QUARTERLY REPORT of RTRI

May   2022 Vol. 63 No. 2

CONTENTS

RAILWAY TECHNICAL RESEARCH INSTITUTE

CONTENTS

Recent Activities for Research and Development of Vehicle Technology

Makoto ISHIGE

Vehicle Technology Division

RTRI is engaged in R&D focusing on enhancing safety based on the Master Plan RESEARCH 2025. In the vehicle field, about 40 themes are implemented annually, targeting safety improvements and cost reduction. This paper introduces four recent achievements related to vehicle technology: running stability evaluation, a brake control method, a battery degradation evaluation method, and development of a train positioning system.

1. Introduction

RTRI organizes its work according to a five-year Master Plan established as a mid-term management plan. FY2021 was the second year of the "Master Plan — Research and Development for Creating the Future of Railways — RESEARCH 2025". The basic guiding policies for R&D within this plan are (1) enhancing safety with an emphasis on improving resilience to natural disasters, (2) developing innovative railway systems based on digital technologies, (3) creating high-quality results by taking advantage of our collective strength. It also sets out four R&D objectives: safety improvement, cost reduction, harmony with the environment, and improved convenience.

R&D in the railway vehicle field is mainly handled by nine laboratories belonging to three divisions: Vehicle Structure Technology, Vehicle Control Technology, and Railway Dynamics. Together, these laboratories work on about 40 R&D subjects every fiscal year. Figure 1 shows the number of FY2020 and FY2021 R&D subjects by objective. Safety improvement accounts for approx. 40%, which is the most important action item. It is followed by cost reduction (< 20% to 30%) and harmony with the environment and convenience improvement (< 20% each). Due to the spread of COVID-19 at the beginning of 2020 and after, the railway business is facing an unprecedentedly difficult situation. Amid uncertainty about how the future will unfold, railway system innovation through unmanned operations, labor- and manpower-saving business, etc. have become urgent issues for the maintenance and development of railways. As such, much is expected from R&D to help tackle these issues. Consequently, there has been an increase in the number of vehicle-related R&D projects which aim to cut cost, which together with improving safety, have become the two priority directions for work.

This paper outlines the following recent R&D outcomes: "an analytical evaluation method for the speed at which hunting oc-

curs," "a brake control method to compensate for reduced braking force," "a degradation evaluation method for lithium-ion batteries for vehicle control circuits," and "a high-accuracy train positioning system for tilting trains."

2. Analytical evaluation method for the speed at which hunting occurs [1]

Hunting motion tests are conducted on rolling stock test equipment to examine the speed at which the hunting motion (an oscillation phenomenon peculiar to railway vehicles) occurs. However, the speed at which hunting motion occurs varies depending on the type of excitation. It has been experimentally shown that the reason for this is that hunting motion occurs when the amplitude of the wheelset lateral displacement caused by oscillation exceeds a certain threshold. This study examined a method for analytically finding the boundary line that separates occurrence of hunting motion and its convergence, which is called the critical hunting curve (Fig. 2).

The study found that when the wheelset amplitude is above the critical hunting curve, oscillation diverges and reaches hunting motion, and when it is below the curve, oscillation converges but just on the curve, there is a steady-state oscillation that theoretically does not diverge or converge and has a constant period and amplitude (Fig. 3). Thus, a method was constructed to analytically calculate the amplitude of steady-state oscillation for one point on the critical hunting curve by applying the shooting method, one of the methods for finding the periodic solution of a nonlinear multi-de-

Fig. 1   Number of R&D subjects by objective
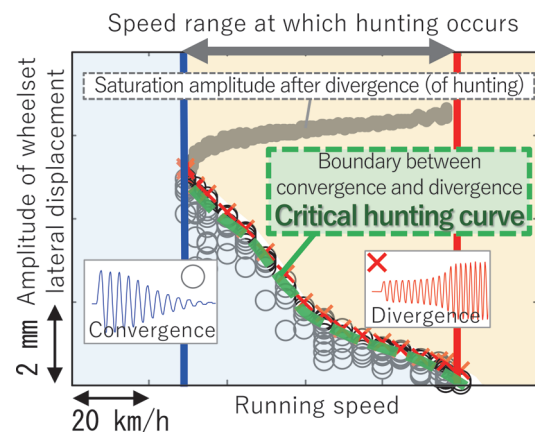
Fig. 2   Critical hunting curve
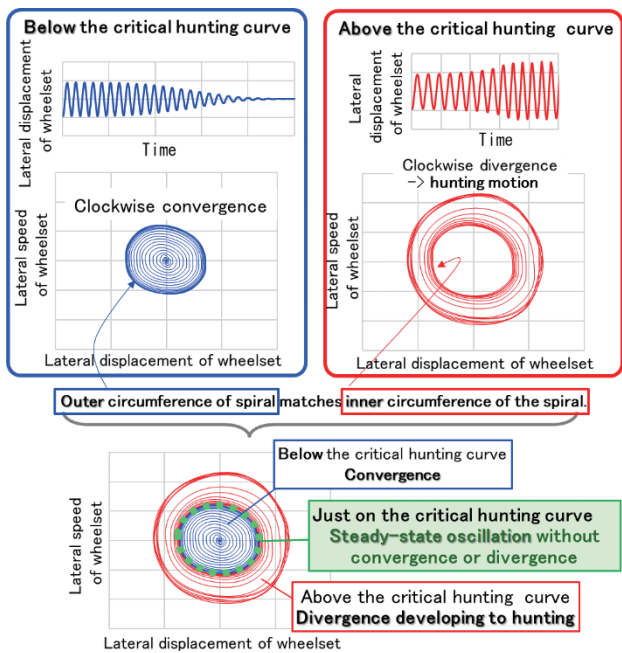
Fig. 3 Steady-state oscillation on the critical hunting curve
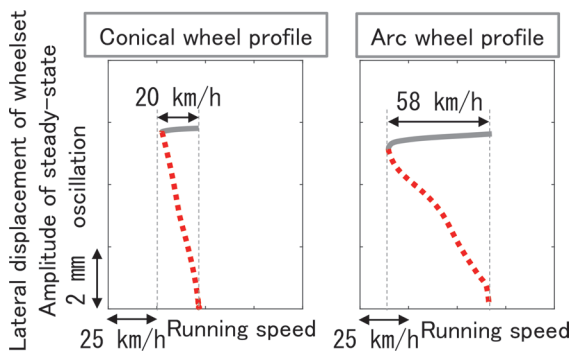
Fig. 4 Example of critical hunting curve calculation

gree-of-freedom system. The method devised therein was to efficiently obtain the next one point using running speeds as a parameter based on the solution of the preceding one point and thus obtain the entire critical hunting curve by repeating the process. Figure 4 shows the results of analytically obtaining the critical hunting curve for a bogie with conical wheel profile and one with arc wheel profile by using this method.

These tests clarified that, depending on the difference in wheel profile, there is a difference in the speed range where hunting motion can occur; the speed range where it can occur is wider for the arc wheel profile, which has stronger nonlinearity than the conical wheel profile in wheel-rail contact.

In addition to further improving the accuracy of this method, we plan to use it to investigate the causes of small-amplitude hunting motion (i.e., continuous small-amplitude oscillation not leading to divergence).

3. Brake control method to compensate for reduced braking force [2, 3]

In a general railway vehicle brake system, a target deceleration is specified for each brake notch. Although braking systems have a load compensation function that compensates for variations in vehicle weight, the effects of variation factors such as variations in braking force, wheel slip, or changes in the gradient unrelated to the vehicle are not automatically compensated. To resolve this, a deceleration control method (a control system that feeds back the deceleration from the vehicle) was proposed in order to always obtain the deceleration corresponding to the selected brake notch. However, when the braking force suddenly drops during braking, it is difficult to prevent extension of the braking distance, and compensating for this requires reselecting the brake notch.

Thus, this study proposed a new method, Distance-Based Deceleration Control, in order to construct a system that does not extend the braking distance even if the deceleration decreases during braking. This control sequentially and automatically updates the deceleration target value according to the braking distance so that the actual deceleration can follow the updated value. With the proposed method, when a new control device added to the brake control system receives a brake command or the distance to the stop position, that command is updated based on the speed fed back from the train before being given to the system (Fig. 5). This device makes the train deceleration follow the target value calculated from the remaining distance to the stop position, and (for insufficient braking force) updates the control brake command sequentially (Fig. 6).

A comparison was made regarding the accuracy of the braking distance with/without applying Distance-Based Deceleration Control to the test train on a test line at RTRI. In the set condition, the
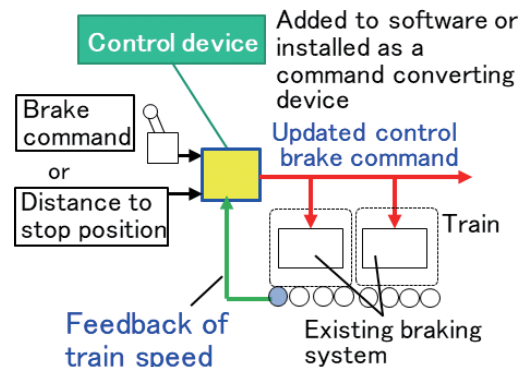
Fig. 5 System configuration of the Distance-Based Deceleration Control method
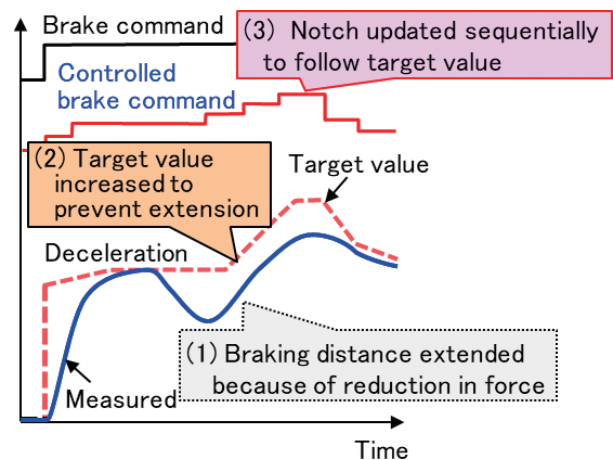
Fig. 6 Control operation of the Distance-Based Deceleration Control method

brake was initiated at 30 km/h, and when the speed fell below 20 km/h, the braking force was intentionally reduced by 25%, and the resulting amount of the extended braking distance was compared. For an existing brake system (without feedback control), the amount of extension was 8.4 m, whereas Distance-Based Deceleration Control suppressed the excess distance to 0.16 m.

Since this method uses deceleration and braking distance calculated from the fed-back vehicle speed, the speed accuracy is estimated to influence the control performance greatly. From now, we will work to investigate the effect of speed control on control performance and to improve the stability of control.

4. Degradation evaluation method for lithium-ion batteries for vehicle control circuits [4]

There are instances in which lithium-ion batteries (LIBs) for driving are installed on trains in preparation for train running on a non-electrified line or emergency running in the event of an overhead contact line power outage. On the other hand, there are instances where LIBs are used instead of conventional lead or similar storage batteries, as control circuit batteries for Shinkansen vehicles. LIBs are more expensive than conventional batteries, but maintenance is generally lower, because of their longer lifetime and they are smaller and lighter because of their high energy density.

To ensure reliability and save on maintenance of control circuit LIBs, we investigated battery degradation behavior through basic experiments. The results were then used to develop a degradation evaluation method which can predict the battery life and diagnose battery health after it has been placed into service.

As for the basic experiments to grasp the degradation tendency, an accelerated test was conducted in which the degradation progress was equivalently accelerated by a factor of 3 or 9. To this end, the ambient temperatures of the test batteries were set by adding 10 or 20°C to the assumed temperature of the actual vehicle. A method was constructed to predict changes in battery capacity and internal resistance over time based on experimental results. As for the battery capacity, Fig. 7 shows a comparison between the predicted values based on the prediction method and the measured values. It shows that the solid curved lines of the predicted values match the measured value plots with high accuracy.

For deciding when to replace the control circuit battery, the actual degree of degradation after the start of operation is an important judgment factor; therefore, this study also proposed a method for diagnosing the degree of degradation from the battery charge/discharge data [5]. Most of the charge/discharge waveforms of control circuit batteries include the repetitions of the monotonous charge and the very short time discharge during train passage through the section, which makes it difficult to apply conventional techniques such as the iterative least squares method and Kalman filter; therefore, the discharge and charge waveforms before and after the pantograph rise were cut out and used for the degradation diagnosis. Comparison with experimental data was made to verify the effectiveness of the proposed method. Figure 8 shows the comparison result between the calculated battery capacity index values based on the proposed method and the measured values. The diagnostic values along the vertical axis were well approximated by the linear expression of the measured values. By obtaining this relational expression in advance, this enables obtaining the degree of degradation by converting the calculated degradation index value acquired from the data in operation.

The proposed battery degradation evaluation method is, for
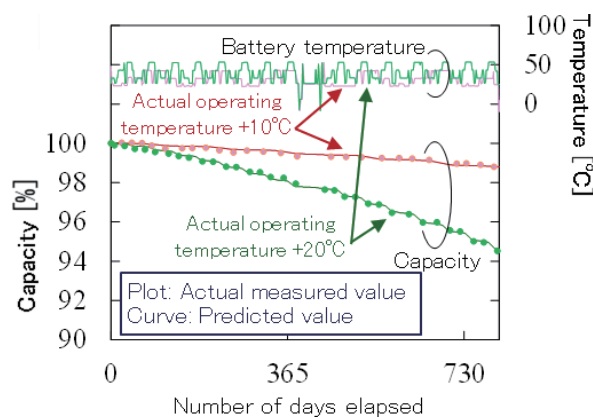
Fig. 7 Comparison of predicted values and measured values
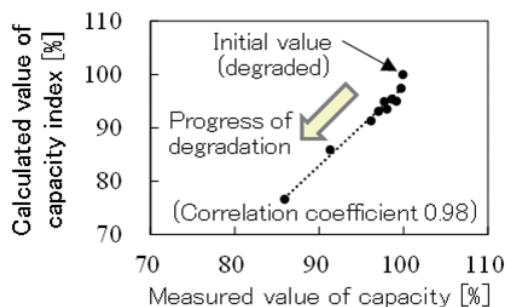
Fig. 8 Comparison between the calculated and measured capacity index values

example, available to estimate the life of a battery of the same type at a design stage of a vehicle control circuit or estimate the remaining life of a storage battery at the time of periodic inspection following the start of vehicle operation.

5. High-accuracy train positioning system for tilting trains [6, 7]

This area of work aims to improve tilting control systems to suppress motion sickness caused by car body tilting behavior and increase ride comfort. The underlying technologies include accurate positioning of running cars, calculation of tilting angles taking into consideration curvature and human response, and tilting actuators offering ideal car body tilting control.

To achieve this, we have been developing a train positioning system (Fig. 9) that uses track curvature collation as opposed to the conventional method of identifying the location based on the installation position of the Automatic Train Protection beacon. This system calculates the track curvature from both the onboard measured running speed and the vehicle yawing angular velocity, and compares it with the reference track curvature data generated by designated signal processing of the curvature measured during running in advance to identify the vehicle position and make the positional correction. A spatial filter, which is a length-based filter, is applied to the calculation of the curvature of railway track to eliminate the effects of differences in vehicle sway between different types of vehicles and changes in track conditions due to aging.

We will proceed verification tests for detecting abnormality of the car body tilting condition toward installation of the tilting control system on actual vehicles.
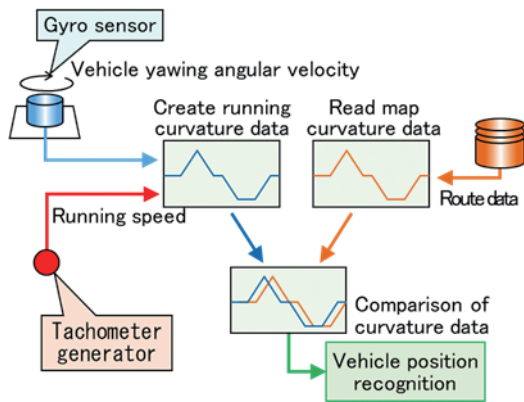
Fig. 9   Train positioning system
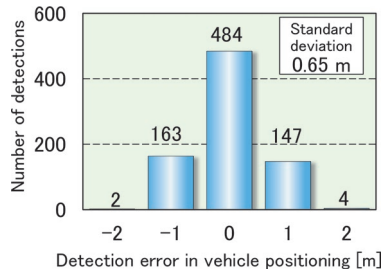
Fig. 10   Distribution of vehicle position detection errors

Furthermore, the developed method can continue recognizing the vehicle position by track curvature collation also when at a station, the train enters a track different from the onboard database or when large-scale wheel sliding occurs, in addition to maintaining an accuracy while running in the long straight section. In the running test, we have confirmed that this system can identify the vehicle position accurately with an error of ± 2 m (Fig. 10).

6. Conclusions

Out of recent R&D outcomes related to vehicle technologies, this paper outlined work on running stability evaluation, a brake control method, a degradation evaluation method for LIBs, and de-velopment of a train positioning system for tilting trains.

Assuming that birthrates and the working population will continue to decline, R&D has a key role to play in finding ways to reduce maintenance in the railway vehicle field. The COVID-19 crisis has increased the urgency of developing such methods. Therefore, to meet these needs, RTRI is prioritizing R&D which can help save labor and maintenance, as well as improve safety.

References

[1] RTRI Major Results of Research and Development in Fiscal 2020:Analytical evaluation method for the speed at which hunting occurs (Feb. 12, 2022),
https://www.rtri.or.jp/eng/rd/seika/2020/05-23.html
(Feb. 12, 2022).

[2] Nakazawa, S., "Accuracy Improvement of Braking Distance by Deceleration Feedback Function Applying to Brake System," *QR of RTRI*, Vol. 62, No. 3, 2021.

[3] RTRI Major Results of Research and Development in Fiscal 2020:Brake control method to compensate for reduced braking force (Feb. 12, 2022),
https://www.rtri.or.jp/eng/rd/seika/2020/01-07.html
(Feb. 12, 2022).

[4] RTRI Major Results of Research and Development in Fiscal 2020:Degradation evaluation method for lithium-ion batteries for vehicle control circuits (Feb. 12, 2022),
https://www.rtri.or.jp/eng/rd/seika/2020/02-18.html
(Feb. 12, 2022).

[5] Taguchi, Y., Kadowaki, S., Yoshikawa, G., Kato, H., Sato, K., Sekino, M., Tsukihara, T., Kikkawa, K., "Fundamental Study on a Degradation Diagnosis Method for Lithium-ion Battery Adopted to Control Circuit of Railway Vehicles," presented at *the IEEJ Annual Meeting*, Mar. 10, 2021, 5-158 (in Japanese).

[6] Harada, K., Maki, Y., Ishiguri, K., Kazato, A., "Development of Train Positioning System Using Track Curvature Collation Applied with Spatial Filtering," *QR of RTRI*, Vol. 61, No. 3, 2020.

[7] RTRI Major Results of Research and Development in Fiscal 2020:High-accuracy train positioning system for tilting train (Feb. 12, 2022),
https://www.rtri.or.jp/eng/rd/seika/2020/04-20.html
(Feb. 12, 2022).

Author

Makoto ISHIGE
Director, Head of Vehicle Technology Division
Research Areas: Bogie Structure

Recent Research and Development on Maintenance of Existing Railway Structures "Inspection, Diagnosis and Reinforcement"

Masayuki KODA
Structures Technology Division

Maintenance of existing railway structures is becoming more and more important for safe and stable operation of railways. However, severe meteorological disasters in recent years have caused enormous damage to railway structures and hindered railway operations. The technical issues surrounding railway structures are wide-ranging, including labor-saving measures for maintenance of existing railway structures, disaster countermeasures, and early recovery measures after disaster. In this paper, we outline the direction of research and development, that the Railway Technical Research Institute is working on, related to maintenance of the existing railway structures, for example, inspection, diagnosis and reinforcement.

Key words: *railway structure, existing structure, maintenance, inspection, diagnosis, reinforcement*

1. Introduction

For safe and stable railway operations, maintenance of existing railway structures is becoming more and more important. However, recent severe meteorological disasters have caused enormous damage to railway structures and sometimes hindered train operations. The technical issues around railway structures range widely, including labor- and manpower-saving measures for maintenance of existing railway structures, pre-implemented disaster measures, and early recovery measures after a disaster.

RTRI has decided to concentrate on advanced R&D from FY2020 that will contribute to improving safety against natural disasters, amongst other threats, and labor-saving using digital technologies under the new Master Plan, "RESEARCH 2025". Specifically, RTRI will focus on R&D that will contribute to maintenance technology and construction & improvement technology as well as R&D that will contribute to the disaster countermeasure technology (including early recovery technology) in an emergency, applying digital technology such as simulations connected to network systems based on any databases.

This perspective outlines several recent R&D topics related to maintenance of existing railway structures such as inspection, diagnosis and reinforcement that RTRI has been working on, and finally presents technologies geared to reinforce existing steel bridges with structural changes as an example of the practical application of this R&D. For details of topics covered in this Perspective, refer to the website of the 340th Railway Technical Research Institute Monthly Presentation [1].

2. Research and development on maintenance of existing railway structures, "inspections, diagnosis and reinforcement"

Table 1 summarizes examples of recent R&D on maintenance of existing railway structures, "inspection, diagnosis and reinforcement" that RTRI has been working on. It also lists the target structures, applications, and keywords. R&D in Nos. 1 and 2 covers inspection of bridges and viaducts, whereas Nos. 3 and 4 investigate diagnosis and reinforcement of station facilities, and Nos. 5 to 7 focus on diagnosis and reinforcement of soil structures and tunnels. The R&D covered in items Nos. 1 to 7 of the table are explained individually below (Fig. 1).

2.1 Factor analysis for cracking on RC girders by using image analysis and FEM [2]

Individual Inspections of RC structures estimate the causes of deformation, such as cracks. These are indispensable inspection activities to evaluate the current and future performance of structures and to connect them to the presence/absence of monitoring, repair and future reinforcement. Thus, it has been made possible to estimate the factors of deformation (e.g., dead load, train load, temperature, effect of shrinkage/creep) by automatically extracting cracks from captured images and reproducing the extraction results

Table 1 Examples of recent R&D on maintenance of existing railway structures "inspections, diagnosis and reinforcement"

No	R&D title	Target structure	Application	Keywords
1	Factor analysis for cracking on RC girders by using image analysis and FEM	Bridges and viaducts	Individual Inspection	crack, image, FEM, factor analysis
2	Support System for the Visual Inspection of Structures Utilizing 3D Images	All structures	General Inspection	3D image, visual inspection, SfM(Structure from motion)
3	Evacuation Safety Verifying Support System in Case of Station Fire	Station facilities	Diagnosis	fire, evacuation safety, personal behavior model, passenger flow
4	Seismic Reinforcement Method for Station Building Ceilings with Short Hanging Distances	Station facilities	Reinforcement	suspended ceiling, seismic reinforcement with square steel pipe, noise abatement measure
5	Calculation method of earth pressure acting on a retaining wall from adhesive backfill during earthquakes	Retaining walls	Diagnosis and reinforcement	adhesive resistance force, active earth pressure during earthquake, centrifugal model test, seismic reinforcement
6	Seismic reinforcement design method for existing embankments using slope frame and nail-reinforced soils	Embankments and cuts	Diagnosis and reinforcement	water impermeability of slope frame, connection between slope frame and nail-reinforced soils, seismic reinforcement
7	Floor heave mechanism and the effect of countermeasures for mountain tunnels	Tunnels	Diagnosis and reinforcement	floor heave, monitoring, ground deterioration method, reinforcement

through nonlinear finite element analysis. Thus, data can be obtained, that will help determine the timing of future repairs and type of repair, drawing on information about minute cracks, including crack width and length, the position of the crack, and number of cracks.

2.2 Support System for the Visual Inspection of Structures Utilizing 3D Images [3]

General Inspections of railway structures are mainly performed visually, and only photographs of the deformed parts and comments on the deformations are recorded in many cases. Thus, a Support System for the Visual Inspection of Structures has been developed, that can generate a 3D image of the structure from given images. The system enables users to intuitively grasp the conditions of the structure and the surrounding environment with 3D images, and can also assist both the extraction of deformations and the creation of records. This system generates a 3D image semi-automatically from 2D image data taken as moving images by using Structure from Motion (SfM). It allows users to visually compare inspections made of a structure at different times, directly on the same screen. It also allows them to grasp the progress of deformation of the structure by bringing past 3D images to the field with a tablet computer or similar device and comparing them with the current structure.

2.3 Evacuation Safety Verifying Support System in Case of Station Fire [4]

Evacuation safety in the event of a station fire is generally ensured by applying the specifications of the Building Standards Act, which stipulates maximum distances to evacuation exits. However, in stations with large passenger flows, where people may have to wait for the arrival or departure of trains, safer station spaces are required not only in terms of station equipment such as stairs, escalators, and elevators but also from the viewpoint of guidance and operation beyond the legal minimum level. RTRI has therefore an developed Evacuation Safety Verifying Support System that verifies the evacuation safety of passengers in stations by combining simulations of smoke diffusion in the event of a fire and passenger evacuation flow simulations, with a built in individual behavior model.

2.4 Seismic Reinforcement Method for Station Building Ceilings with Short Hanging Distances [5]

In an under-viaduct station building with a short hanging distance, applying anti-seismic braces (a general seismic reinforcement method) is difficult because of the need to ensure some space is left above the ceiling. In addition, until now there has been no reinforcement method that can achieve inexpensive seismic reinforcement without affecting the space above ceilings. Thus, for such under-viaduct station buildings, we have developed an inexpensive seismic reinforcement method that is easy to construct using square steel pipes. In addition, the effectiveness of train noise abatement measures adaptable to this construction method, was demonstrated in order to improve the comfort of under-viaduct station building spaces. These are RTRI's original construction methods.

2.5 Calculation method of earth pressure acting on a retaining wall from adhesive backfill during earthquakes [6]

For existing retaining walls, the backfill is often constructed with adhesive soils. In this case, it may be unreasonable to perform
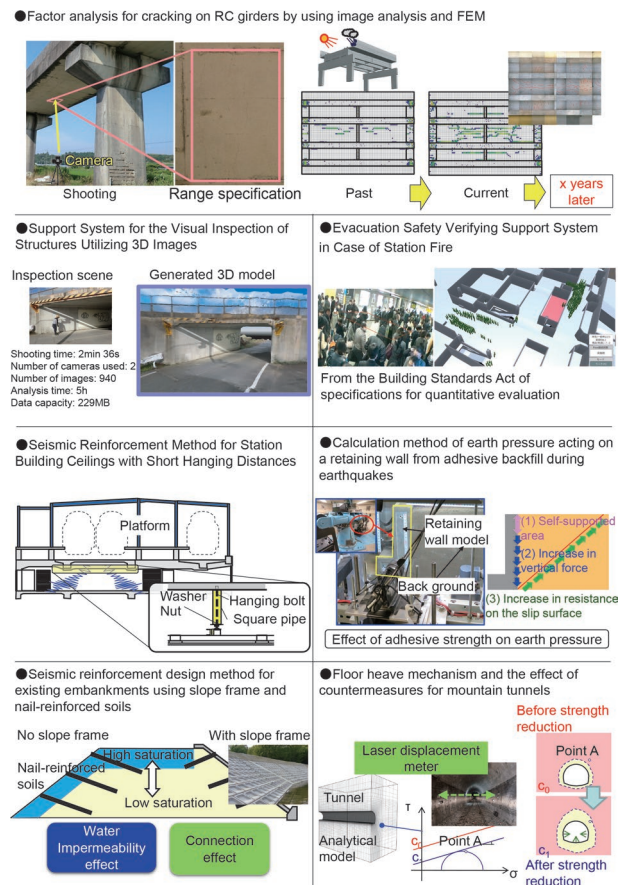
Fig. 1 Examples of recent R&D on maintenance of existing railway structures

seismic diagnosis or seismic reinforcement of the retaining wall against extremely large earthquake motion, such as Level 2 Earthquake Motion, adopting conventional methods which ignore the effect of adhesive resistance force. This study showed the expression mechanism of active earth pressure by adhesive resistance force elucidated through centrifugal model tests and the calculation method of the earth pressure, and the cost reduction effect based on this mechanism.

2.6 Seismic reinforcement design method for existing embankments using slope frame and nail-reinforced soils [7]

Although slope frames are often constructed in existing embankment for the rainfall measures, this effect is not taken into account in seismic diagnosis or reinforcement design. This research clarified the water-impervious effect of the slope frame made on an existing embankment and the effect of connecting the slope frame and the nail-reinforced soils; in addition, it proposed a seismic reinforcement design method for existing embankments in consideration of these effects. It also has developed a new slope frame that can be used for seismic reinforcement.

2.7 Floor heave mechanism and the effect of countermeasures for mountain tunnels [8]

In mountain tunnels, inner sections may shrink due to deformation of the natural ground. However, the effects of countermeasure (e.g., back-filling, rock bolts) have not been quantitatively evaluat-

ed. In addition to constructing a system that monitors internal displacement and other parameters, in real-time, this study estimated the effects of the countermeasures based on the monitoring data, and presented the design method used for developing the countermeasures that can suppress inner displacement velocity.

3. Technology to reinforce existing steel bridges through structural change [9]

3.1 Outline of the Integral Reinforcement Method with Nail-Reinforced Soil

For steel girder-abutment type bridge, since the backfill is constructed after the construction of the abutments, subsidence or lateral movement of the abutment may occur due to the backfills. On the other hand, for aged steel bridges, in addition to the corrosion of steel girders and bridge bearings, subsidence of backfills with aging, and clines or cracks in the abutments or subsidence of the backfills may occur during earthquakes. In some cases this may lead to bridge collapse due to the fragile seismic resistance of abutments and back embankments.

To extend the life and increase resistance to disasters of existing steel girder-abutment type bridges, and to solve these issues without replacing bridges, a reinforcement countermeasure was proposed that integrates steel girders, abutments and backfills by connecting the abutments and backfills with nail-reinforced soil and forming the steel girders and abutments into a rigid-frame structure by RC lining. This type of bridge is called an Integral Bridge with Nail-Reinforced Soil, and the reinforcement method is called the Integral Reinforcement Method with Nail-Reinforced Soil (Fig. 2). It is a reinforcement technology where the basic concept of the new bridge type, "Integral Bridge with Geosynthetics-Reinforced Soil" is applied to the reinforcement of existing steel girder-abutment type bridges.

3.2 Verification tests with a full-scale test bridge

RTRI constructed a full-scale test bridge consisting of steel girders, abutments, and embankments, conducted a test to verify the workability about combining abutment/backfills by nail-reinforced soils, and integrating steel girders/abutments by RC lining. In addition to the static loading test and vibration generator test before and after the integral reinforcement, the following measurements and tests were conducted: long-term measurements, repeatable horizontal loading tests simulating steel girder expansion/contraction depending on the temperature, and repeatable positive/negative horizontal loading tests to verify seismic resistance. The following shows the results of a series of demonstration tests using a full-scale test bridge.

This test was conducted on a full-scale test bridge with a girder length of 13.32 m in order to examine the effect of the expansion/contraction of steel girders due to the temperature change after the integral reinforcement against the abutment top and back embankments; with measuring equipment attached to the test bridge, long-term measurements were taken over a whole year after the reinforcement. The temperature change of the steel girders was approx. 30°C/year (measured at 00:00). On the other hand, the relative horizontal displacement between the top of the A1 abutment and the top of the backfill was approx. 1.0 mm/year (that at the A2 abutment was approx. 1.5 mm/year; the elongation of the free-end test bridge calculated from the coefficient of linear expansion is 4.80 mm). In
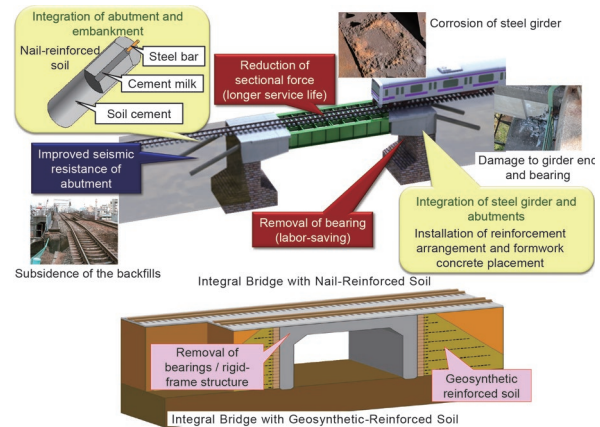
Fig. 2 Integral Bridge with Nail-Reinforced Soil and Integral Bridge with Geosynthetics-Reinforced Soil
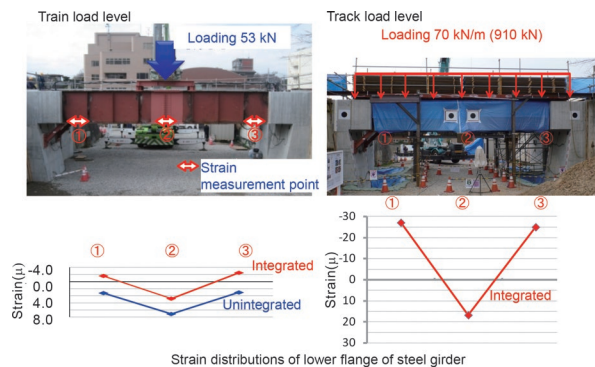
Fig. 3 Strain distributions of lower flange of steel girder (static vertical loading test)

the one-year long-term measurement, the deformation of the steel girders was suppressed by the portal-type rigid-frame structurization and the restraint of the backfills. In addition, no deformations and cracks in the steel girder-abutment joint, or subsidence of backfills occurred, and the steel girders exhibited stable expansion/contraction behavior.

A static vertical loading test by the weight of the vibration generator and a vibration test using the generator were conducted before and after the steel girder-abutment integral reinforcement (vibration generator: weight 53 kN, vibration force within ±60 kN, frequency ≤ 30 Hz). The purpose of these was to check the reduction effect of the live load response of the test bridge constructed by the steel girder-abutment integral reinforcement method (the reduction effect means that the bending moment and deflection at the center of the steel girder are theoretically halved). Both the static vertical loading test by the vibration generator weight and the vibration test showed that the strain on the lower flange of the steel girder in the center of the span was almost halved after the integral reinforcement. The static vertical loading test at the rail track load level (70 kN/m, total 910 kN) showed that the bending strain at the end of the girder showed upward tension and demonstrated that both ends of the steel girder were sufficiently fixed by the connecting with the abutments at both ends of the steel girder (Fig. 3).

Next, to check the seismic resistance, a repeated positive/negative horizontal loading test that applied force to the girder along the bridge axis was conducted on the test bridge after the integral reinforcement. The test results showed that the maximum horizontal

displacement of the top of the A1 abutment was approx. 10 mm for the horizontal force equivalent to the Level 2 Earthquake, and the residual horizontal displacement after unloading was very small, at less than 5 mm (Fig. 4). After the loading test, damage to the concrete body and subsidence of the backfills were found, which clarified that the damage was extremely minor and was soon restorable even when a horizontal force equivalent to a Level 2 Earthquake was applied.

3.3 Application to an actual existing steel bridge

The target bridge was an overbridge with a bridge length of 13.42 m, including the gravity-type concrete abutments with the spread foundations. The Integral Reinforcement Method with Nail-Reinforced Soil was adopted after a comprehensive comparison and consideration in terms of reinforcement conditions and costs and others in order to take seismic countermeasures for the steel bridges. The actual work is detailed in Reference 10 (Fig. 5).

The use of this reinforcement method allowed us to significantly reduce the reinforcement cost and shorten the reinforcement period compared to the replacement of the existing bridge. After the Integral Reinforcement, the deflection amount at the center of the steel girder when the train passed was reduced from 1/2 to 1/3 compared to the previous amount of deflection. It is expected that the longer service life of the steel girder can be extended. In addition, the rigid-frame structurization eliminates bridge bearings, which will dispense with the need for maintenance including cleaning. Furthermore, it was clarified that the RC lining at the end of the girder and the increase in the weight of the girder have a noise abatement effect.

4. Conclusions

This perspective outlined recent examples of R&D related to maintenance, "inspection, diagnosis and reinforcement of existing railway structures" that RTRI has been working on, and finally presented the reinforcement technology for existing steel bridge through structural change, as an example of how this R&D can be applied in practice.

As explained at the beginning, in the future we will promptly focus on R&D that will contribute to the maintenance technology and construction & improvement technology, as well as R&D that will contribute to disaster countermeasure technologies (including early recovery technology) for emergencies, and applying digital technology such as simulations connected to network systems based on any databases. These include (i) R&D on rainfall diagnostic methods and disaster countermeasures for railway river bridges and railway embankments and (ii) R&D related to visual inspection support, repair and reinforcement methods for railway concrete structures and railway tunnels. Railway management is currently in a difficult situation due to the prolonged COVID-19 crisis, but we would like to pursue specific utilization methods of R&D outcomes that will lead to safe and sustainable railways with an eye on a post-COVID-19 society.

References

[1] Koda, M., "Recent Research and Development on Railway Structures," *340th Railway Technical Research Institute Monthly Presentation*, Sep. 2020 (in Japanese). <https://www.rtri.or.
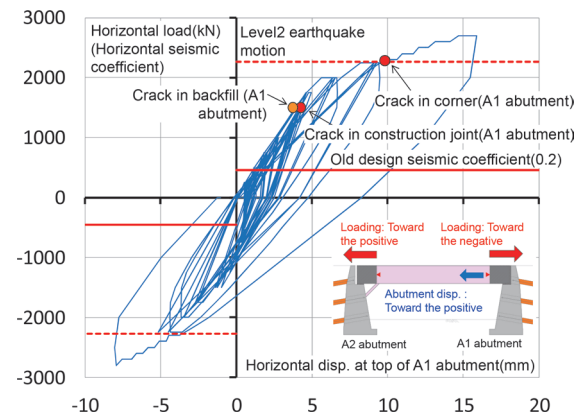
Fig. 4 Horizontal load-horizontal displacement relationship at the top of the A1 abutment (repeated positive/negative horizontal loading test)
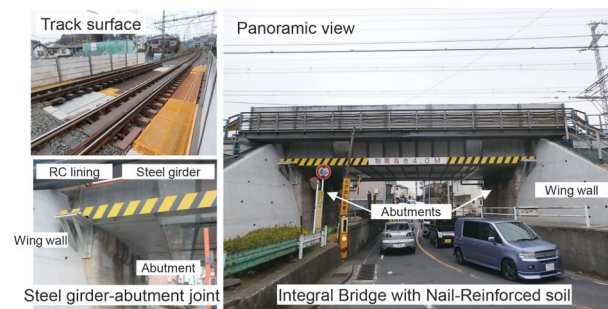
Fig. 5 Applying the Integral Reinforcement Method with Nail-Reinforced Soil to an actual existing steel bridge

jp/events/getsurei/2020/mr340.html>

[2] Noma, Y., Sawada, S., Nishimura, T., Sato, Y., & Watanabe, K., "Development of Crack Image Measurement Method by Using Luminance and Geometric Properties and In-situ Experiment of RC Deck," *4th International Symposium on Concrete and Structures for Next Generation*, pp. 345-352, June 2019.

[3] Kobayashi, Y. & Jimba, W., "Development of Assist System for Visual Inspection of Railway Structures with 3D-images," *Japanese Railway Engineering*, No. 214, pp. 11-13, Oct. 2021.

[4] Ishizuki, M. & Yamamoto, M., "Proposal Evaluation System for Evacuation Safety in Case of Station Fire," *RTRI Report*, Vol. 33, No. 9, pp. 41-46, Sep. 2019 (in Japanese).

[5] Shimizu, K., Miki, H., & Yamada, S., "Seismic Reinforcement Method for Ceilings in Under-Viaduct Stations Combining Noise Abatement Measures," *Quarterly Report of RTRI*, Vol. 62, No. 1, pp. 40-46, Feb. 2021.

[6] Nakajima, S., Ozaki, T., Sanagawa, T., "1g Shaking Table Model Tests of Seismic Active Earth Pressure Acting on Retaining Wall with Cohesive Backfill Soil," *Soils and Foundations*, Vol. 61, pp. 1251-1272, 2021. <https://doi.org/10.1016/j.sandf.2021.06.014>

[7] Fujimoto, T., Nakajima, T., Matsumaru, T., Nakajima, S., Kurakami, Y. & Sugiyama, K., "Seismic Reinforcement Design Method for Existing Embankments Considering the Effect of Fixing between Slope Frame and Nailed-Reinforced Soils," *Proceeding of 75th Annual Presentations of Japan Society of Civil Engineers*, III-132, 2019 (in Japanese).

[8] Shimamoto, K., Yashiro, K. & Kawagoe, T., "Floor Heave

Mechanism and the Effect of Countermeasures for Mountain Tunnels," *Quarterly Report of RTRI*, Vol. 63, No. 2, pp. 115-120, May 2022

[9] Koda, M., Yokoyama, T., Nonaka, T., Kobayashi, Y. & Tateyama, M., "Method for Restoring and Reinforcing Deteriorated Steel Railway Bridges -Development of Integral Bridges with Nail-Reinforced Soil-," *Quarterly Report of RTRI*, Vol. 54, No. 1, pp. 1-7, May 2013.

[10] Hayakawa, Y., Okino, S. & Sanagawa, T., "Seismic Reinforcement Project for the Former Onda River Bridge in Odakyu-Odawara Line - Introduction of the Reinforcement Method Integrated by Nailed Reinforcement Soil," *Geotechnical Engineering Magazine*, Vol. 69, No. 4, pp. 27-30, April 2021 (in Japanese).

Author

Masayuki KODA, Dr. Eng.
Director, Head of Structures Technology Division & Foundation and Geotechnical Engineering Laboratory
Research Areas: Foundation & Geotechnical Engineering, Soil Mechanics

Technology for Experiment/Measurement to Clarify Phenomena Specific to Railway System

Fumiaki UEHAN

Railway Dynamics Division

Railway systems are composed of many sub-systems such as overhead contact lines, vehicles, tracks and structures, which interact with each other and show complex dynamic behavior. In order to clarify the phenomena specific to railways caused by complex behaviors, the Railway Technical Research Institute has developed its own experimental technologies and measurement technologies. In this paper, first, as examples of our experimental technologies, we introduce three newly developed large-scale test facilities. Then, we introduce some of our measurement techniques for condition monitoring of tracks and structures are explained. Finally, we present the outlook for our future R&D policies to be implemented by effectively combining experiment/measurement technologies and numerical simulation techniques.

1. Introduction

Railway systems are composed of overhead contact line structures, vehicles, tracks, and civil structures, each with their own complicated mechanisms (Fig. 1). Understanding these complex mechanisms is required to develop countermeasures against railway-specific phenomena caused by interactions between these components to preserve ride comfort and running performance, prevent equipment deterioration and damage, noise, vibration, and protect against damage from natural disasters.

RTRI has been working on the elucidation of railway-specific phenomena by using advanced simulation technologies [1] and its original experimental and measurement technologies as two wheels (Fig. 2). In addition to an overview of experimental and measurement technologies for elucidating railway-specific phenomena, this report presents the outlook for future technological development through the effective linkage between experimental and measurement technologies and numerical simulations.

2. Experimental technologies related to railway-specific phenomena

2.1 Test facility for elucidating railway-specific phenomena

RTRI has developed various pieces of test facility to clarify various railway-specific phenomena caused by interactions between components such as overhead contact lines, pantographs, vehicles, tracks, and structures. The test facility specifically includes, a Rolling Stock Test Plant which can simulate running tests of actual vehicles running up to 500 km/h by using rollers for two bogies; a Large-scale Low-noise Wind Tunnel which enables evaluation of the aerodynamic and noise characteristics of actual pantographs and vehicle models at a maximum wind speed of 400 km/h; a Large-scale Shaking Table which can shake test pieces (e.g. structures, tracks, and bogies) with a maximum weight of 500 kN, and with an earthquake motion of seismic intensity of 7 on the Japanese seismic scale.

RTRI has also installed three types of new large-scale pieces of test facility in FY2020 in consideration of environmental changes such as increased running speeds for railway vehicles, which are outlined below.
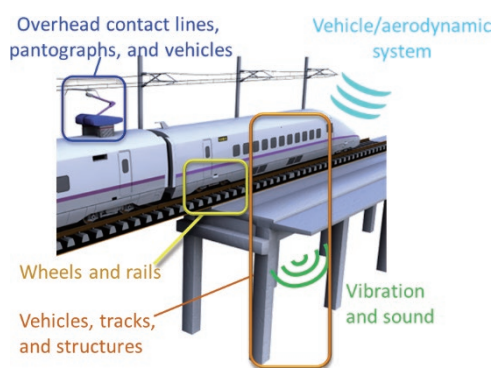
Fig. 1   Railway system and interactions between components
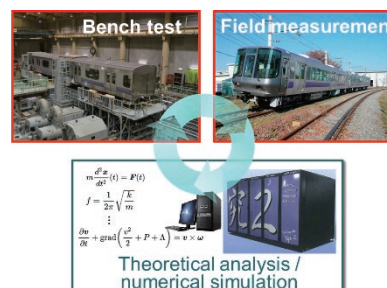
Fig. 2   System for studying railway-specific phenomena

2.2 High-speed test facility for pantograph/OCL systems

RTRI has developed a High-speed test facility for pantograph/OCL systems [2] (Fig. 3) in order to evaluate the compliance characteristics and current collection performance of pantographs, and to clarify the wear phenomenon of contact wires and pantograph contact strips in a high-speed running environment. This machine has an actual pantograph installed on a stand that can be vibrated vertically (max 10 Hz, ±35 mm), and above it, a rotating disc to which the contact wire is fixed: this can simulate the conditions of a pantograph traveling at high speed while sliding with a contact wire by vibrating the rotating disc vertically (max 27.8 Hz, ±100 mm) and laterally (max 5 Hz, ±300 mm) while rotating it at high speed (max 500 km/h). In addition, it has a maximum energization performance of

600 V and 1,000 A with AC or DC, and can control the environment in the test chamber within a temperature range of -20 to 40°C and a humidity range of 10% to 90% by using an environmental atmosphere controller. In the future, we will apply a hybrid simulation method combining this machine and numerical simulation and will utilize it for the development and performance evaluation of pantographs and contact strips and to elucidate the causes of accidents.
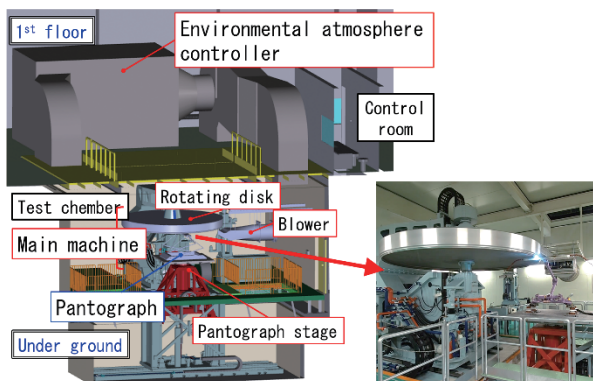
Fig. 3 High-speed test facility for pantograph/OCL systems

2. 3 High-speed wheelset dynamic load test facility

RTRI has developed a High-speed wheelset dynamic load test facility [3] (Fig. 4) in order to evaluate the durability of wheels, axles, bogie parts, etc. of vehicles traveling at high speed and to clarify damage mechanisms. This machine can reproduce the conditions in which a bogie equipped with a load frame simulates the load and sway of a car body running on rails at up to 500 km/h by rotating rollers that simulate rails at high speed. It can simulate the load generated on the bogie by reproducing the vertical displacement of the track by the vertical vibration (max ±15 mm) of the rollers and the car body vibration by the vibration of the load frame (max ±100 mm both vertically and laterally). It can also simulate the torque acting on the wheelset during acceleration and deceleration. In the future, we will utilize it for performance and durability evaluation of wheelsets, bearings, other bogie parts, etc., and for investigation of failure causes.
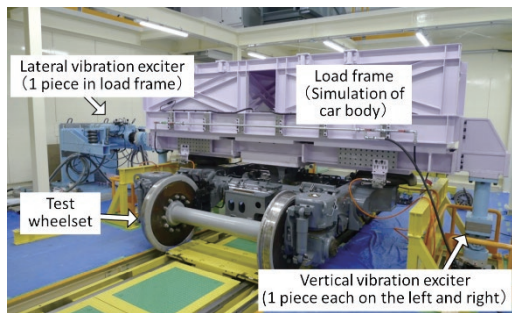

Fig. 4 High-speed wheelset dynamic load test facility

2.4 Low-noise moving train model running test facility

RTRI has developed the Low-noise moving model test facility [4] (Fig. 5) in order to clarify the aerodynamic noise generated by the vehicle and the phenomenon related to the action on the vehicle and structures by precisely reproducing the air flow and turbulence around the vehicle traveling at high speed. This equipment can run a

1/20 scale real-shaped vehicle model at high speed (400 km/h for 2.5 train set length or 350 km/h for 7.5 m train set length) by using launching rotating-wheel equipment, and makes it possible to evaluate the relative motion of the vehicle and the ground, the 3D characteristics of the vehicle head shape, and the effect of train set length.

The measurement section is in a semi-anechoic chamber with sound-absorbing material attached to the wall surfaces and ceiling, which enables evaluation of the aerodynamic noise acoustic characteristics, including the low-frequency domain. In the future, we will utilize it for elucidating the generating mechanism underlying aerodynamic noise and acting load generated during train passage, examining the measures to reduce tunnel micro-pressure waves, and acquiring data for verification and development of numerical simulation technology.
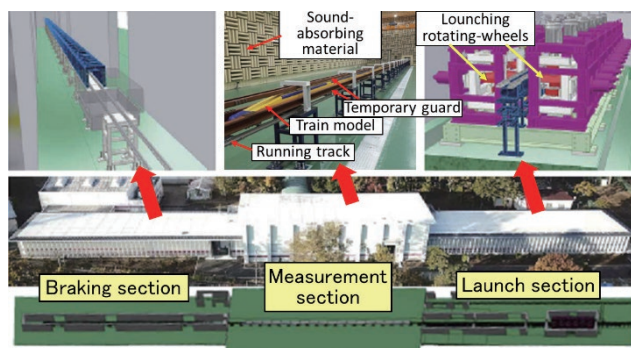
Fig. 5 Low-noise moving train model running test facility

3. Measurement technologies related to railway-specific phenomena

3.1 Dynamics-focused track/structure measurement technology

Grasping railway-specific phenomena requires the technologies for effectively measuring dynamic phenomena including complex interactions among railway components. RTRI has been working on the development of various measurement technologies for the realization of advanced bench tests and the effective grasp of real railway field information. As the previous section presents the bench test technology around the vehicle, this section shows an example of the development of measurement technology with the purpose of monitoring the condition of ground facilities in an actual railway line section.

The conditions of tracks and structures gradually change due to the dynamic action of traveling load from railway trains, causing performance degradation by deterioration or damage. To improve the efficiency of railway maintenance, it is necessary to detect signs indicating potential anomalies and failures by monitoring the condition of facilities and taking advance measures. To realize this Condition Based Maintenance, it is indispensable to develop and apply advanced sensing and monitoring technology. Therefore, RTRI is working on the development of a unique condition monitoring technology focusing on the vibration characteristics of tracks and structures.

3.2 Monitoring track condition

3.2.1 Wireless monitoring of ballast vibration acceleration

To elucidate the cause of ballasted track ballast subsidence, ballast vibration is measured using an acceleration sensor. To elimi-

nate obstacles, such as cables, to maintenance work in addition to improving the efficiency of this vibration measurement work, RTRI is working on making the ballast vibration acceleration sensor wireless [5]. We constructed a three-axis acceleration measurement system equipped with a Wi-SUN module (wireless communication unit), and verified that vibration data can be transmitted wirelessly even in an environment surrounded by many obstacles such as ballast, sleepers, and ballast curbs as shown in Fig. 6. We expect that by developing such wireless sensor measurement technology, it will be possible to monitor the condition of each track part more efficiently in the future.
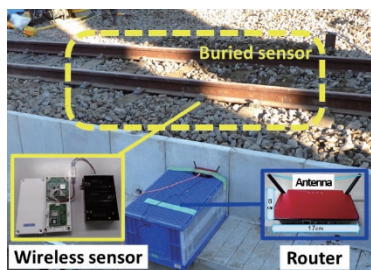

Fig. 6   Ballast acceleration wireless monitoring

3.2.2   Concrete sleeper inspection technology

Some prestressed concrete (PC) sleepers, installed over 50 years ago, are now old and have cracks and other damage that are becoming apparent. Thus, we have developed a hammering test technology for PC sleepers to supplement the accuracy of visual inspection by quantitative evaluation based on numerical data [6]. Cracks on sleepers reduce their stiffness and natural frequency. Thus, the natural frequency of the sleeper is estimated by impact-vibrating the sleeper with a hammer as shown in Fig. 7 and measuring the hammering sound generated along with the vibration.

The accuracy of such inspections can be improved by utilizing vibration and hammering sounds of the third mode, which are highly sensitive to damage and are not easily affected by the support status of the sleeper. Currently, inspections are performed by workers making rounds on foot. The efficiency of such inspections is therefore expected to improve by developing mechanized vehicle-mounted equipment.
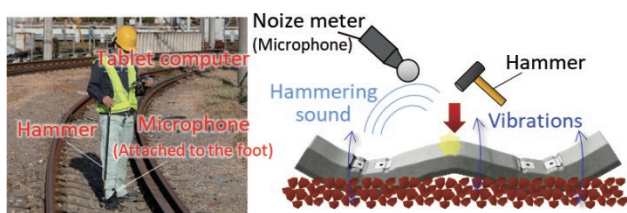

Fig. 7   PC sleeper hammering test technology

3.3   Evaluating structure conditions

3.3.1   Bridge vibration acceleration monitoring

Bridge vibrations generated when a train passes are used to evaluate the ride comfort and running performance of vehicles and the deterioration and damage of bridges; therefore, various measurement and evaluation technologies have been studied in relation to vibrations (Fig. 8). RTRI has been working on the sophistication

of acceleration measurement and evaluation methods that have been performed by attaching accelerometers to bridges. In addition, RTRI has developed an algorithm to estimate the deflection (i.e., displacement) and the reinforcing bar stress inside the concrete bridge from the acceleration measurement data while data collection by making the rounds has been omitted by using wireless sensors. This technology has allowed us to determine the necessity of repair or reinforcement of bridges by monitoring them using small and permanently installable acceleration sensors and quantitatively evaluating the bridge performance.
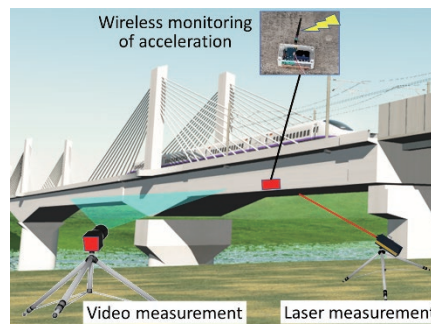
Fig. 8   Bridge vibration measurement technology

3.3.2   Bridge vibration non-contact sensing

A method has been studied to improve the efficiency and safety of measurements by omitting the installation of sensors in high places or near railway tracks by non-contact measurement from a remote position (Fig. 8). This results in the development of U-Doppler, a non-contact vibration measurement system, which is a laser Doppler vibrometer that has an additional function to correct the effect of vibration of the vibrometer due to wind, etc. so that structural vibration measurement outdoors can be highly accurate [7]. It is used for bridge and viaduct inspections that use deflection and natural frequency as indices. In addition, a new dynamic image measurement system using a video camera has been developed that can synchronously measure the vibrations of any number of points in the video [8]. In the future, we plan to work on the sophistication of bridge inspection and condition monitoring by taking advantage of laser measurement, which can measure micro-vibrations such as micro-tremors with high accuracy, and multi-point synchronous video measurement, which can measure vibrations during train passage.

3.3.3   Detecting the resonance-generating bridge by onboard measurement

RTRI is also working on the development of technology to grasp the dynamic behavior of structures from running vehicles. As the speed of the train increases and the bridge deteriorates, the vibration frequency due to the traveling load of the train and the natural frequency of the bridge approach each other, which may expose a structure to large vibrations due to resonance, and early detection of resonance-generating bridges has become an issue.

Thus, resonance-generating bridges can now be detected by (as shown in Fig. 9) performing onboard measurement of the acceleration of the first car and the last car and detecting the resonance-generated increase in shaking during passage of the last car [9]. We expect that the technology for measuring the characteristics of structures through onboard measurements (which can omit the difficult task of installing sensors on all of the many existing structures) will play a

leading role in condition monitoring of structures in the future.
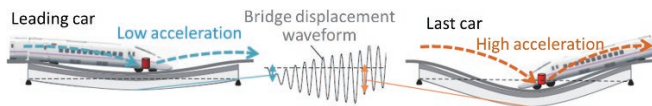
Fig. 9 Detecting the resonance-generating bridge by onboard measurement

4. Future role of experimental and measurement technologies

Experimental and measurement technologies are indispensable for reproducing and grasping various phenomena that occur in the actual railway field, and will continue to play an important part in elucidating railway-specific phenomena, investigating accident causes, establishing the inspection and evaluation standards, and proposing countermeasures against accidents and disasters. From now, we plan to proceed with the following while strengthening the links between experimental technology and numerical simulation technology: (i) improving hybrid experiment/simulation technology that more faithfully reproduces real phenomena by combining experimental equipment and numerical simulation, (ii) improving numerical models with basic data and verification data prepared by RTRI's original experimental technology, and (iii) improving the operational efficiency of large-scale test equipment by linkage with a numerical laboratory (i.e. virtual experimental equipment by numerical simulation) (Fig. 10).

As for measurement technology, we will develop it into a system for providing actual railway field information in a railway digital twin.

RTRI is working on the development of a virtual railway test line that reproduces a railway in computer space[1]. By associating it with condition monitoring data in near real-time, we would like to develop it into a digital twin as a dynamic model that faithfully reproduces the actual railway route. We would like to improve the efficiency of railway maintenance and ensure safety by constructing the system that catches the signs of equipment deterioration and accidents that could occur in the real railway field at an early stage, evaluates the condition by simulation on the virtual railway test line, and conveys the coping method to the railway in real space by using more advanced sensing and monitoring technologies and data communication technologies.
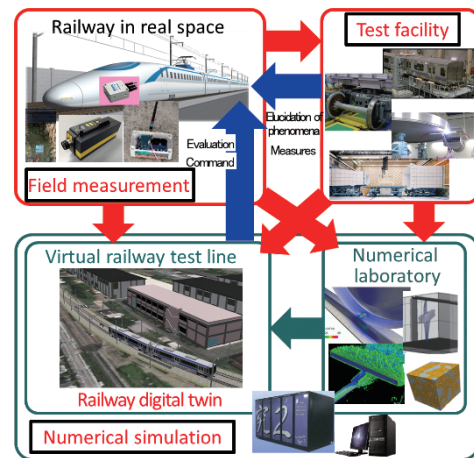
5. Conclusion

This paper presented the latest large-scale test equipment developed by RTRI for the elucidation of railway-specific phenomena, and vibration measurement technology for tracks and structures aimed at understanding and monitoring the real conditions of railways in the field. In addition to the topics presented in this paper, RTRI has also constructed measurement technologies that utilize various indoor and on-track test technologies and digital technologies such as image analysis, AI, and wireless/networking technologies. We are commit-

Fig. 10 Linkage between experimental and measurement technologies and simulation

ted to the innovation of railways and always welcome input, cooperation and feedback from other researchers in this field.

References

[1] Uehan, F., "Research and Development on Railway Simulators," *Quarterly Report of RTRI*, Vol. 62, No. 2, pp. 88-91, May 2021.

[2] Koyama, T., "Development of High-speed Test Facility for Pantograph/OCL Systems," *Quarterly Report of RTRI*, Vol. 63, No. 2, pp. 128-132, May 2022.

[3] IDO, A., "RTRI Large-Scale Low-Noise Wind Tunnel," *Ascent*, No. 9, https://www.rtri.or.jp/eng/publish/ascent/ascent09.html, October 2021.

[4] Miyachi, T., "Low-Noise Moving Model Test Facility Completed at RTRI," *Ascent*, No. 9, https://www.rtri.or.jp/eng/publish/ascent/ascent09.html, October 2021.

[5] Iwasawa, N., et.al., "Basic Concepts of Buried Wireless Sensor under Ballasted Layer," *Proceedings of ICSNC2019*, No. 4346, November 2019.

[6] Matsuoka K., Watanabe T., "Application of a frequency based detection method for evaluating damaged concrete sleepers," *Advances in Structural Health Monitoring*, https://www.intechopen.com/chapters/64878, December 2019.

[7] Uehan, F., "Development of the U-Doppler Non-contact Vibration Measuring System for Diagnosis of Railway Structures," *Quarterly Report of RTRI*, Vol. 49, No. 3, pp. 178-183, August 2008.

[8] Matsuoka, K., Uehan, F., Kusaka, H., and Tomonaga, H., "Experimental Validation of Non-Marker Simple Image Displacement Measurements for Railway Bridges," *Applied Sciences*, Vol. 11, No. 15, 7032, https://doi.org/10.3390/app11157032, July 2021.

[9] Matsuoka, K., Watanabe, T., Uehan, F., "Resonant Bridge Detection Method by On-board Measurement," *Quarterly Report of RTRI*, Vol. 61, No. 2, pp. 133-138, May 2020.

Author

Fumiaki UEHAN, Dr. Eng.
Director, Head of Railway Dynamics Division
Research Areas: Structural Mechanics, Measurement Engineering

Heat Resistance Effect Evaluation Method of Copper-based Sintered Alloy Base Material on Friction Coefficient

Hisanori NISHIMORI　　　**Yasushi KARINO**　　　**Takafumi TSUJI**
Braking Systems Laboratory, Vehicle Technology Division

Shogo SAKAI
Braking Systems Laboratory, Vehicle Technology Division (Former)

Train mechanical brakes convert kinetic energy into friction heat, which is emitted, to obtain braking force. Therefore, when stopping distance needs to be shortened to improve safety, the heat load on the brake increases. Friction material used for the brake is then required to have a thermally stable friction coefficient in addition to the heat capacity capable of accepting a given kinetic energy. This study therefore focuses on a method for evaluating brake friction materials used in Shinkansen, especially copper-based sintered alloy. We conducted experimental investigations, such as thermal analysis of solid lubricants and measurement of friction coefficient using a high-temperature friction test apparatus. This paper introduces the developed evaluation method of the heat resistance of base materials on the experiment results.

***Key words**: brake friction material for Shinkansen, solid lubricants, base material of friction material, thermal analysis, friction coefficient, high-temperature friction apparatus*

1. Introduction

Train mechanical brakes convert kinetic energy into friction heat which is then released. The maximum running speed of a train depends heavily on its mechanical brake performance, therefore, when shortening stopping distances to improve safety, heat load in the brakes increases. Friction material used for the brakes then needs to have a thermally stable friction coefficient in addition to a heat capacity capable of enduring a given kinetic energy.

To select friction material which satisfies these requirements, we generally perform brake tests using a full-size bench tester. In the bench test, we evaluate braking performance such as deceleration, stopping distance and friction coefficient, and verify properties based on various specifications such as temperature of wheels, discs and friction materials. Here, when the friction coefficient at high temperature conditions does not meet the target value, a friction material which is expected to have better high temperature property is prepared, and full-size bench tests (hereinafter referred to as 'bench tests') are repeated until the friction material which satisfies the target braking performance is found.

Thus, while bench tests are indispensable for final evaluation of braking performance, the method described above to evaluate friction coefficient at high temperature conditions requires enormous time and effort. Therefore, we examined the applicability of a high-temperature friction test apparatus capable of measuring friction coefficients at arbitrary temperatures from room temperature to 1100°C [1, 2, 3], as an easier method for evaluating friction materials.

This study experimentally investigates and analyzes the relationship between thermal changes of solid lubricants and friction coefficients for copper-based sintered alloy (hereinafter referred to as friction materials) used as brake friction materials of Shinkansen, by focusing on changes in solid lubricants and base materials contained in friction materials observed in the structure of friction materials subjected to heat load. Using the results of the investigation and analysis, we develop a method to evaluate effect of heat resistance of base materials on friction coefficient [4].
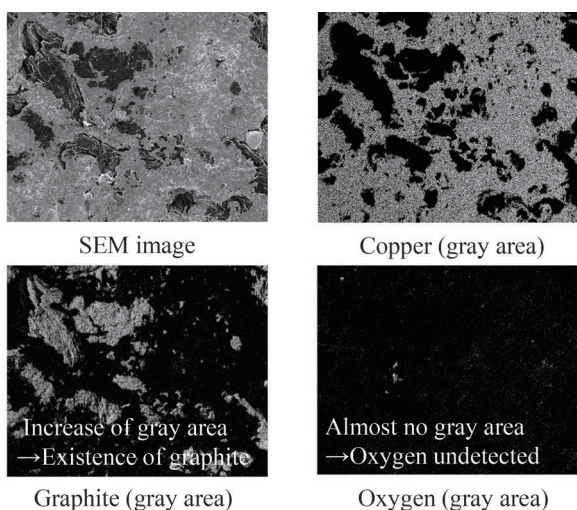
2. Structure observation of friction material subjected to heat load

Copper-based sintered alloys are composed of copper-based base materials, solid lubricants, friction modifiers, etc. The blending ratio of each component is adjusted to obtain the desired friction coefficient value. In order to investigate the change of each component constituting the friction material caused by frictional heat, we prepared new friction materials which had not been subject to heat load, and friction materials subjected to heat load by bench tests or atmospheric furnace heating, and carried out structure analyses near the surface on each.

2.1 Friction material subjected to heat load by bench test

A scanning electron microscope (SEM) and elemental analysis by energy dispersive X-ray spectroscopy (EDX) were carried out to analyze and observe the structure of the friction materials. As objects of elemental analysis, we selected three elements: graphite (carbon) used for solid lubricants, copper which is the main component of the base material, and oxygen assuming the oxidation phenomenon by heat load. Figure 1 shows the structure observation and elemental analysis of results on the surface of the friction materials before and after heat loading in bench tests. It is noted that the friction material after the bench test was selected from those which had a temperature history of 850°C or higher during braking.

From Fig. 1, comparing the detection state of each element before and after the heat load by the bench test, the gray area detecting graphite, decreased due to the heat load. This suggests that the amount of graphite decreased due to the heat load. On the other hand, oxygen was almost undetectable before the heat load. But after the heat load, the gray detection area increased drastically. Since the detection area of oxygen after heat load also coincides with the detection area of copper after the heat load, it is presumed that copper changed to copper oxide under the heat load.

SEM image   Copper (gray area)

Increase of gray area   Almost no gray area
→Existence of graphite   →Oxygen undetected

Graphite (gray area)   Oxygen (gray area)

(a) Before heat load

SEM image   Copper (gray area)

Coincident gray area
with that of oxygen
→Change to copper oxide

Decrease of gray area   Increase of gray area
→Decrease of graphite   →Increase of oxygen

Graphite (gray area)   Oxygen (gray area)
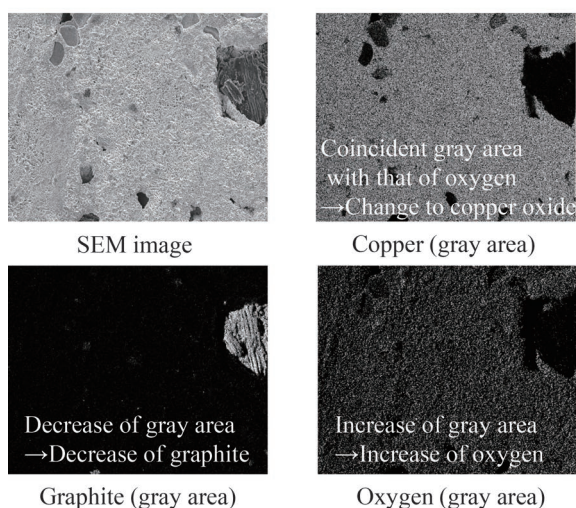
(b) After heat load (After temperature history of 850°C or higher)

Fig. 1 Structure observation and elemental analysis results on the surface of the friction materials before and after bench tests

2.2 Friction material subjected to heat load by atmospheric furnace heating

An investigation of the friction material subjected to heat loading in the bench tests revealed that the amount of graphite contained in the friction material decreased with heat load, and copper changed to copper oxide. Assuming that these changes through heat load affect the temperature dependence of the friction coefficient, it is necessary to investigate change in friction material by temperature in more detail. However, it is very difficult to control the temperature of the friction material in the bench test because of the temperature rise caused due to frictional heat. Therefore, as a heat load method to replace bench tests, we adopted a method of giving heat load by heating the friction material to the target temperature using a furnace under an atmosphere (hereinafter referred to as an 'atmospheric furnace'). We then observed structure by SEM and elemental analysis by EDX on the surface of the friction material after heating in the atmospheric furnace. Table 1 shows the condi-

Table 1 Heat load conditions for atmospheric furnace heating

Heating temperature	R.T., 400°C, 400°C and after, every 100°C until 1000°C
Heating atmosphere	Atmosphere
Holding time	15 minutes (After the temperature inside the furnace reached the target value, friction material was put into the furnace)
Cooling method	Natural cooling outside the atmospheric furnace under atmosphere

tions for the atmospheric furnace heating used to add heat load to the friction material. The friction material was put into the furnace after the temperature inside the furnace reached the target value, and then kept isothermally in the furnace for 15 minutes, before being taken out of the atmospheric furnace. After the friction material was removed, it was cooled in the atmosphere. Elemental analysis by EDX was carried out for graphite, copper, and oxygen.
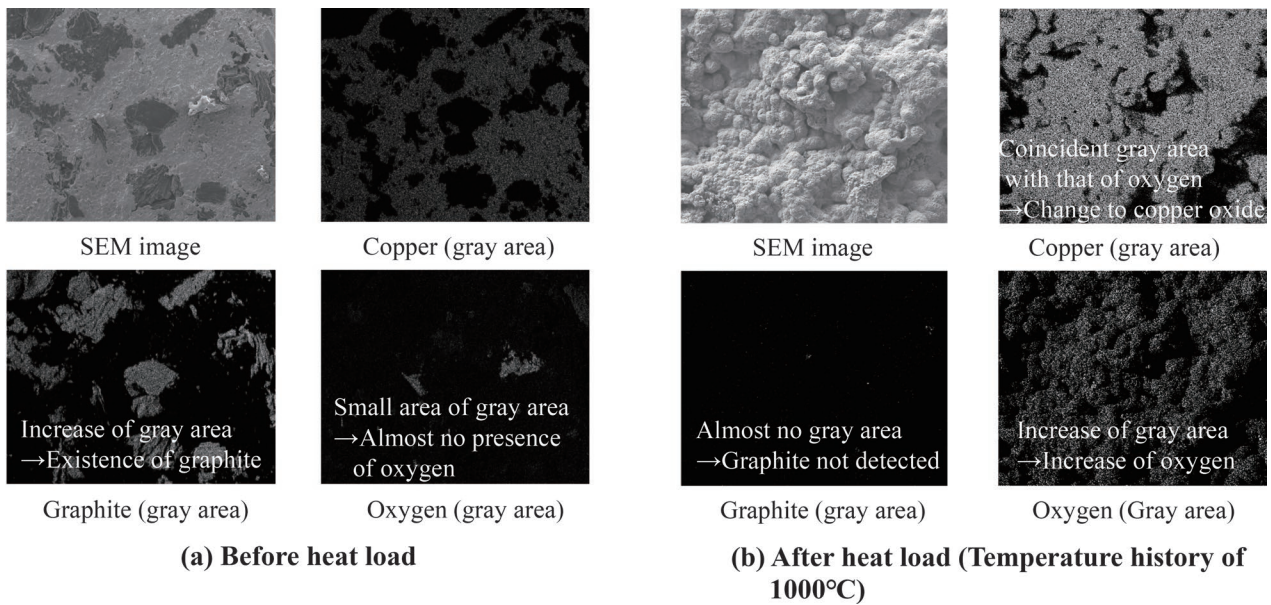
Figure 2 shows the structure observation and elemental analysis results on the surface of the friction materials before heat loading, and after being subjected to maximum heat load reaching 1000°C as a representative example of the structure analysis results. Figure 2 shows that graphite has a gray detection area from before heat loading up to a heat load temperature (hereinafter referred to as the 'hl-temperature') of 600°C, but at the hl-temperature of 700°C, the gray detection area decreases sharply. The detection of graphite was almost undetectable at the hl-temperature of 1000°C as shown in Fig. 2(b). On the other hand, the shades of gray became darker as the heat load temperature increased. Furthermore, the detection region of oxygen coincided with the detection region of copper, and the same phenomenon as had occurred after heat loading with the bench test was observed. Figure 3 shows the results of structure observation and elemental analysis by electron probe micro analyzer (EPMA) for friction materials before heat loading and after being subjected to heat loading reaching 1000°C. This elemental analysis was carried out from the surface to the depth direction. In the friction material subjected to the hl-temperature of 1000°C, graphite was not detected at 500 μm depth from the surface. In this region, the detection intensity of oxygen is stronger than that in regions deeper than 500 μm, and conversely, the detection intensity of copper is weaker than that in regions deeper than 500 μm. Accordingly, it seems that copper oxide is formed in the region up to a depth of 500 μm.

From these investigations of the friction material subjected to heat load by atmospheric furnace heating, it was found that graphite sharply decreases in the 600°C to 700°C boundary, and that copper gradually changes to copper oxide under heat loading. Also, for friction materials subjected to a heat load of 1000°C, it was confirmed that the change of the friction material structure extended up to a depth of 500 μm from the surface.
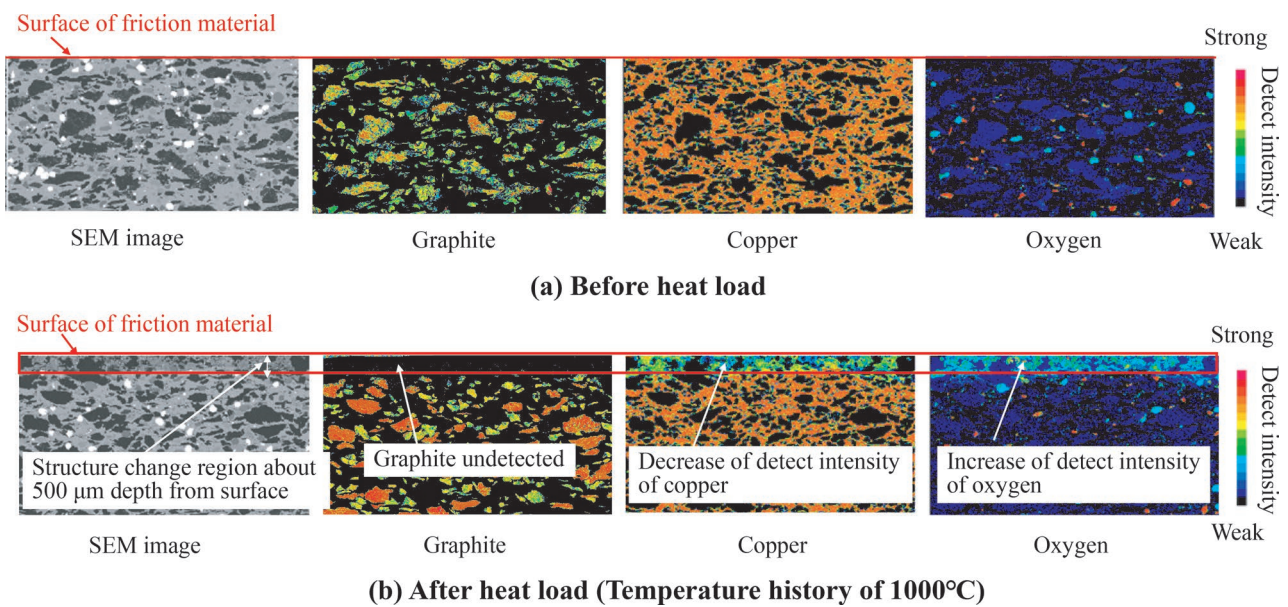
3. Thermal analysis of solid lubricants

A structural analysis of friction materials subjected to heat loading revealed that graphite used for solid lubricants abruptly decreases from a high temperature and copper used for base material

SEM image   Copper (gray area)

Increase of gray area   Small area of gray area
→Existence of graphite   →Almost no presence
                                                    of oxygen

Graphite (gray area)   Oxygen (gray area)

(a) Before heat load

Coincident gray area
with that of oxygen
→Change to copper oxide

SEM image   Copper (gray area)

Almost no gray area   Increase of gray area
→Graphite not detected   →Increase of oxygen

Graphite (gray area)   Oxygen (Gray area)

(b) After heat load (Temperature history of 1000°C)

Fig. 2   Structure observation and elemental analysis results on the surface of the friction materials before and after atmospheric furnace heating (representative example)

Surface of friction material

SEM image   Graphite   Copper   Oxygen

(a) Before heat load

Surface of friction material

Structure change region about
500 μm depth from surface

Graphite undetected

Decrease of detect intensity
of copper

Increase of detect intensity
of oxygen

SEM image   Graphite   Copper   Oxygen

(b) After heat load (Temperature history of 1000°C)

Fig. 3   Structure observation and elemental analysis results of the friction materials from surface to depth direction by EPMA

changes to copper oxide. Graphite plays an important role in securing a stable friction coefficient, therefore a decrease in graphite would have a great influence on the change in friction coefficient. Then, in order to investigate the change due to heat load, in addition to graphite used in brake friction material for Shinkansen for this study, thermal analyses were carried out on a total of 4 kinds of solid lubricants (including graphite): hexagonal boron nitride, molybdenum disulfide, and tungsten disulfide used in other industrial fields.

3.1 Summary of thermal analyses

Using the method specified in JIS K0129:2005 (General rules

for thermal analysis), we investigated thermal changes of solid lubricants under atmosphere conditions [5]. Graphite and hexagonal boron nitride were analyzed by simultaneous thermogravimetry and differential thermal analysis (TG-DTA). On the other hand, molybdenum disulfide and tungsten disulfide were analyzed by simultaneous thermogravimetry and differential thermal analysis and mass spectrometry (TG-DTA/MS). Table 2 shows the thermal analysis conditions.

3.2 Results of thermal analysis

Figure 4 shows the results of the thermal analysis of graphite; Fig. 5, that of hexagonal boron nitride; Fig. 6, that of molybdenum

Table 2   Thermal analysis conditions (partly modified [4])

| Sample conditions		Measurement items			Atmospheric conditions		Temperature conditions	
Sample (powder)	weight	TG[*1]	DTA[*1]	MS	Atmospheric gas	Gas flow rate	Temperature range	Temperature rising speed
Graphite	20 mg	○	○	-	Atmosphere			
Hexagonal boron nitride	20 mg	○	○	-	Atmosphere	200 ml/min	Room temperature to 1500°C [*3]	5°C/min
Molybdenum disulfide	2.7 mg	○	○	○	Pseudo-atmosphere[*2]			
Tungsten disulfide	2.7 mg	○	○	○	Pseudo-atmosphere[*2]			

*1 As a reference substance, α-alumina was selected which reacts no physical and chemical change within the measurement temperature range (room temperature to 1500°C).

*2 With the limitation of configuration of the measuring device, pseudo-atmosphere (20%O_2-He) by mixing the active gas (O_2) and inert gas (He) was selected.
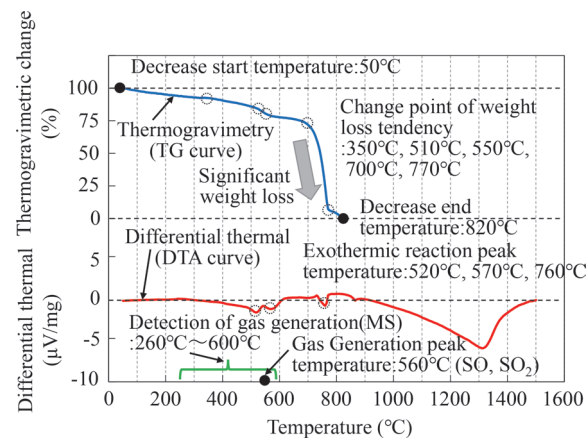
*3 The maximum temperature range that can be measured with a measuring device was selected.
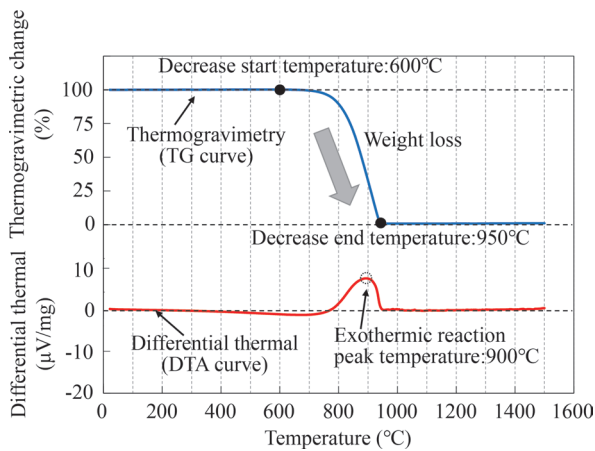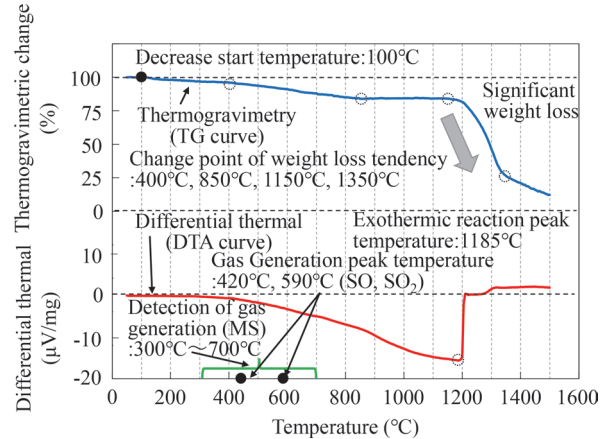

Fig. 4   Result of thermal analysis of graphite (partly modified [3])
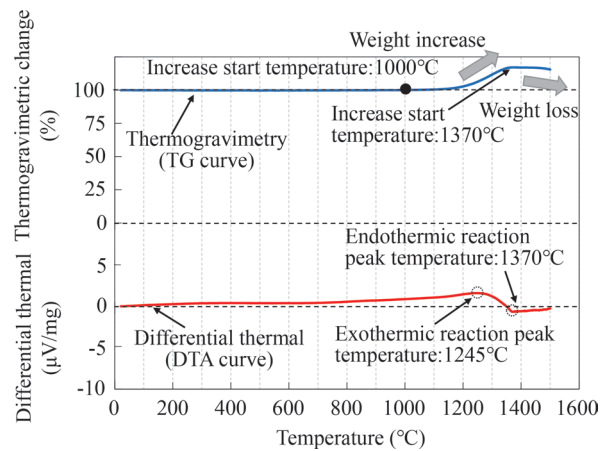
Fig. 5   Result of thermal analysis of hexagonal boron nitride (partly modified [4])

Fig. 6   Result of thermal analysis of molybdenum disulfide (partly modified [4])

Fig. 7   Result of thermal analysis of tungsten disulfide (partly modified [4])

disulfide; and Fig. 7, that of tungsten disulfide.

(a) Graphite

The TG curve shown in Fig. 4 shows that graphite begins to decrease in weight at 600°C, the weight loss becomes remarkable from around 700°C, and thermogravimetric change becomes 0% at 950°C. This means that all graphite disappears at 950°C, ceasing weight loss. The DTA curve shows that an exothermic reaction occurs from 800°C to 950°C, peaking at 900°C. From these TG-DTA results, it seems that graphite combines with oxygen in the analyzer from 600°C generating a combustion reaction, and the weight de-

creases due to graphite changing to carbon monoxide or carbon dioxide.

(b) Hexagonal boron nitride

The TG curve in Fig. 5 shows that hexagonal boron nitride does not change in weight until 1000°C before the weight increases from 1000°C, the weight gradually begins to decrease after reaching a maximum value at 1370°C. In the DTA curve, moderate peaks which seemed to be an exothermic reaction at 1245°C and an endothermic reaction at 1370°C, are observed. From the results of TG-DTA, we verified that hexagonal boron nitride is thermally stable without chemical and physical changes up to 1000°C even in atmosphere conditions.

(c) Molybdenum disulfide

As shown in the TG curve in Fig. 6, molybdenum disulfide begins to decrease in weight at 50°C, and changes in weight reduction are observed at 5 temperature points: 350°C, 510°C, 560°C, 700°C, and 770°C. Weight decreases in particular at 700°C, and the thermogravimetric change falls to 0% at 820°C. In the DTA curve, peaks in endothermic reaction are observed at 520°C, 570°C, 760°C. In addition, gas is detected from 260°C to 600°C in MS measurement, with a peak in gas generation observed at 540°C. Since the mass spectrum m/z of this generated gas is 48 and 64, it is presumed that the generated gases are sulfur monoxide and sulfur dioxide. According to the results of the TG-DTA/MS, in the temperature range below 600°C, the point in temperature at which weight falls and the temperature at which peaks in endothermic reaction are observed are close. Furthermore, the peak of gases estimated to be sulfur monoxide and sulfur dioxide is detected at 540°C. Therefore, molybdenum disulfide in pseudo atmosphere condition is considered to combine with oxygen in the analyzer from 260°C and to change into oxide gradually as the temperature rises.

(d) Tungsten disulfide

The TG curve in Fig. 7 shows that tungsten disulfide begins to decrease in weight at 100°C, and changes in weight reduction are observed at 4 temperature points: 400°C, 850°C, 1150°C, 1350°C. Especially, it is noted that after 1150°C, weight falls significantly. In the DTA curve, the endothermic reaction occurs from 400°C to 1200°C, and the peak of the endothermic reaction is observed at 1185°C. Furthermore, in the measurement of MS, gas is detected from 300°C to 700°C, and especially the peaks of gas generation are observed at 420°C and 590°C. Since the mass spectrum m/z of the generated gases are 48 and 64 respectively, it is presumed that the generated gases are sulfur monoxide and sulfur dioxide. TG-DTA/MS results show that the change in weight reduction tendency and the initiation of the endothermic reaction are observed at 400°C, and the peaks of gases estimated to be sulfur monoxide and sulfur dioxide are detected at 420°C. Hence, tungsten disulfide in pseudo atmosphere conditions is considered to combine with oxygen in the analyzer from 300°C and to gradually change into the oxide with the temperature rise.

4. Evaluation method for heat resistance of base material of friction material

The thermal analysis results of solid lubricants in this study revealed that the thermal change start temperature of hexagonal boron nitride is highest, and hexagonal boron nitride is a solid lubricant thermally stable up to 1000°C. This fact suggests that by making a friction material containing hexagonal boron nitride instead of graphite blended in the friction material, it is possible to evaluate the base material heat resistance of copper-based sintered alloy friction

material, which has been difficult to evaluate until now, because of the change in friction coefficient caused by thermal changes in solid lubricants. The possibility of evaluating heat resistance of friction material base material was then examined by producing friction material applying hexagonal boron nitride as a solid lubricant to carry out high-temperature friction tests.

4.1 Summary of high-temperature friction test

As a first step to evaluate heat resistance of friction material base material, material A containing graphite as a solid lubricant and material B containing hexagonal boron nitride as a solid lubricant were prepared. We then conducted high-temperature friction tests to obtain a temperature range in which mean friction coefficient of material A and material B change and compared them. Next, material C which contains hexagonal boron nitride as a solid lubricant and use a base metal different from material B was prepared. Using material C, we carried out heat resistance evaluation of the friction material base material. The high-temperature friction test conditions are shown in Table 3.

Table 3   Heat load conditions by atmospheric furnace heating (partly modified [1])

Surface pressure	1.1 MPa
Frictional area	11 cm^2
Effective radius	35 mm
Frictional speed	0.11 m/s
Test temperature	R.T., 200°C, 400°C 400°C and after, every 100°C until 1100°C
Test time	60 seconds
Number of tests	3 times (after friction coefficient stabilized)

## 4.2 Organization of test results

To more clearly grasp the change tendency of the mean value of friction coefficient (hereinafter referred to as mean friction coefficient) at each test temperature, the variation rate of mean friction coefficient α is taken as an index. This index represents the degree in the mean coefficient of friction, f_e, at other test temperatures based on the mean friction coefficient f_m at a specific temperature. Equation (1) shows the formula for calculating the average coefficient of friction change.

$$\alpha = \left(\frac{f_e}{f_m} - 1 \right) \times 100 \ (\%) \tag{1}$$

Since the thermal change start temperature (thermogravimetric change) of graphite is 600°C, the mean friction coefficient at 600°C of each friction material is used as the standard value.

## 4.3 Relationship between thermal change of solid lubricant and friction coefficient

Figure 8 shows the results of the high-temperature friction test on material A and the TG-DTA of graphite. As shown in Fig. 8, the variation rate of the mean friction coefficient (hereinafter referred to as variation rate α) is almost constant as the temperature rises from 200°C to 500°C. Then, variation rate α changes to positive at 700°C, which means that the friction coefficient increases. Thereafter, after
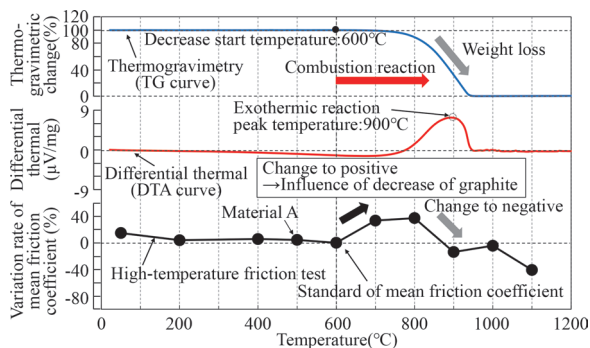
Fig. 8 Result of high-temperature friction test of material A and relationship between friction coefficient and thermal change of graphite (partly modified [4])

reaching maximum value at 800°C, variation rate α changes significantly to negative at 900°C, which indicates a marked fall in the friction coefficient. The temperature change from 600°C to 700°C, in which the temperature change of the variation rate α changes from negative to positive, corresponds to the temperature range where the combustion reaction of graphite was observed in TG-DTA results. The reason why the variation rate α reaches a maximum at 800°C seems to be influenced by the decrease in graphite due to the combustion reaction.

Figure 9 shows the result of high-temperature friction tests on material B. Figure 9 also describes the TG-DTA of hexagonal boron nitride and the test result of material C explained in the next paragraph. As shown in Fig. 9, the variation rate α is constant in the temperature range of 200°C to 500°C regardless of temperature rise. Above 700°C, the variation rate α becomes negative, which means that the friction coefficient decreases with the increase in temperature, followed by a more marked decrease above 900°C. The results of TG-DTA show that hexagonal boron nitride is thermally stable up to 1000°C, thus, fluctuations in the variation rate α below 1000°C seem to be due to the effect of heat resistance of the base material, and not the effect of hexagonal boron nitride used as a solid lubricant. Thus, comparison of variation rate α for materials A and B, obtained by high-temperature friction, clarified that the difference in thermal change of the solid lubricant contained in the friction material has a major influence.
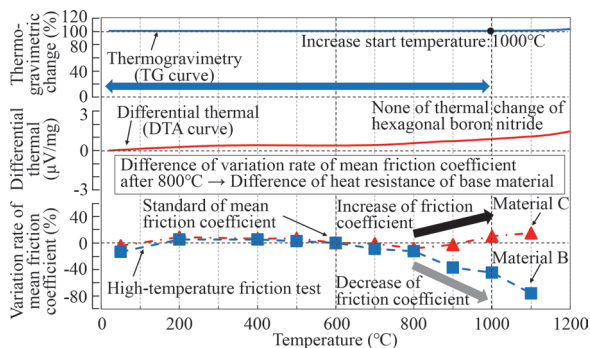
Fig. 9 Comparison of result of high-temperature friction test between material B and material C (partly modified [4])

4.4 Evaluation method for heat resistance of base material of friction material

Figure 9 shows the result of high-temperature friction tests of material C. By comparing the variation rate α of material B with that of material C, it is found that the variation rate α with respect to temperature shows the same tendency in both materials from room temperature to 800°C. However, at temperatures above 900°C, the variation rate α of material B is negative which means that the friction coefficient decreases. On the other hand, in the same temperature range, the variation rate α of material C is positive. It was clarified that the friction coefficient of material C remains the same or higher as that at room temperature up to higher temperature range than material B. From this result, by applying hexagonal boron nitride to the solid lubricant, it seems to be possible to evaluate the heat resistance of base material of friction material using the variation rate α of the friction coefficient as an index.

5. Conclusions

Although full-size bench tests are indispensable for final brake performance evaluations, they are relatively labor intensive and time consuming if the purpose of the evaluation focuses only on performance of friction material in high temperature conditions.

This study therefore experimentally investigated and analyzed using structure analysis of the friction material, thermal analysis of solid lubricants contained in the friction material, and measurement of friction coefficient by high-temperature friction tests as a method for evaluating friction materials more easily than through full-size bench tests. As a results, it revealed that the thermal change of solid lubricant affects the change in the friction coefficient. In addition, by using a solid lubricant that does not cause a thermal change in high temperature conditions, it is considered that the effect of the base material heat resistance of the friction material on friction coefficient can be evaluated, and we proposed a heat resistance evaluation method of base material by using high-temperature friction tests for friction materials applying hexagonal boron nitride thermally stable up to 1000°C to a solid lubricant. From the results of the high-temperature friction tests on friction materials of different base materials, it was clarified that the difference in base material has an influence on the difference in friction coefficient, and it revealed that using this proposed method, heat resistance evaluation of friction material base material was possible.

In the future, we would like to improve the validity and reliability of the proposed method as an evaluation method of friction materials by repeatedly comparing and verifying with test results from full-size bench tests. By extension, we would like to utilize this evaluation method as a basic test for friction material selection before full-size bench tests in the development process of the brake friction materials for Shinkansen.

References

[1] Matsuoka, K. and Nishimori, H., "Measurement method of friction coefficient of the brake friction materials at arbitrary temperature," *J-Rail 2017*, S1-2-3, 2017 (In Japanese).

[2] Nishimori, H. and Matsuoka, K., "Method for Evaluating Brake Friction Materials Using High-temperature Friction Test Apparatus," *Quarterly Report of RTRI*, Vol. 60, No. 2, pp. 90-96, 2019.

[3] Karino, Y., Nishimori, H., Sakai S. and Fujita, K., "Recent Evaluation Techniques for Brake Friction Materials for Shinkansen Vehicle," *Journal of Japanese Society of Tribologists*, Vol. 65, No. 12, pp. 730-735, 2020 (In Japanese).

[4] Nishimori, H., Karino, Y., Sakai, S, Tsuji, T. and Kitazawa, Y., "New Proposal for Evaluating Heat Resistance of Base Materials Composing Copper-based Sintered Alloys," *J-Rail 2020*, S1-2-2, 2020 (In Japanese).

[5] Japanese Standards Association, "General rules for thermal analysis," *JIS K0129*, 2005 (In Japanese).

Authors

Hisanori NISHIMORI
Assistant Senior Researcher, Braking Systems Laboratory, Vehicle Technology Division
Research Areas: Brake Friction Materials

Takafumi TSUJI
Researcher, Braking Systems Laboratory, Vehicle Technology Division
Research Areas: Brake Friction Materials

Yasushi KARINO
Senior Chief Researcher, Head of Braking Systems Laboratory, Vehicle Technology Division
Research Areas: Brake Friction Materials

Shogo SAKAI
Researcher, Braking Systems Laboratory, Vehicle Technology Division (Former)
Research Areas: Brake Friction Materials

Development of Active Bogie Steering System to Improve Curving Performance

Takashi KOJIMA   **Yasuhiro UMEHARA**
Vehicle Dynamics Laboratory, Vehicle Technology Division

Takatoshi HONDO
Vehicle Mechanics Laboratory, Railway Dynamics Division

This paper presents an active steering system designed to ensure both the curving performance and running stability of a vehicle. Electro-hydraulic actuators installed in place of anti-yaw dampers generate a yaw moment between the carbody and bogie. The system detects curves with gyroscopes mounted on the vehicle. This configuration enables the reduction of wheel/rail lateral force without requiring complicated mechanical links in the bogies. The actuators also work as anti-yaw dampers during high-speed running to ensure running stability.

Key words: *bogie, steering control, curving performance, lateral force, electro-hydraulic actuator*

1. Introduction

In railway bogies, high running stability and higher curving performance are required as a basic dynamic performance. Higher bogie rotational resistance, higher primary suspension stiffness, longer wheelbase, and smaller wheel tread gradient provide higher running stability. However, they all result in lowering curving performance. Specifications for these are generally selected according to the running speed and curvature profile of the route. For vehicles traveling on both high-speed sections and in sharp curve sections, however, it is difficult to select satisfactory specifications. This is especially an issue for vehicles offering services which run directly between Shinkansen and conventional lines. The higher the running speed on a Shinkansen line, the more difficult it becomes to optimize the specifications. Hence, the authors have developed an active bogie steering system. The system applies a steering moment between the carbody and bogie frame in sharp curves to improve curving performance. In addition to the steering moment, the system functions as an anti-yaw damper at high speeds to ensure running stability.

## 2. Configuration of the steering system

2.1 Steering mechanism

There have already been many studies on railway steering bogies. Most of them propose methods to steer the wheelset relative to the bogie frame. One of them is a wheelset steering mechanically linked to the bogie angle [1][2]. This bogie has been put into practical use on Japanese conventional lines. These bogies are realized by equipping the primary suspension with mechanical links. The link leads to a reduction of the attack angle and wheel/rail lateral force. On the other hand, Matsumoto et al. [3] proposed a method to steer a bogie frame relative to a carbody. This "active bogie steering" can comprise primary suspension equivalent to conventional bogies. The active bogie steering may be suitable for ensuring reliability at high speeds on Shinkansen lines. This section of the paper describes our investigation of active bogie steering, and our proposal of a steering system that functions as an anti-yaw damper when running at high speeds.

2.2 Steering moment generation mechanism

In order to mount a steering device on the bogie, a certain amount of space is required. However, available space on most bogies is limited. In addition, the positions at which to apply steering force should be distant from the center of the bogie. In this paper, we propose to install an actuator instead of an anti-yaw damper. The actuator generates a force to control steering and functions as a normal anti-yaw damper when not being controlled.

Vehicles for services which run directly between Shinkansen and conventional lines [4] are equipped with two anti-yaw dampers on each side of each bogie. One of the two dampers is a normal damper, and the other is a switchable damper. On a Shinkansen line, the switchable dampers switch to higher damping to ensure running safety. On a conventional line, the switchable dampers switch to lower damping to improve curving performance.

The steering system proposed in this paper is equipped with actuators in place of the switchable dampers. Figure 1 shows the proposed steering system, which controls the actuators in sharp curves and functions as anti-yaw dampers during high-speed running.
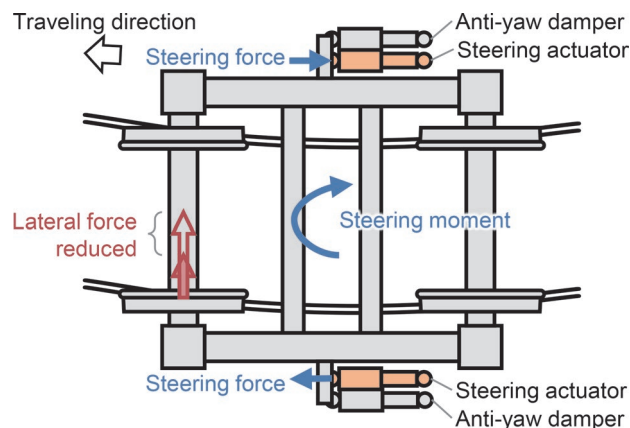
Fig. 1 Steering force control at the anti-yaw damper positions

2.3 Curve detection method

A database consisting of curvatures and locations in the vehicle route may enable a predictive control of the proposed steering system. This method can control steering according to transition curves at the beginning and end of curves but requires maintenance of a database. On the other hand, onboard inertia sensors can estimate current curvature from the vehicle's motion. In this method, there is a delay in recognizing curves which weakens the effect of reducing lateral force on transition curves. However, this method has the advantage of simplifying the system configuration. By using an onboard sensor method, we focused on improving the curving performance on circular curves.

3. Vehicle running simulation for studying specifications

This section of the paper describes how we investigated the basic relationship between the required steering performance and the lateral force reduction effect. The investigation used a numerical simulation with multibody dynamics analysis software. Figure 2 shows the simulation model. In the simulation, we applied a trapezoidal wavy steering force that matches the curvature of the track. Figure 3 shows the lateral force generated on the leading outer wheel when running on a curve. The radius of curvature was 250 m and the running speed was 80 km/h. As shown in Fig. 3, it was found that the lateral force reduction in the circular curve was almost proportional to the given steering force.

We designed a steering actuator based on the simulation result. The design considered the amount of force and responsiveness required to obtain a significant lateral force reduction effect. Furthermore, the design also considered its mountability on an actual vehicle.

4. Prototyping of steering system

Figure 4 shows the system configuration of the active bogie steering system. This system consists of four steering actuators, three gyroscopes, a steering controller, and two bogie angle detection mechanisms. The actuators function as anti-yaw dampers during high-speed running and the gyroscopes sense the yaw rate. The steering controller controls steering while recognizing curves from the yaw rate. The bogie angle detection mechanisms serve to prevent unexpected steering to the opposite side of curves and on straight tracks.
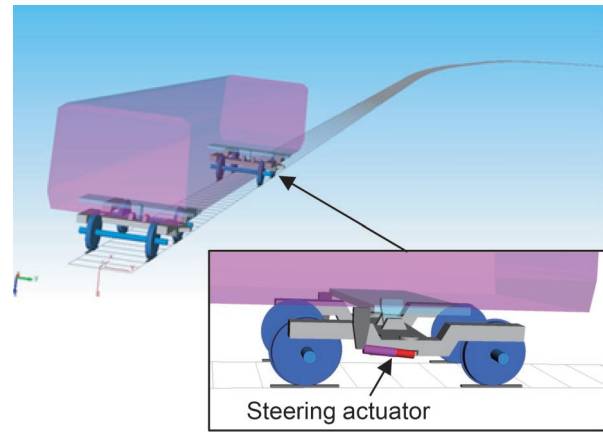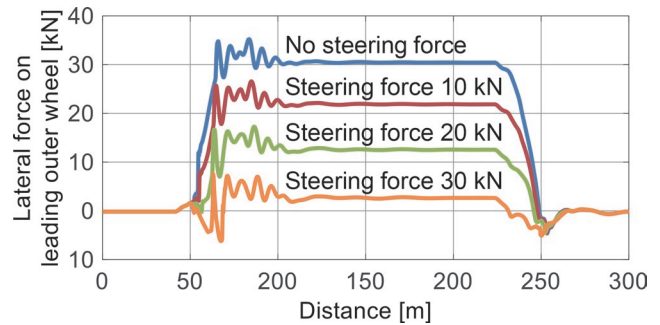

Fig. 2   Simulation model

Fig. 3   Vehicle running simulation result

4.1 Steering actuator

The steering actuator must function both as an actuator and a switchable damper. We therefore adopted and prototyped an electro-hydraulic actuator as a steering actuator. Figure 5 shows the prototype actuator.

The actuator consists of two units for mounting space in a vehicle. One of them is a hydraulic cylinder. The other one is the unit consisting of a motor, a pump, and electromagnetic valves. Three hydraulic hoses connect between two units as shown in Fig. 5. Figure 6 shows the generation flow of contraction and extension force in the hydraulic circuit of the actuator. The steering system switches to one of the following three modes, based on the combination of the states of an electromagnetic proportional relief valve, an electric motor, and two electromagnetic switching valves.

(1) Actuator mode

When the motor operates, the switching valve 1 closes, and the switching valve 2 opens, the pressure on the piston rod side chamber
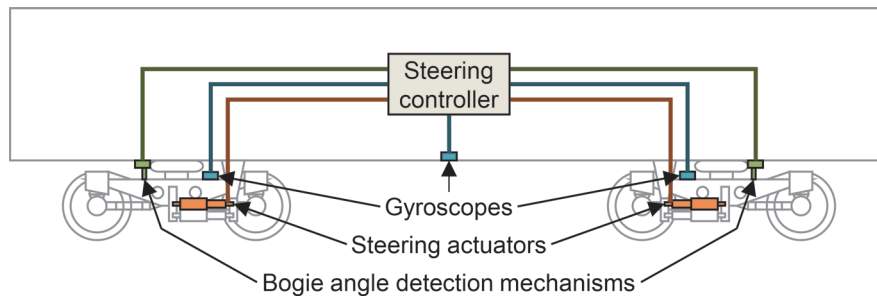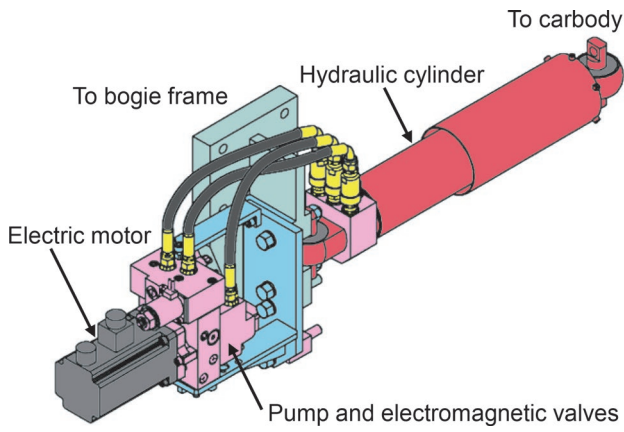

Fig. 4   Configuration of the active bogie steering system

Fig. 5 Steering actuator

(a) Generation of contraction force

(b) Generation of extension force

Fig. 6 Hydraulic circuit of the steering actuator

of the cylinder rises. This sequence generates a contraction force as shown in Fig. 6 (a). When the motor operates, switching valve 1 opens, and switching valve 2 closes, the pressure in both chambers of the cylinder rises. This sequence generates an extension force due to the difference in the pressure-receiving area as shown in Figure 6 (b). It is noted that the proportional relief valve controls the magnitude of the force.

(2) High damping mode

When the motor stops, the proportional relief valve closes, and the switching valves 1 and 2 close, the hydraulic circuit becomes equivalent to a normal damper. The orifice and the relief valve limit the flow of oil extruded during the piston moving. By this sequence, a damping force is generated.

(3) Low damping mode

When the motor stops, the proportional relief valve closes, and the switching valves 1 and 2 open, both chambers of the cylinder communicate to the tank. By this sequence, a minimum damping force is generated.
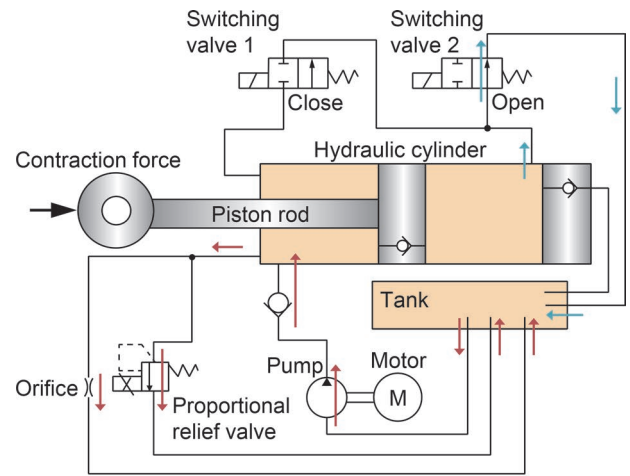
4.2 Steering control algorithm

This section of the paper describes how we designed a simple steering control algorithm that uses only yaw rate and running speed without using any track database.

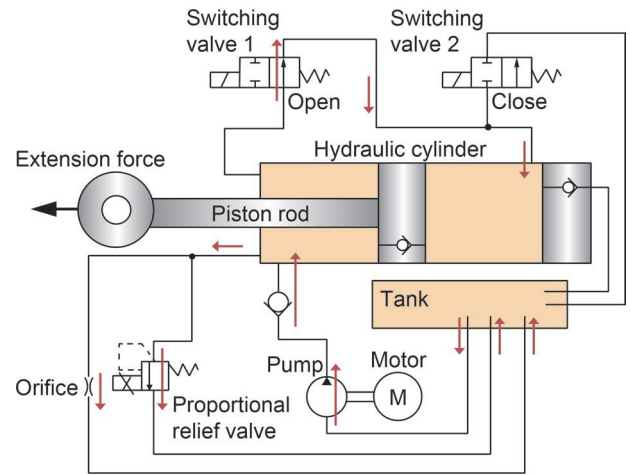#### 4.2.1 Switching of steering actuator mode

The controller switches to the appropriate mode among three modes of the actuators according to running speed. When the running speed is higher than a preset threshold, the controller selects the high damping mode. Both the steering actuator and the anti-yaw damper generate damping force to ensure running stability. When the running speed is lower than the threshold, the controller selects the actuator mode and controls steering. At extremely low speeds, the controller selects the low damping mode and does not control steering. This is because the controller cannot calculate the curvature accurately.

4.2.2 Estimation of curvature

The controller divides the yaw rate by the running speed and applies a low-pass filter to estimate curvature continuously. The low-pass filter removes the vibration component in the yaw rate. When the curvature is larger (i.e., the radius of curvature is smaller) than the preset threshold, the controller enables steering. The con-

troller calculates three curvatures with the yaw rate of the car body, front bogie, and rear bogie. In consideration of safety, steering is enabled only when all three curvatures exceed the threshold.

#### 4.2.3 Calculation of target steering force

In this paper, we assumed that the required steering force is proportional to curvature. The controller multiplies the estimated curvature by a proportionality constant which is experimentally derived. The controller limits the calculated force with a preset maximum force and outputs it as a target steering force.

4.2.4 Health monitoring of gyroscopes

The following equation holds for the low-frequency components of each yaw rate of the carbody and the bogies.

$$\dot{\psi}_C \approx \frac{\dot{\psi}_{B1} + \dot{\psi}_{B2}}{2} \qquad (1)$$

where, $\dot{\psi}_C$ is the yaw rate of the carbody, $\dot{\psi}_{B1}$ is the yaw rate of the front bogie, and $\dot{\psi}_{B2}$ is that of the rear bogie. All passed through a low-pass filter. The controller detects a gyroscope failure when a large discrepancy occurs between both sides of this equation.

Fig. 7 Bogie angle detection mechanism

Fig. 8 Running test for steering performance evaluation
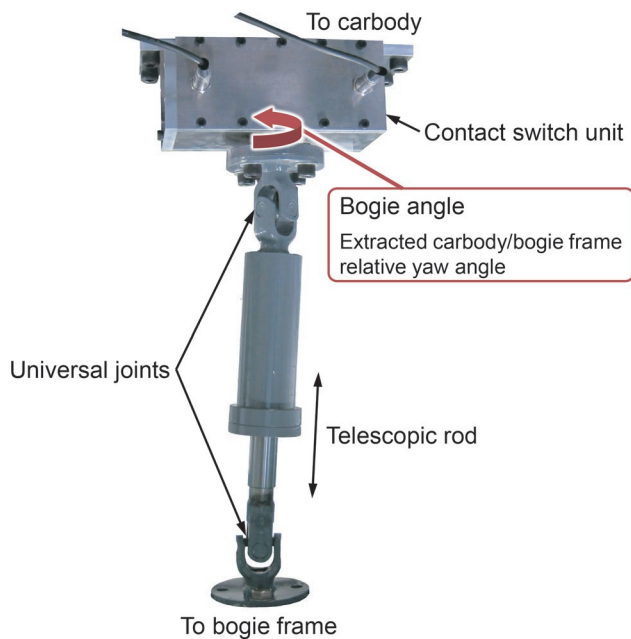
4.3 Bogie angle detection mechanism

If the curvature estimation fails, the system may steer to the opposite side of curves or on straight tracks. The proposed system used a bogie angle detection mechanism to prevent it.

The relative motion between the bogie and the car body has six degrees of freedom. Bogie angle mechanical detection requires some mechanism to extract only the yaw angle out of the motion of six degrees of freedom. This system uses an angle detection mechanism [5] that has a rotation-restricted telescopic rod with universal joints attached to both ends. Figure 7 shows the mechanism. The upper end of this mechanism is connected to the carbody underframe. The lower end is connected to the bogie frame. This mechanism enables detection of the bogie angle even if this mechanism is mounted far from the bogie center.

The steering system can also use the detected bogie angle as an input for steering control. For simplification, however, this system just used it to discern the direction of curves with contact switches. The contact switches are activated at the bogie angle on sharp curves (e.g., radius of curvature smaller than about 500-600 m).

5. Running test on a test line to evaluate steering performance

This section of the paper describes how we evaluated the steering performance of the prototype active bogie steering system. We conducted a running test using a test vehicle with this system on the narrow-gauge test line of the RTRI.

5.1 Test method

Figure 8 shows the running test. This test targeted one bogie in a vehicle for steering control. In the test, two steering actuators and a bogie angle detection mechanism were mounted on a bogie. Yaw dampers were not installed in parallel with the steering actuators, in consideration of the low running speed. The distance between the left and right air springs is 1.98 m. The distance between the left and

right steering actuators is 2.52 m. Focusing on the case where the steering-controlled bogie is the leading bogie, we evaluated the lateral force generated in the leading outer wheel.

5.2 Test results

Figure 9 shows the lateral force generated on the leading outer wheel. As shown in Fig. 9, the steady lateral force on the circular curves during steering control is lower than that without control. Figure 10 shows the average lateral force on the circular curve with a radius of curvature of 160 m. It was found that the steering control reduces the average lateral force by about 60% compared to without control.

6. Roller rig test to evaluate running stability

This section of the paper describes how we evaluated the effect of the prototype active bogie steering system on the vehicle running stability. We conducted a hunting test of a bogie on a roller rig in the RTRI.

6.1 Test method

Figure 11 shows a Shinkansen bogie with a load frame mounted on the roller rig. The load frame with dead weights is equivalent to half of a carbody. The mass of the load frame was 17,000 kg. In the test, there were two conditions: steering actuators installed in parallel with anti-yaw dampers, and switchable anti-yaw dampers installed in parallel with the anti-yaw dampers. Only one anti-yaw damper was attached to the bogie (i.e., only one side) in the test. This was assumed to evaluate the running stability under stricter conditions if one of the anti-yaw dampers had failed. In the test, the switchable anti-yaw dampers and steering actuators were set under two conditions, of a low damping mode and a high damping mode.
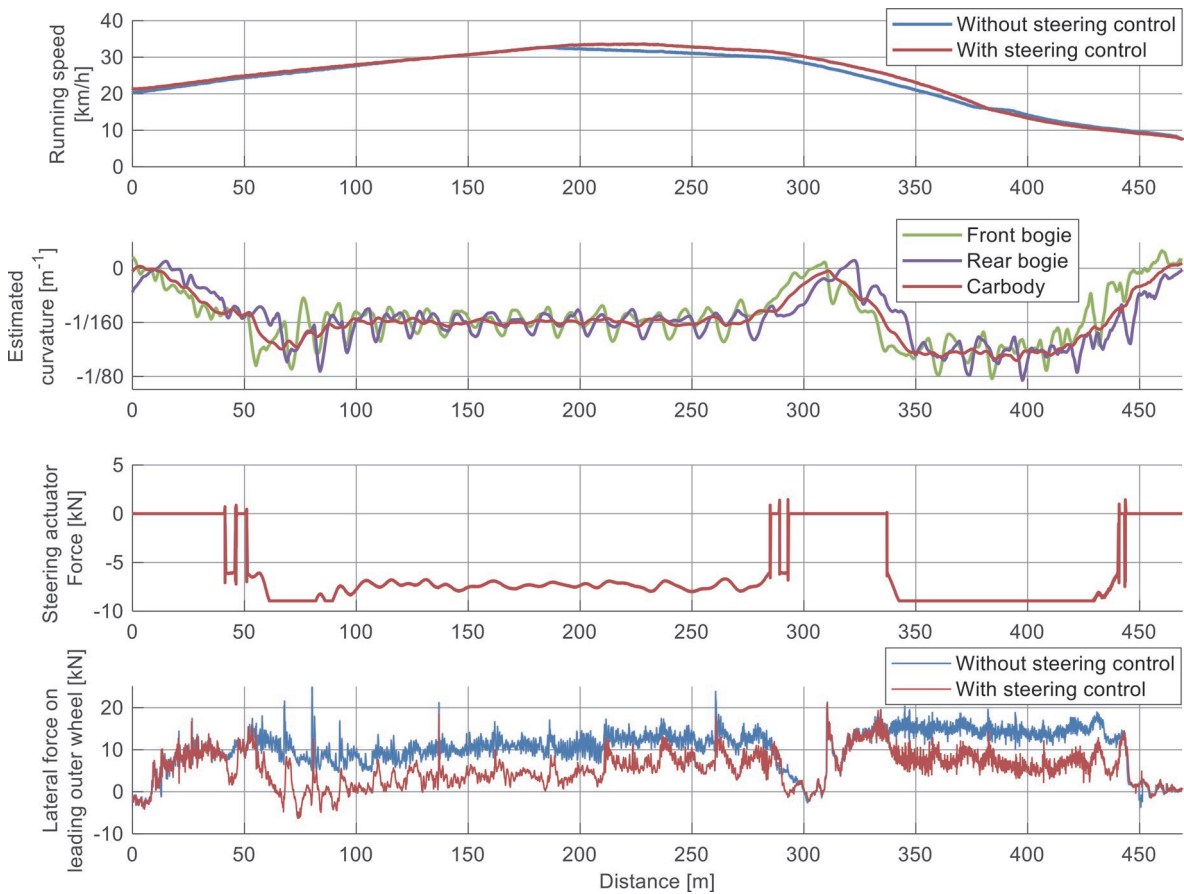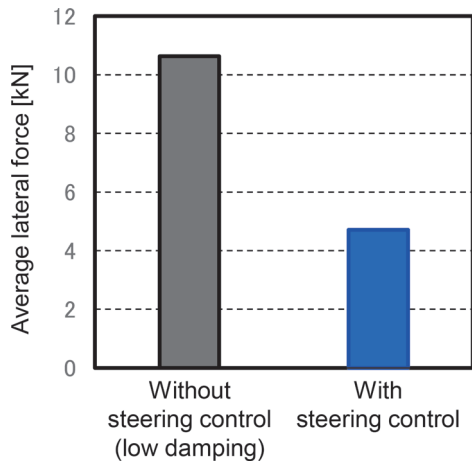
Fig. 9   Running test results

Fig. 10   Average lateral force on leading outer wheel in circular curve with a radius of curvature of 160 m

While increasing the rotation speed of the rollers in stages, all rollers translated in sine waves in the lateral direction (amplitude: ±3 mm, frequency: 1 Hz, wavelength: 3 cycles, phase difference between front and rear axle: 180°). We defined the running speed when hunting occurs after the roller translation as the hunting limit speed.

6.2   Test results

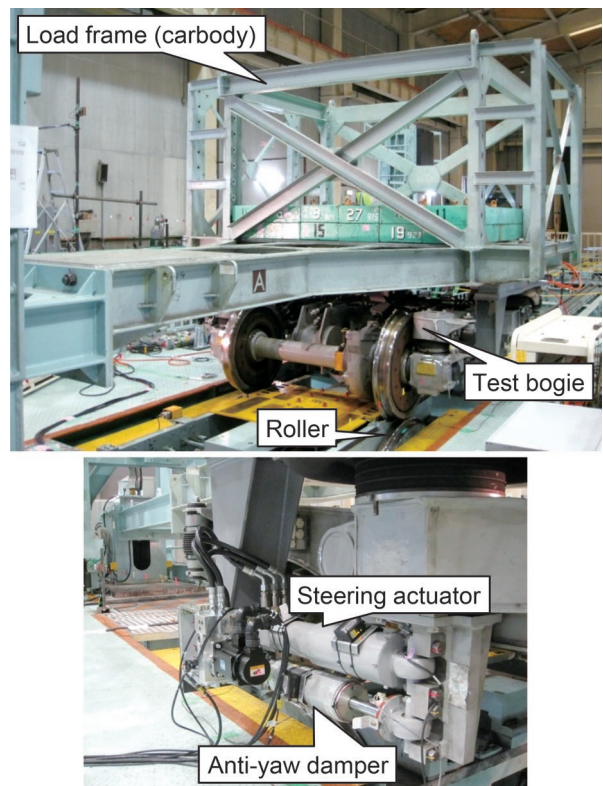In the test, the hunting limit speed with the steering actuators

Fig. 11   Roller rig test for running stability evaluation

was divided by that with the switchable anti-yaw dampers. The obtained value provides a normalized hunting limit speed. The normalized hunting limit speed was 1.02 in the low damping mode and 1.03 in the high damping mode. This result indicates that the prototype active bogie steering system does not affect the vehicle running stability.

7. Conclusions

We proposed and prototyped an active bogie steering system. The developed system consists of steering actuators, gyroscopes, a steering controller, and bogie angle detection mechanisms.

The test vehicle with the prototype steering system ran on the test line in the Railway Technical Research Institute. As a result of the test, it was found that the steering control reduces the average lateral force generated on the leading outer wheel on the circular curves. To be specific, the reduction was about 60% at a radius of curvature of 160 m compared to without control.

A hunting of the bogie was evaluated on a roller rig. The hunting limit speed with steering actuators was compared with that with switchable anti-yaw dampers. The test result shows that the prototype active bogie steering system does not affect the vehicle running stability.

References

[1] Sato, E., Kobayashi, H., Tezuka, K., Okamoto, I., Kakinuma, H. and Tamaoki, T., "Lateral Force during Curve Negotiation of Forced Steering Bogies," *QR of RTRI*, Vol. 44, No. 1, pp. 8-14, 2003.

[2] Togami, Y., Goto, R., Ogino, T., Shikata, K., Toide, T., Mizuno, M. and Shimokawa, Y., "Development of the New Concept Steering Bogie," *Journal of Mechanical Systems for Transportation and Logistics*, Vol. 6, No. 2, pp. 124-132, 2013.

[3] Matsumoto, A., Sato, Y., Ohno, H., Mizuma, T., Suda, Y., Michitsuji, M., Tanimoto, Y., Miyauchi, E. and Sato, Y., "Research on high curving performance trucks: concept and basic characteristics of active-bogie-steering-truck," *Vehicle System Dynamics Supplement*, No. 41, pp. 33-42, 2004.

[4] Tajima, S., "Opening of Tohoku Shinkansen Extension to Shin Aomori and Development of New Faster Carriages – Overview of Series E5/E6," *Japan Railway & Transport Review*, No. 57, pp. 6-11, 2011.

[5] Kamoshita, S., Umehara, Y., Yamanaga, Y., Suzuki, M., Hondo, T., "Total Performance Evaluation of the Assist Steering System for Bolsterless Bogie," *Quarterly Report of RTRI*, Vol. 59, No. 4, pp. 243-248, 2018.

Authors

Takashi KOJIMA, Dr. Eng.
Assistant Senior Researcher, Vehicle Dynamics Laboratory, Vehicle Technology Division
Research Areas: Running Gear Structure, Signal Processing

Yasuhiro UMEHARA, Dr. Eng.
Senior Researcher, Vehicle Dynamics Laboratory, Vehicle Technology Division
Research Areas: Vehicle Dynamics, Running Gear Structure

Takatoshi HONDO, Dr. Eng.
Assistant Senior Researcher, Vehicle Mechanics Laboratory, Railway Dynamics Division
Research Areas: Vehicle Running Safety, Measurement Technology, Signal Processing

Development of Train Operation Power Simulator Reproducing Commercial Operation

Tomoyuki OGAWA
Hydrogen and Sustainable Energy Laboratory, Vehicle Technology Division

Yoko TAKEUCHI
Transport Operation Systems Laboratory, Signalling and Operation Systems Technology Division

Hiroaki MORIMOTO
Power Supply Systems Laboratory, Power Supply Technology Division

Tatsuhito SAITO
Hydrogen and Sustainable Energy Laboratory, Vehicle Technology Division

Masahisa KAGEYAMA
West Japan Railway Company (Former)

In recent years, railway companies have been introducing energy-saving technologies. This is leading to a growing need for methods able to accurately estimate the energy-saving effect of individual technologies. To this end, RTRI and JR West have been developing a method to estimate energy consumption during train operation using the Train Operation Power Simulator which reproduces commercial operating conditions. Because of the dispersion of energy consumption in commercial operations, it is important to be able to faithfully reproduce commercial operations. Therefore, we have developed a method to reproduce commercial operation utilizing commercial running data obtained from a Train Data Collection Device. Moreover, we have achieved a practical calculation time to estimate the energy-saving effect.

Key words: *DC feeding, energy consumption, Train Data Collection Device, drivability/maneuverability, vehicle auxiliary power, running resistance*

1. Introduction

Reducing energy consumption is currently a topical issue in research, in many areas including railway systems. Estimating the energy-saving effect of applications in energy-saving strategies implemented on actual railway lines requires an accurate large-scale simulator.

Therefore, RTRI and JR West have been developing the Train Operation Power Simulator. This simulator is capable of calculating overall train operating energy used on DC railway lines by virtue of working closely with corresponding technical fields, namely electric power, vehicles, and train operations, and aims to predict the effects of energy-saving technologies. The development was divided into two stages: the development of a physical calculation algorithm and the development of a method for reproducing commercial operating conditions. In the first stage, simultaneous measurement tests of ground facilities and vehicles in the limited feeding section ware conducted to verify the physical calculation algorithm of the simulator [1]. In the second stage, power measurement tests were conducted on ground facilities during commercial line operation while using a train data collection device (TDCD) to verify the commercial operation reproduction method. This paper describes the second stage, i.e., the reproduction of commercial operations.

Regarding the reproduction of commercial operations, we classified railway lines into commuter and suburban lines and proceeded with the development of the calculation method in the stages. The Gakkentoshi Line of JR West, used as a target commuter line in this research, has little variety in the types of rolling stock series in use, track layout, etc., and is thus simple enough for basic calculation simulation and 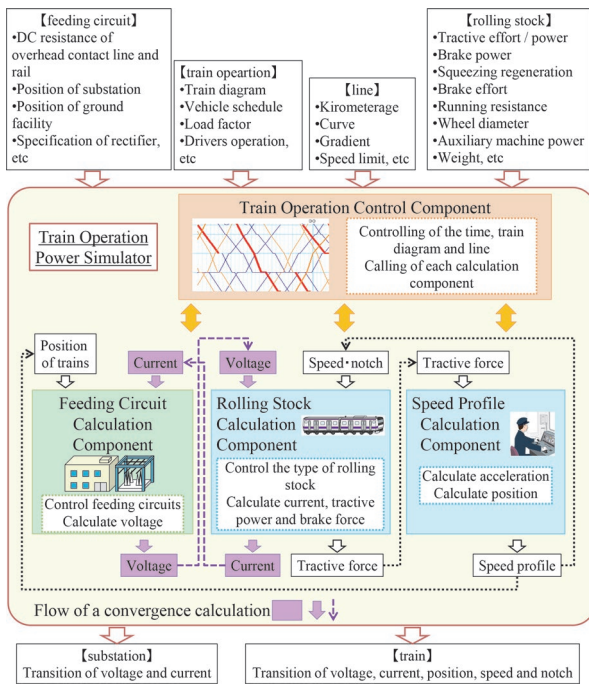result analysis. The Maibara - Kyoto section of the JR West Tokaido Line, used as a target suburban line, contains many points to be verified to make the simulator more general (e.g., diversity of rolling stock series, relatively long station-to-station distance, frequent operation of freight trains, and the existence of quadruple-track sections).

This paper shows the calculation method for reproducing commercial operations and verification results for the commuter and suburban lines.

2. Calculation method for reproducing commercial operations

2.1 Configuration of the Train Operation Power Simulator

Figure 1 shows the configuration of the Train Operation Power Simulator, which consists of the Train Operation Control Component, the Feeding Circuit Calculation Component, the Rolling Stock Calculation Component, and the Speed Profile Calculation Component. The Train Operation Control Component simulates the train operation control of all trains and progresses the simulation clock. The Feeding Circuit Calculation Component calculates the current and the voltage that will have an appropriate electrical relationship according to the train position on the line. The Rolling Stock Calculation Component calculates the current and the tractive force according to the voltage, the velocity, and the notch. The Speed Profile Calculation Component calculates the speed profile according to the temporal tractive force. That is, in each calculation step, the calculation proceeds while exchanging information between the Feeding Circuit Calculation Component, the Rolling Stock Calculation Component, and the Speed Profile Calculation Component.

Fig. 1 Configuration of the Train Operation Power Simulator [3]

Fig. 2 Outline of the algorithm for the creation of a speed profile for energy estimation [3]

Fig. 3 Concept of the re-search that takes place during a voltage drop in creation of speed profile for energy estimation [3]

Fig. 4 Train Data Collection Device [3]

To reproduce commercial operations, a creation algorithm of speed profile for energy estimation that creates speed profiles according to the specified running time was developed in the Speed Profile Calculation Component. In addition, parameter identification methods from using a Train Data Collection Device (TDCD) were established for brake notch, running resistance, auxiliary load, and passenger load factor, etc.
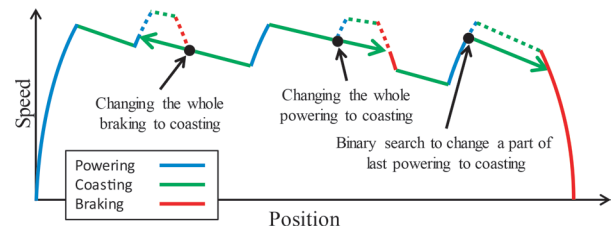
2.2 Speed profile creation algorithm

Energy consumption varies greatly depending on the driving operation. Thus, the creation algorithm of speed profile for energy estimation [2] (Fig. 2) was incorporated into the Train Operation Power Simulator, aiming to create a speed profile where the running time is specified and energy consumption becomes at the average level. When applying the creation algorithm of speed profile for energy estimation to the Train Operation Power Simulator, we should consider acceleration changes caused by the voltage fluctuation. Thus, in the simulation clock progresses, when a difference between specified and calculated running time exceeds a certain amount, the algorithm starts re-search for creation of speed profile for energy estimation from the current position (Fig. 3).
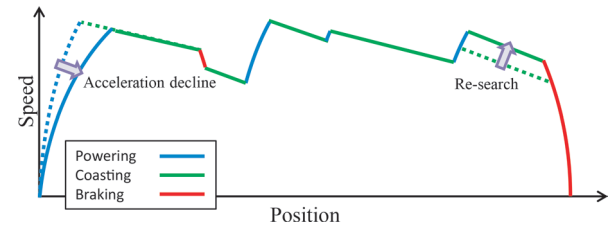
2.3 Train Data Collection Device (TDCD)

For constructing the rolling stock model, the information from the TDCD [4] was used. TDCD can receive various types of information via the communication line (Fig. 4). The device records the speed, the notch, the pantograph voltage, the traction circuit current, and auxiliary current data acquired from the digital data transmission system on a vehicle-by-vehicle and unit-by-unit basis.
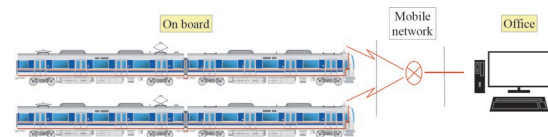
2.4 Brake notch model

We patterned the brake operation data on the commercial trains

of the target lines from TDCD. To extract typical brake operations, brake notch averages for each station-to-station section were calculated in 30 km/h steps. The average brake notch is therefore the time-averaged brake notch for every 30 km/h speed range in a section. No distinction was made between stop brakes for stopping at stations and deceleration braking because of speed limits. The pattern of brake operations is called a "brake pattern". Brake patterns are expressed as, for example, "5→4→3", which means that the time-averaged brake notch in the speed range over 60 km/h was B5N, B4N in the 60 to 30 km/h speed range, and B3N in the speed range below 30 km/h. B5N means "Brake 5 Notch" and the number corresponds to the braking force. Figure 5 shows and example of the brake pattern distribution for the Gakkentoshi Line. The 20 most frequent patterns accounted for 60% of all brake operations. Therefore, to reproduce the variation in brake operation, these top 20 patterns were applied randomly, according their appearance rate, to each train in station-to-station sections.

Figure 6 illustrates this concept of how brake patterns were applied. Deceleration varies depending on the brake pattern; thus, if the brake patterns are applied, there will be differences in running time. Therefore, the algorithm for the creation of speed profiles for energy estimation was used after applying each brake pattern in order to adjust operations according to the planned running time.

2.5 Running resistance model

The loss caused by running resistance accounts for most of the energy consumption [4]; thus, to calculate energy consumption, it is desirable to use a running resistance formula which can produce results as close to reality as possible. We therefore used the running resistance formula obtained in running resistance measurement tests (Fig. 7).
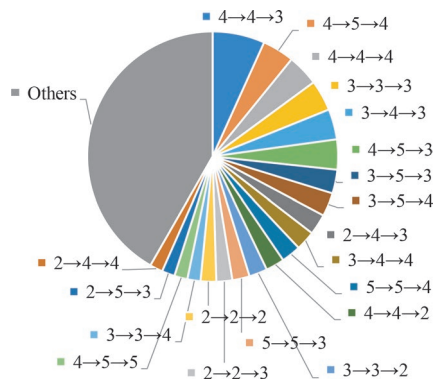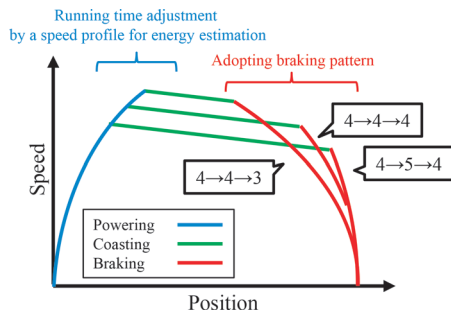
Fig. 5   Brake pattern appearance rate [3]

Fig. 6   Concept of how to apply brake patterns [3]
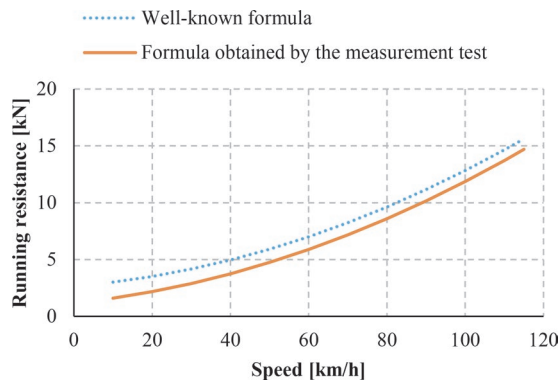

Fig. 7   Example of running resistance model [3]

2.6 Auxiliary load model

The auxiliary load of rolling stock fluctuates greatly depending on ambient temperature. Therefore, the auxiliary load model for the ambient temperature was calculated from the data in the TDCD (Fig. 8). Auxiliary power was set according to the ambient tempera-
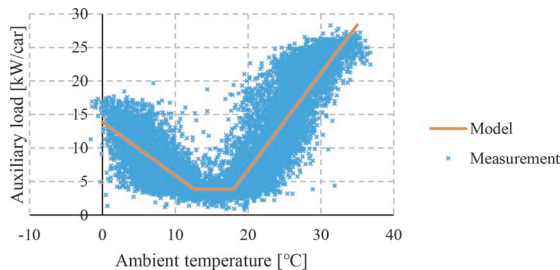

Fig. 8   Auxiliary load model [3]

ture, and the sum of the traction circuit power and the auxiliary power was used in the rolling stock power calculation.

2.7 Passenger load factor model

If the passenger load factor is different, the rolling stock mass changes, which affects the train acceleration in the speed profile calculation and the rolling stock power by load compensating control. Therefore, the model of passenger load factors for each time zone and each station-to-station section was calculated from the data in the TDCD. The medians of passenger load factors were calculated for each time zone and each station-to-station section from the data in the TDCD, and these values were set to use for the speed profile calculation and the rolling stock power calculation. When there were not enough data to calculate medians of passenger load factors because of little data from the TDCD, the passenger load factor for each station-to-station section was estimated using automatic ticket gate data.

3. Verification of method for reproducing commercial operations on a commuter line

The commercial operation reproduction method was verified on the Gakkentoshi Line of JR West, which is a commuter line.

3.1 Verification targets

Table 1 outlines the calculation conditions. Simultaneous power measurement of the substations and the rolling stock observes cases of regenerative power interchange even for rolling stock approx. 15 km away. Since the feeding circuit was connected to another line section, the calculation range was set wider than the verification range described later. Then, not only the Gakkentoshi Line but also the adjacent lines (JR Tozai Line and the Osaka Higashi Line) were targeted for accurate estimation. Figure 9 shows a part of the Gakkentoshi Line timetable used in the analysis.

Since the daytime timetable consists of pattern diagrams for every 30 minutes, the energy consumption is expected to be almost the same for each pattern. Therefore, the measured data was divided every 30 minutes, and six pieces of data were obtained per day during daytime zone of the 11:30 to 14:30. The evaluation comparison was made based on these pieces of data. As a result, a large number of samples were available for verification of daytime operations.

3.2 Substation measurement

Simultaneous power measurement of multiple substations in commercial operation was conducted from October 2015 to Febru-

Table 1   Calculation conditions for the commuter lines [3]

Lines	Gakkentoshi Line (Kizu – Kyoboshi)
	JR Tozai Line (Kyobashi – Amagasaki) Osaka Higashi Line (Hanaten – Kyohoji)
Substations	13 posts, including sectioning posts
Timetable	Weekday daytime and weekday whole day
Passenger load factor	Set for each train and each station-to-station section
Calculation scale	Train kilometer:2,130 km or 16,365 km

ary 2016 and from July 2016 to May 2017. Measuring instruments were temporarily installed on the Shimokoma, Tanabe, Tsuda, Shijonawate, and Hanaten substations on the Gakkentoshi Line, to measure the feeder line currents, the DC bus voltages, etc.

Figure 10 outlines the feeding circuit of the Gakkentoshi Line. The Kizu - Matsuiyamate section is a single-track section. The section between Matsuiyamate and Shijonawate is a double-tracked but the feeders on the up and down lines are permanently connected in parallel. The rest of the section is purely double-track and a paralleling switchgear post is installed at Suminodo station. Therefore, in these sections, the regenerative power may be directly interchanged between the up and down lines without going through the DC bus of the substation. Therefore, for the section from the Tanabe Substation (SS) to the Hanaten SS, the current measured at the substations cannot be separated between the up and down lines; thus, the total load of the up and down lines was subjected to the verification.

3.3 Analysis method

Figure 11 shows the method that was to analyze power in the substations. Power in individual feeder lines was acquired by measuring the feeder line current and DC bus voltage. Synchronized sampling technique by GPS enabled substation line power calculation between adjacent substations. The feeding section power was
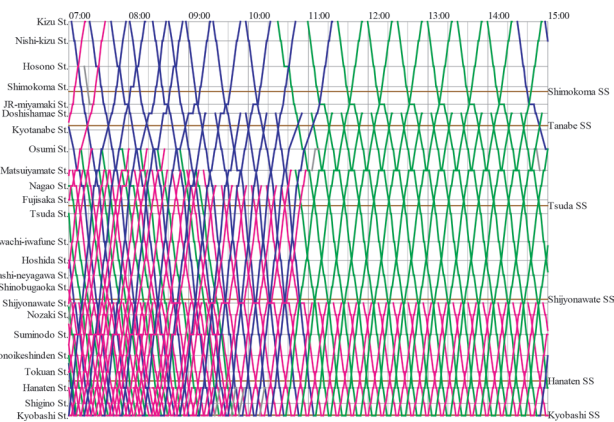

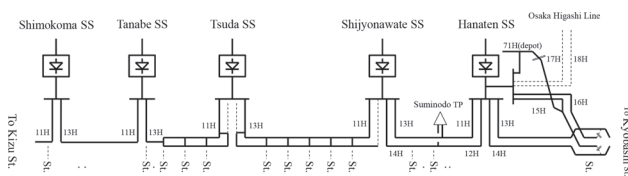**Fig. 9   Part of the commuter line timetable to analyze [3]**

Fig. 10   Outline of measurement feeding circuit of the commuter line [3]

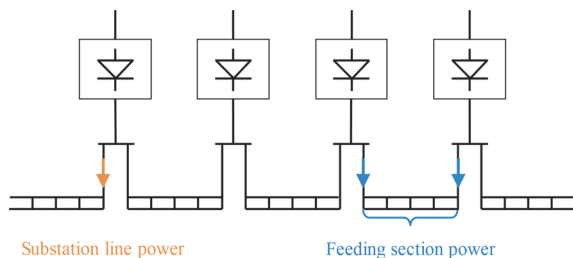Substation line power   Feeding section power

Fig. 11   Method of analysis by substation synchronous measurement [3]

obtained from the sum of the substation line power supplied to that feeding section. The feeding section energy consumption which is obtained by integrating the feeding section power over time is a useful index for estimating the energy consumption of rolling stock because it is the energy consumption of the train running in the relevant feeding section.

3.4 Comparison with the measurement results

Figure 12 compares calculated and measured results for feeding section energy consumption. The points on the graph represent energy consumption every 30 minutes during the 11:30 to 14:30 period, which corresponds to the pattern diagram, in relation to ambient temperature. As an example of issues in the conventional calculation method, braking operations and running resistance did not match the actual situation. Therefore, to compare the conventional calculation method and the proposed method, the Fig. 12 (b) shows the calculation results of a reproduction of the conventional method; (i) the brake operation was set to B5N, used for normative driving, and (ii) the running resistance of all rolling stock was increased by 20%. This figure also shows the measurement results averaged in the ±2.5°C range after divided per 5°C interval in the ambient temperature. As for the average value of the measurement results, at the ambient temperature upper limit (35°C), the measured value used for calculating the average was biased toward the lower limit, and at
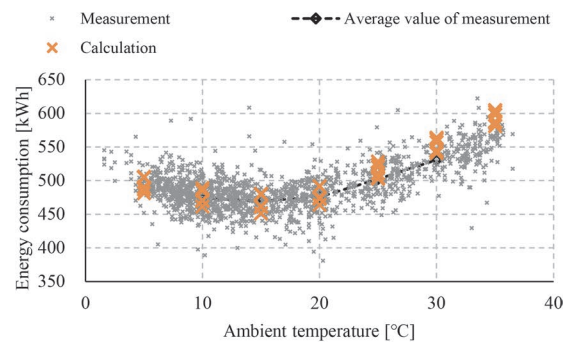
(a)   Proposed method
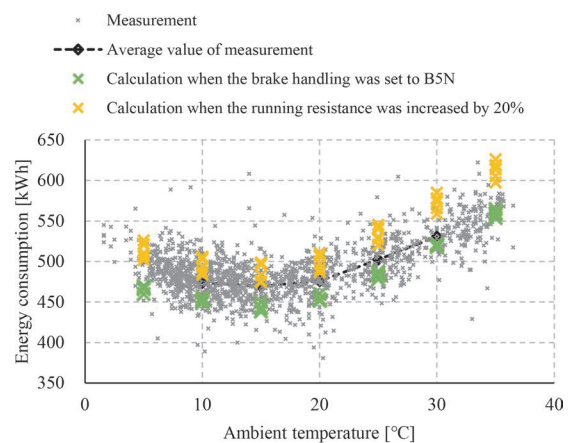
(b)   Reproduction of conventional method

Fig. 12   Verification based on the energy consumption in the commuter line feeding section
(Feeding circuit energy consumption of the Tsuda SS - Shijonawate SS section)

the lower limit (5°C), which is the one used for calculating the average was biased toward the upper limit. Therefore, the graph excludes these biases and only shows data for the 10 to 30°C range.

Plotting ambient temperature on the horizontal axis, reveals that the energy consumption fluctuates depending on ambient temperature. The measurement results vary even at the same ambient temperature. The main factors of these variation are that the passenger load factor varied even in the same pattern diagram, that two rolling stock series ran, and that there were variations in driving operation. In this calculation, the passenger load factor was set from the TDCD data depending on the train and the station-to-station section, the vehicle roster was set randomly according to the rate of the number of rolling stock series, and driving behavior was reproduced by randomizing brake operation, as explained in section 2.4. Out of these, by making the brake operation random, the calculation results varied near the measurement results compared to the case where the brake operation was set uniformly at B5N. From this fact, it is considered that the difference in brake operation is the primary factor in variation. Therefore, variation in the measurement results were reflected by randomizing the brake operation.

The calculation results of the proposed method were close to the average value of the measurement results; for example, at an ambient temperature of 15°C, the calculation results ranged from -4.0% to +2.2% (average -0.2%) compared to the average value of the measurement results (Fig. 12 (a)). Compared with the conventional calculation method, when the brake operation was set uniformly to B5N, the calculation results tended to be smaller than the measured results. For example, at an ambient temperature of 15°C, the calculation results ranged from -6.7% to +4.1% (average -5.6%) compared to the average value of the measured results (Fig. 12 (b)). When the running resistance was increased by 20%, the calculated results tended to be larger than the measured results. For example, at an ambient temperature of 15°C, the calculated results ranged from +1.0% to +6.2% (average +3.8%) compared to the average value of the measured results (Fig. 12 (b)). From the above, although the differences varied depending on the ambient temperature, the proposed method can reproduce the tendency of measured results, and it is therefore considered that the calculations were generally good.

4. Verification of method for reproducing commercial operations on a suburban lines

The commercial operation reproduction method was verified on the Tokaido Line of JR West, which is a suburban line.

4.1 Verification targets

Table 2 outlines the calculation conditions. In the study of the Gakkentoshi Line mentioned in the previous chapter, the daytime timetable, which was a pattern diagram, was analyzed. However, on the Tokaido Line, energy consumption did not repeat at regular in-

Table 2   Calculation conditions for the suburban line [3]

Lines	Tokaido Line (Maibara – Kyoto) Kusatsu Line (Tsuge – Kusatsu)
Substations	15 posts, including sectioning posts
Timetable	Weekday whole day
Passenger load factor	Set for each train and each station-to-station section
Calculation scale	Train kilometer: 23,865 km

tervals even during the daytime, because the number of cars in passenger train trains varies, and there was operation of freight trains not patterned. Therefore, verification was conducted over a single day's operation from first to last train. The ranges used in the calculations were the Maibara - Kyoto section of the Tokaido Line and the Kusatsu Line. The model of the feeding circuit was simplified to a minimum.

In addition, in the target line section, type of rolling stock and number of cars in each train-set varied greatly. It was difficult to prepare a model for every type of rolling stock. Therefore, the car-kilometer value was calculated in advance for each rolling stock series and the numbers of cars in train-sets from the timetable and the vehicle roster. Figure 13 summarizes the car kilometer calculation results by rolling stock series. In consideration of the rolling stock series and the number of cars in each train-set, 12 types of passenger rolling stock model were used.

4.2 Substation measurement

Simultaneous power measurement of multiple substations used in commercial operations was conducted from October 2017 to February 2019. Measuring instruments were temporarily installed at the Kawase, Notogawa, Shinohara, Moriyama, and Seta SSs and Yasu and Kusatsu sectioning posts on the Tokaido Line, the feeder line currents, the DC bus voltages, and others were measured. Figure 14 outlines the feeding circuit on the Tokaido Line which was measured. The Maibara - Kusatsu section is a double-track section, and the Kusatsu - Kyoto section a quadruple-track section.

4.3 Estimating running resistance

In general, trains on suburban lines run at higher speeds than on commuter lines. Running at a higher speed increases the ratio of running resistance to tractive force and increases the effect on the calculation accuracy of running resistance. However, it was impractical to measure the running resistance of all types of rolling stock running on the target line section. Therefore, the running resistance was measured for the main rolling stock series from the car kilometer calculation results.

The target rolling stock series operates in sets of four or more cars. Then, the running resistance was measured for different consists and we estimated the running resistance estimation equation
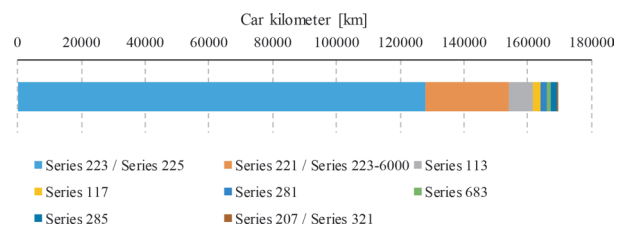
Fig. 13   Car kilometers by rolling stock series [3]
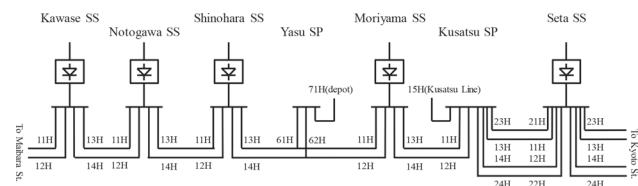
Fig. 14   Outline of measurement feeding circuit of the suburban line [3]

including the consist type as a variable. Figure 15 shows the running resistance characteristics used in the calculation.

4.4 Comparison with the measurement results

Figure 16 compares calculated and measured results of feeding section energy consumption. The calculation results were obtained by calculating the energy consumption every 60 minutes with the condition of an ambient temperature of 15°C in every time zone. The measurement results show the measured values corresponding to the 15±2°C range.

There is a wide range of measurement results depending on the measurement date. Possible factors of such variability are, for example, (i) differences in driving operation among drivers, (ii) different rolling stock series that are assigned daily because of common operation among multiple rolling stock series, (iii) fluctuations in passenger load factor of passenger trains and hauling mass of freight trains. For this reason, a calculation method that can reflect variations was used. Quantitative comparison with average values is for reference only, during the daytime zone from 10:30 to 17:30, which included a lot of data falling within the ambient temperature range of 15±2°C, the calculation results ranged from -3.8% to + 12.6% (average +5.3%) compared to the average value of the measurement results. In addition, qualitatively, the calculation results changed while generally responding to the changes in measurement results over time, which is considered to be good calculation result.

5. Comparison of calculation scale and calculation time

Figure 17 shows a comparison in the calculation scale and calculation time in single thread (computer: CPU Intel Core i9-9900 3.10 GHz, RAM 16.0 GB). The calculation time was a little over a day even with a train kilometer value of over 20,000 km. It is a
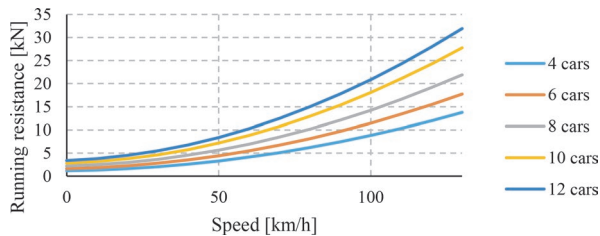

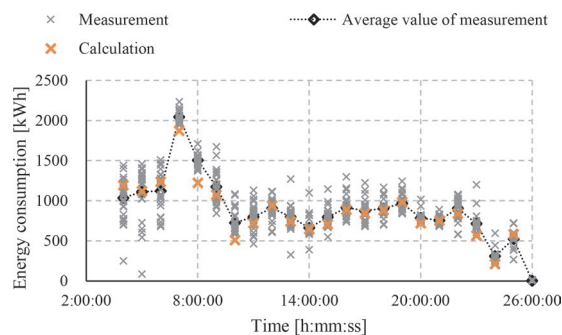**Fig. 15 Estimated running resistance characteristics [3]**

Fig. 16 Verification by feeding section energy consumption of the suburban lines
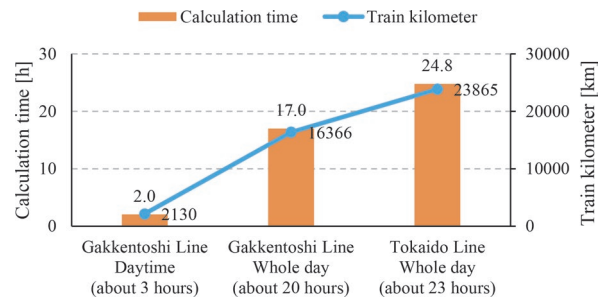**(Feeding circuit energy consumption of the Notogawa SS - Shinohara SS section downline)**

Fig. 17 Comparison of calculation scale and calculation time

practical calculation time for predicting the effects of energy-saving technology.

In the estimation of energy-saving technology, in general, we have to compare conditions before and after the introduction of that technology into practice. As for the conditions after the introduction, comparisons are often made through a multiple-specification study. This simulator has a single core processor. A comparison in multiple conditions can be made in almost the same calculation time as in single conditions using parallel processing by the multi-core following the startup of multiple processes in the same computer.

6. Conclusion

This paper presented the reproduction of commercial operations in the Train Operation Power Simulator. The issue with commercial operations is that energy consumption varies even within the same timetable. By reproducing commercial operating conditions, we have developed a method that can reproduce variation in train operation and obtained a calculated energy consumption which is close to measured data; for example, the calculation results ranged from -4.0% to +2.2% (average -0.2%) compared to the average value of the measurement results on a commuter line, and the calculation results ranged from -3.8% to + 12.6% (average +5.3%) compared to the average value of the measurement results on a suburban lines. In addition, predicting the effects of energy-saving technologies can be achieved within a practical calculation time; for example, the calculation time was a little over a day even with a train kilometer value of over 20,000 km.

In the future, we will utilize the Train Operation Power Simulator to accurately predict the effects of various energy-saving technologies and search for efficient ways to put this method into practice.

References

[1] Yoko TAKEUCHI, Tomoyuki OGAWA, Hiroaki MORIMOTO, Yoichi IMAMURA, Shingo MINOBE, and Shoichi SUGIMO-TO, "Development of a Train Operation Power Simulator Using the Interaction between the Power Supply Network, Rolling Stock Characteristics and Driving Patterns, as Conditions,"

Quarterly Report of RTRI, Vol. 58, No. 2, pp. 98-104, 2017.

[2] Tomoyuki Ogawa, Yoko Takeuchi, Hiroaki Morimoto, Yoichi Imamura, and Masahisa Kageyama, "Energy Simulation by use of a Speed Profile Generator for an Energy Estimation," *RTRI Report*, Vol. 30, No. 11, pp. 29-34, 2016 (in Japanese).

[3] Tomoyuki Ogawa, Yoko Takeuchi, Hiroaki Morimoto, Masahisa Kageyama, and Shingo Minobe, "Estimation Method of Energy Consumption Using Train Operation Power Simulator,"

IEEJ Transactions on Industry Applications, Vol. 141, No. 5, pp. 374–387, 2021 (in Japanese).

[4] Tomoyuki OGAWA, Shinichi MANABE, Gaku YOSHIKAWA, Yoichi IMAMURA, and Masahisa KAGEYAMA, "Method of Calculating Running Resistance by the Use of the Train Data Collection Device," *Quarterly Report of RTRI*, Vol. 58, No. 1, pp. 21-27, 2016.

Authors

Tomoyuki OGAWA, Dr. Eng.
Senior Researcher, Hydrogen and Sustainable Energy Laboratory, Vehicle Technology Division
Research Areas: Energy Simulation, Analysis of Train Information

Yoko TAKEUCHI
Senior Chief Researcher, Head of Transport Operation Systems Laboratory, Signalling and Operation Systems Technology Division
Research Areas: Train Operation Simulation, Energy Simulation and Control, Mathematical Optimization

Hiroaki MORIMOTO
Senior Chief Researcher, Head of Power Supply Systems Laboratory, Power Supply Technology Division
Research Areas: Traction Power Supply Systems

Tatsuhito SAITO, Dr. Eng.
Researcher, Hydrogen and Sustainable Energy Laboratory, Vehicle Technology Division
Research Areas: Traction Motor Drive, Energy Storage System, Regenerative Brake Control

Masahisa KAGEYAMA
Deputy General Manager of Technical Research & Development Dept. Railway Operations Headquarters, West Japan Railway Company (Former)
Research Areas: Vehicle Technology

Design Method for GRS Integral Bridge with the Use of PCT Girder

Shuntaro TODOROKI
Concrete Structures Laboratory, Structures Technology Division

Masaru OKAMOTO
Concrete Structures Laboratory, Structures Technology Division (Former)

Hidetoshi NISIOKA
Foundation & Geotechnical Engineering Laboratory, Structures Technology Division (Former)

Shinichi TAMAI   **Toyoji YONEZAWA**   **Hidekazu ISHII**
Japan Railway Construction, Transport and Technology Agency

Geosynthetic-Reinforced Soil (GRS) integral bridge is a bridge that rigidly joins a girder and a reinforced soil abutment. This paper describes an outline of our new joint structure connecting a prestressed concrete T-shaped (PCT) girder and an abutment, which has been an important issue in developing GRS integral bridges using PCT girders. In addition to a design method for this joint structure of a PCT girder and an abutment, unique points of a design method for GRS integral bridge with use of PCT girders are introduced.

Key words: *GRS integral bridge, PCT girder, joint structure, design method*
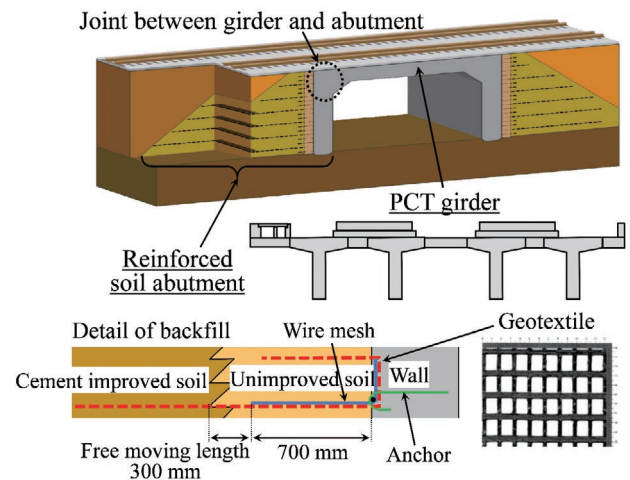
1. Introduction

Geosynthetic-Reinforced Soil (GRS) integrated bridges have already been designed and constructed on the Hokkaido Shinkansen [1] and the Sanriku Railway [2] in Japan. Figure 1 shows GRS integral bridge. A wall and backfill reinforced with geotextile are connected with geotextile and it is called a reinforced soil abutment, moreover the girder and the abutment are rigidly joined.

GRS integral bridge has the following characteristics: 1) lower construction and maintenance cost because bearings are not used, 2) prevention of backfill subsidence through geotextile reinforcement, 3) greater economy by virtue of slimmer abutments, 4) high redundancy and excellent seismic resistance because of the reinforced soil, rigid frame with a PCT girder and an abutment resistant to seismic force.
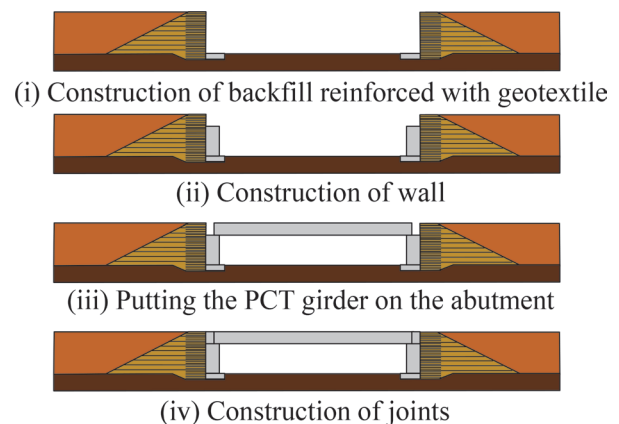
In the Hokkaido Shinkansen, the girder structure of the GRS integrated bridge uses Reinforced Concrete (RC), and it is a short-span bridge of 20m or less. In order to apply this bridge to a longer span, the girder structure had to use Prestressed Concrete (PC) as shown in Fig. 1.

Figure 2 shows the construction process of GRS integral bridge using a PCT girder. First, reinforced soil is constructed (i), after the subsidence of the reinforced soil by the deformation of the soil and the supporting ground have sufficiently converged, walls are constructed (ii). Secondly, a PCT girder manufactured in a yard on site is put on the abutments (iii). Finally, the joint between the PCT girder and the abutments, the space between the girders, and an overhanging slab are constructed (iv).

On the other hand, there is no design guideline and no application for bridges using a PC structure. This is because in contrast to RC girder structures, PC structures are applied for lengthening spans, and the response of the geotextile connecting a rigid frame and an abutment increases with repeated shrinkage, creep and temperature change of concrete, and changes in the response characteristics of the geotextile over time as a result of this, are still unclear. In addition, prestressed force also changes significantly. Therefore,

Fig. 1   GRS integral bridge using PCT girder

(i) Construction of backfill reinforced with geotextile

(ii) Construction of wall

(iii) Putting the PCT girder on the abutment

(iv) Construction of joints

Fig. 2   Construction process of bridge using PCT girder

it is difficult to evaluate the response of a bridge. Also, there has been no research on the joint structure between a PCT girder and reinforced soil abutments.

So far, the repetitive response characteristics of the geotextile [3], the response as a bridge [4,5,6,7], and the joint structure between a PCT girder and abutments [3] have been studied. On the basis of this research, a design method for GRS integral bridge using PCT girders has been proposed.

In this paper, among these studies, the proposed joint structure between a PCT girder and abutments is shown, and in addition to a design method for this joint structure of a PCT girder and abutments, a characteristic design method when using a PCT girder are introduced.

2. Joint structure between PCT girder and abutment

2.1 Outline of proposed joint structure

Figure 3 shows a proposed joint structure. For simply supported girders, the concrete of the flange is cast up to the end of a girder in advance, but a girder for GRS integral bridge is cast up to the joint. Then, the reinforcing bars of the flange are extended to the back surface of the abutment, concrete is cast at the joint, and the girder and abutment are integrated. In addition, reinforcing bars are placed on the web side surface of the girder in contact with the joint surface. In this joint structure, shearing force and torsional moment generated at the joint are transmitted by the friction and reinforcing bars of the joint surface.

2.2 Equation for torsion transmission strength of joint surface and its test

Equation (1) for the torsion transmission strength of a joint surface has been proposed for flat slabs [8,9]. Here, an experiment was carried out using a rectangular RC beam modeling a girder and a joint, and the applicability of this equation to this GRS integral bridge was examined by loading test. The applicability of shear transmission strength for design V_{cwd} has been examined in previous studies [10].

$$M_t = 1/2 \cdot c^2 \cdot (d - c/3) \cdot \tau_y / \gamma_{b1} \quad (1)$$

Where:

$\tau_y = V_{cwd} / A_c$
$V_{cwd} = (\tau_c + p \cdot \tau_s \cdot \sin^2 \theta - \alpha \cdot p \cdot f_{syd} \cdot \sin \theta \cdot \cos \theta) A_c / \gamma_{b2}$
$\tau_c = \mu \cdot f'^b_{cd} \cdot (\alpha \cdot p \cdot f_{syd} - \sigma_{nd})^{1-b}$
$\tau_s = 0.08 \cdot f_{syd} / \alpha$
$\alpha = 0.75 \cdot \{1 - 10 \cdot (p - 1.7 \cdot \sigma_{nd} / f_{sy})\} \quad 0.08\sqrt{3} \leq \alpha \leq 0.75$

- M_t : torsion transmission strength for design (N · mm)
- c : short side of joint surface (mm)
- d : long side of joint surface (mm)
- τ_y : shear transmission stress for design (N/mm²)
- V_{cwd} : shear transmission strength for design (N)
- A_c : cross-sectional area of joint surface (mm²)
- p : reinforcing bar ratio $p = A_s / A_c$
- A_s : cross-sectional area of reinforcing bars (mm²)
- θ : the angle between joint surface and the reinforcing bar
- f_{syd} : tensile yield strength of the reinforcing bar for design (N/mm²) $f_{syd} = f_{syk} / \gamma_s$
- f_{syk} : tensile yield strength of the reinforcing bar (N/mm²)
- γ_s : safety factor for steel material
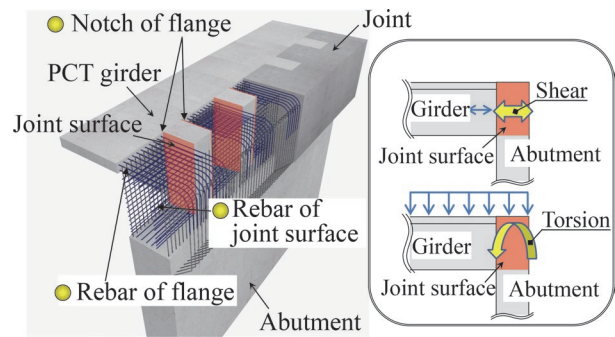- μ : average coefficient friction for solid contact, 0.45

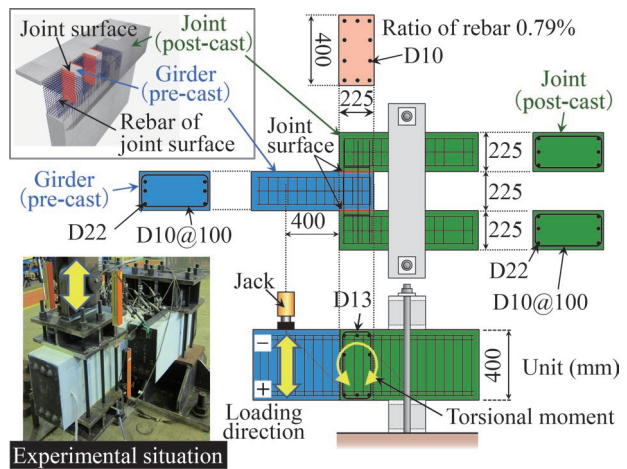**Fig. 3 Proposed joint structure between PCT girder and abutment**

Fig. 4 Test structure for torsion transmission of joint surface

Table 1 Material properties

Concrete		Rebar			Ratio of rebar in joint surface
f_c		Nominal diameter (Name)	f_{sy}	E_s	
Girder	Joint				
51.3	28.8	9.53 mm(D10)	380	181	0.79%
		12.7 mm(D13)	356	190	
		22.2 mm(D22)	450	182	

f_c: compression strength(N/mm²), f_{sy}: yield strength(N/mm²), E_s: Young's modulus(kN/mm²)

- b : coefficient considering the properties of joint surface. In here, 1/2 when the joint surface is roughened
- σ_{nd} : average stress generated perpendicular to the joint surface (N/mm²). When compressed, $\sigma_{nd} = -\sigma'_{nd}/2$
- σ'_{nd} : average compression stress generated perpendicular to the joint surface (N/mm²))
- f'_{cd} : compressive strength of concrete for design (N/mm²) $f'_{cd} = f'_{ck} / \gamma_c$
- f'_{ck} : compressive strength of concrete (N/mm²)
- γ_c : safety factor for concrete material
- γ_{b1} : safety factor for member in (1)
- γ_{b2} : safety factor for member in V_{cwd}

Figure 4 shows a test structure. Table 1 shows material specifications. The test structure consists of a girder and a joint with beams. First, one beam modeling a girder was manufactured, then,
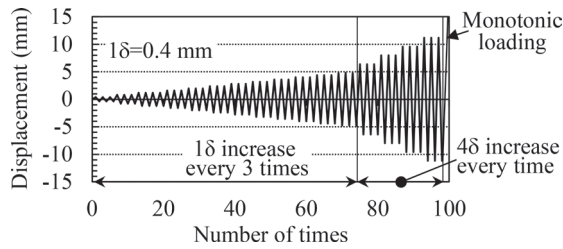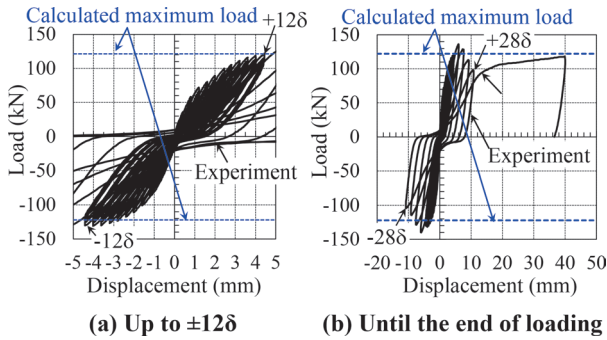
Fig. 5   Loading method

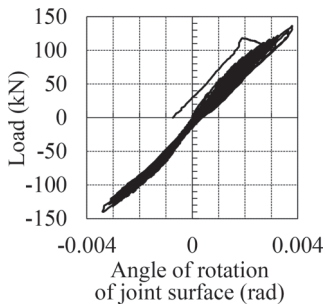**(a) Up to ±12δ**   **(b) Until the end of loading**

Fig. 6   Load-Displacement

Fig. 7   Angle of rotation of joint surface

Fig. 8   Joint surface at maximum load

Fig. 9   Comparison of experimental and calculated values

Fig. 10   Examination of safety factor
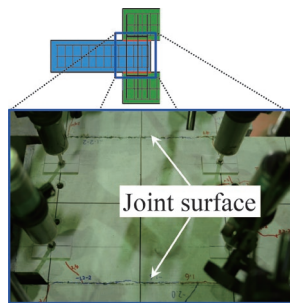
two beams modeling a joint were manufactured. The dimensions of the joint surface are 400 mm in height, 225 mm in width. The reinforcing bar ratio was 0.79%. The joint surface had irregularities of 2 to 3 mm following treating with a retarding agent. The reinforcing bars in the beams were arranged so that the bend strength and shear strength of the beam were greater than the torsion transmission strength of the joint surface. The torsion transmission strength was calculated by (1). γ_{b1} and γ_{b2} were set to 1.0.

Figure 5 shows loading cycles. "1δ" is the displacement of 0.4 mm at a load of 1/3 of the maximum load ("calculation" in Fig. 6) calculated by (1). Up to the maximum load calculated by (1), loading was repeated 3 times in ± 1δ increments, and thereafter, loading was repeated once in ± 4δ increments. After 28δ, the load was monotonically loaded on the positive side, and the test was completed. The loading direction is positive (+) on the lower side and negative (-) on the upper side as shown in Fig. 4.

Figure 6 shows a load-displacement relationship. The maximum load in the experiment is larger than the value calculated by (1). As shown in Fig. 7, the angle of rotation of the joint surface is as small as 0.004 rad or less at the maximum load. The joint surface did not shift even at the maximum load (Fig. 8).

Figure 9 shows a comparison between the experimental values including previous experimental results [9] and the calculated val-
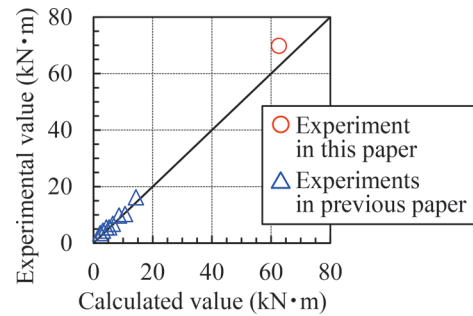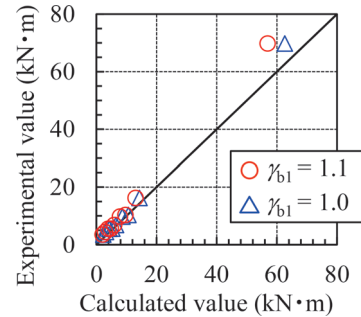
ues by (1). γ_{b1} and γ_{b2} were 1.0. The experimental / calculated values, including previous experimental results, had an average value of 1.18 and a coefficient of variation of 0.16. Therefore, it is considered that torsion transmission strength can be roughly calculated by (1).

Figure 10 shows a comparison between the calculated values and the experimental values, where γ_{b1} is 1.0 or 1.1. γ_{b2} was set to 1.0 because V_{cwd} evaluates experiment values on average [3]. When γ_{b1} is 1.1, the experimental value / calculated value is 1.06 to 1.71, and the experimental value is larger than the calculated value in all the results. Therefore, in calculating the design torsion transmission strength, γ_{b1} was set to 1.1.

2.3 Design method for earthquake and its test

From a seismic response analysis, it has been confirmed that GRS integral bridge exhibits linear response without damaging structural elements such as girders and abutments even with L2 seismic force used in the design [11]. However, in preparation for an earthquake larger than the scale used in the design, it is better to clarify in advance the order of damage for each structural element: the lower end of the haunch (Fig. 11) of an abutment part of a RC structure should be designed to be the first damaged in such a large earthquake for ease of repair. Therefore, the formation of plastic hinges and deformation performance on an abutment using the test structure modeling girders, an abutment, and joints was examined.

Figure 11, and Tables 2 and 3 show the outline of the test structure, the compressive strength of concrete, and the specifications of reinforcing bars. The test structure is a 1/3 scale model of real girders, an abutment, and joints. Reinforcing bars in the joints and the abutment were arranged so that the ratio of the reinforcing bars was the same as the actual size. The number of reinforcing bars on the joint surface was set so that the lower end of haunch part of the abutment was damaged at first. The joint surface of the abutment and the joint surface of the girder were treated with a retarding agent
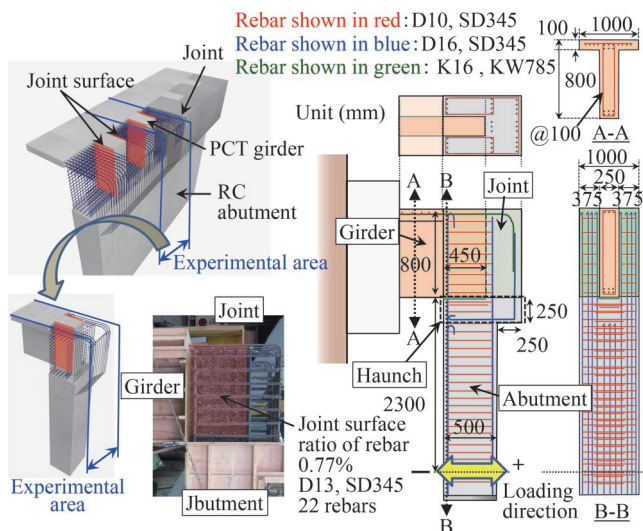
Fig. 11   Test structure for design method for earthquake

Table 2   Compression strength of concrete (N/mm²)

Abutment	Girder	Joint
34.2	55.1	35.3

Table 3   Material properties of rebar

Name		Nominal diameter	f_{sy}	E_s	ε_{sy}
D10	SD345	9.53 mm	365	179	2035
D13		12.7 mm	363	186	1955
D16		15.9 mm	375	174	2151
K16	KW785	15.9 mm	803	189	4239

f_{sy}: yield strength (N/mm²), E_s: Young's modulus (kN/mm²), ε_{sy}: yield strain (μ)
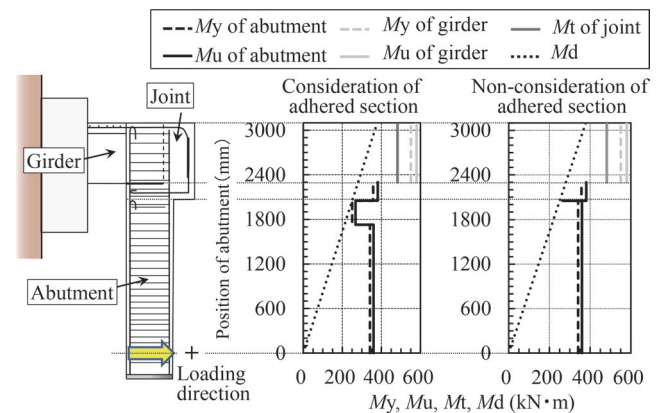

Fig. 12   Relationship between the strength of each member when loading on the positive side

to have irregularities of 2 to 3 mm.

The loading method was a positive/negative cyclic loading with 3 repetitions. A reference displacement "1δ" is the displacement that an axial reinforcing bar is yielded at the time of loading on the positive side.

Figure 12 shows the relationship between the strength of each member. This figure shows the case of positive loading. The strength in "Consideration of the adhered section" is calculated assuming that there is no adhesion along a length of 320 mm of the reinforcing bar fixed at the lower end of haunch, corresponding to 20 times the diameter of the reinforcing bar, whereas strength with "No consideration of the adhered section" is calculated assuming there is adhesion between the concrete and the reinforcing bar along this 320 mm section.

M_y and M_u are the bending yield strength and bending ultimate strength. Shear strength is greater than bending strength for both the girder and the abutment. M_t is the torsion transmission strength of the joint surface calculated by (1), and M_d is the bending moment.

The test structure was designed so that the lower end of the haunch of the abutment would be damaged before the girders and joints were damaged. Figure 12 indicates that M_y is smaller than M_d at the lower end of the haunch of the abutment. Since a girder will be erected on an abutment after being manufactured in a yard, axial reinforcing bars of an abutment cannot be placed at the erection point of a girder. Therefore, the numbers of axial reinforcing bars to be tensile in the abutment during positive and negative loading are 8 and 11 respectively, and bending yield strength and bending strength during positive and negative loading are different.

Figure 13 shows the load-displacement relationship. The displacement is measured at the loading position using a measurement beam fixed to the joint. Therefore, displacement occurs only by deformation of the abutment removing the deformation due to the deformation of the girder and the rotation of the joint. In addition, calculated values using a deformation performance calculation equation shown in the railway standards [11] are illustrated. The shear span used in the calculation was set to 2.3 m when loaded on the positive side and 2.05 m when loaded on the negative side due to the condition of the cracks.

In the positive loading, the load gradually increased from +1δ to the second time of +7δ. The tensile reinforcing bar broke at the third time of +7δ, and the load decreased. In the negative loading,
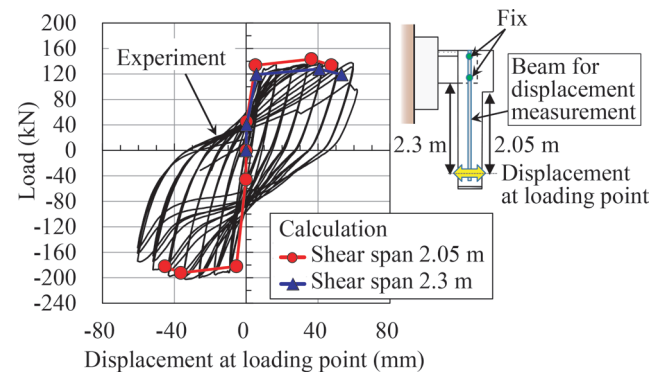

Fig. 13   Load-Displacement

spalling of the cover concrete and buckling of the reinforcing bar occurred at the lower end of the haunch of the abutment as shown in Fig. 14, and then the maximum load was reached at −4δ. After that, the load gradually decreased from −5δ to −7δ. As expected in the design, it was confirmed that the lower end of the haunch part of the abutment was damaged before the joint surface and the specified deformation performance could be secured.

Figure 15 shows the strain of the reinforcing bars on the joint surface. The maximum strain of the reinforcing bars on the joint surface was about 400 μ to 1,200 μ when loaded on the positive side, and the yield strain had not been reached. In addition, no deviation was confirmed visually at the joint surface. Therefore, it can be assumed that the junction is a rigid region in the response analysis.

3. Unique points of design method for GRS integral bridge with PCT girder

3.1 Calculation of response value

3.1.1 Modeling of bridge

In GRS integral bridge, reinforcing soil and a rigid frame with a PCT girder and abutments are integrated to resist the force during an earthquake and action other than during earthquake. Therefore, it is desirable to model each structural element as a unit, considering the interaction between reinforced soil and a rigid frame. However, by appropriately setting boundary conditions such as load conditions and constraint conditions and a member model, it is possible to separate and model each structural element.

Figure 16 shows the structural analysis model used for checking the failure of abutments, PCT girders, joints between abutments and girders, and geotextiles. A "buffer layer" spring is a model for the response characteristics of the section of geotextiles and unimproved soil of 700 mm and free lengths of 300 mm shown in the detailed view of the back of the abutment in Fig. 1.

The entire girder is modeled as a single beam, and the joint is modeled as a rigid region. The response value of each main beam is calculated by calculating the response sharing ratio of each main beam using a grid structure model consisting of the main beam, cross beams, and a floor slab, and multiplying it by the design response value of the entire girder calculated in Fig. 16.

3.1.2 Structural analysis method

GRS integrated bridge using a PCT girder has a rigid frame structure due to the joint between the abutment and the girder. Since deformation due to concrete shrinkage and creep in the girder, and deformation due to prestressing are restrained, the response of a bridge changes over time as the shrinkage and creep progress.

Therefore, a structural analysis method is used that can calculate the response value using shrinkage strain and creep coefficient from the age of concrete when a structural system changes, such as when an abutment and a girder are joined.

3.1.3 Modeling for time dependent response characteristics of buffer layer spring

Figure 17 shows that the response characteristics of a buffer layer spring change over time due to shrinkage and repetition of temperature expansion of the girder. Therefore, it is preferable to perform time-dependent analysis taking into account changes in the response characteristics of the buffer layer due to the number of repetitions of temperature expansion, and shrinkage and creep of concrete.

However, at present, since it is not easy to model the change in response characteristics of a buffer layer, a buffer layer is modeled using a "strong spring" which is assumed immediately after construction and a "weak spring" assumed toward the end of the design service life. Because the process of change from "strong spring" to "weak spring" is unclear, the design uses both "strong spring" and "weak spring" as a buffer layer spring from the time of construction to the end of the design service life.

3.1.4 Response value for earthquake

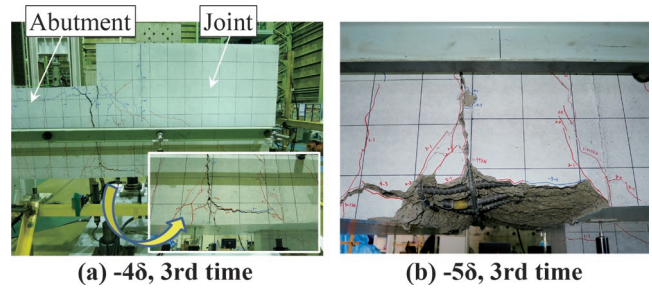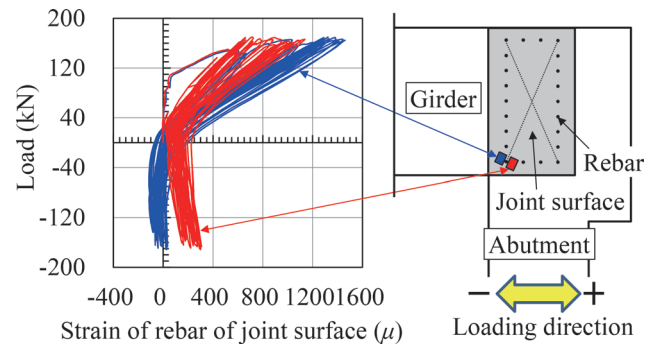When a bridge length is 20 m or less, the influence of the dy-

(a) -4δ, 3rd time   (b) -5δ, 3rd time

Fig. 14   Damaged condition

Fig. 15   Load-Strain of rebar of joint surface

Fig. 16   Structural analysis model

(a) Experimental result [4]   (b) Modeling for design [3]
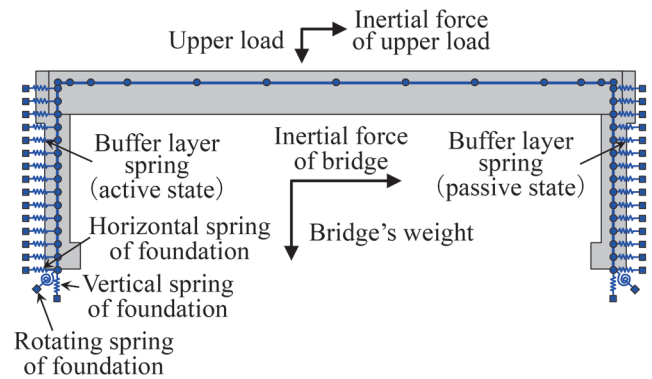
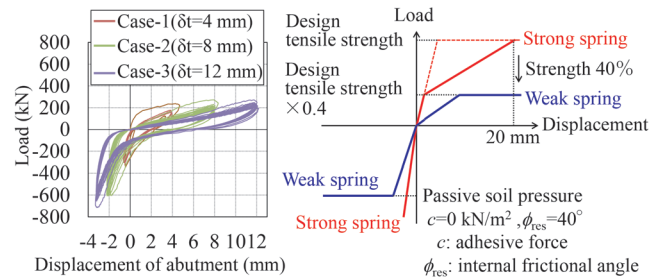**Fig. 17   Response characteristics of buffer layer spring and its modeling**

namic behavior of reinforced soil is greater than the influence of the dynamic behavior of a rigid frame. Therefore, the response value of a girder is calculated using the maximum response acceleration of the soil structure inspection wave shown in the seismic standard [11].

On the other hand, when a bridge length exceeds 20 m, the in-

fluence of the dynamic behavior of a bridge is greater than the influence of the dynamic behavior of reinforced soil, and it has been confirmed that the dynamic response of a bridge cannot be ignored [5]. Therefore, if a bridge length, which is expected to be applied to a PCT girder, exceeds 20 m, it is basically calculated on the basis of a dynamic analysis.

If reinforced soil is not damaged, a rigid frame is considered to have greater damping than a general ramen viaduct because it is integrated with reinforced soil and a rigid frame. Design response values may be calculated using the demand yield seismic coefficient spectrum for bridges and viaducts shown in the seismic standard [11].

A study of a response during an earthquake for GRS integrated bridge with a bridge length of 40 m using a PCT girder clarifies that even if seismic force exceeds an assumption in the design, all the members do not become plastic and maintain elastic behavior [6]. This is because a buffer layer spring on the pushing side bears the inertial force of a rigid frame.

Therefore, the seismic response characteristics of GRS integrated bridge change depending on whether the buffer layer spring is in a compressed state or a tensile state due to the temperature expansion and contraction of the girder [7].

When using a PCT girder, the temperature expansion and contraction of the girder is large, so it is necessary to consider the effect of temperature changes on an earthquake.

3.2 Verification for fatigue failure of geotextile

Table 4 shows required performance and performance items. When using a PCT girder, the shrinkage of concrete and temperature expansion and contraction of the rigid frame is large, as is the expansion and contraction of geotextiles. Therefore, the fatigue failure of geotextiles due to repeated temperature changes shall be checked.

From the examination of the repetitive response characteristics of geotextiles [3], if the tensile strain of geotextiles was less than 3%, fatigue failure of geotextiles did not occur, and so the verification was satisfied.

3.3 Verification for joint part of PCT girder and abutment

In the calculation of design response values, a joint is modeled in a rigid region, and the bending moment, shear force, and axial force are calculated at the member ends of a girder and an abutment.

Design limit values are calculated using design shear transmission strength V_{cwd} and design torsion transmission strength M_t by (1). In the calculation of design shear transmission strength, average compressive stress σ'_{nd} generated perpendicular to the joint surface is set to 0.0 N/mm², and a coefficient b considering the properties of the joint surface is set to 2/5.

In this joint structure, prestress is introduced using laterally tightened PC steel, therefore compressive stress is generated on the joint surface. However, the compressive stress generated on the joint surface is uncertain because the prestress force introduced into the joint is unclear due to being restrained from the abutment and reinforced soil. Therefore, $\sigma'_{nd} = 0.0$ N/mm² is set considering the judgment of safety.

In principle, a joint surface should be made uneven using a joint treatment agent such as a retarding agent. However, from the judgment of safety, $b = 2/5$ is set in consideration of fluctuations in the quality of a joint surface due to treatment agents, methods, construction management, and so on, and the opening of a joint surface due to shrinkage, and so on.

Table 4 Performance requirements and performance items

Performance requirements	Performance items (member)
Safety	Failure (abutment, girder, joint (**3.3**), geotextile)
	Fatigue failure (girder, geotextile (**3.2**))
	Running safety
	Stability
Serviceability	Aesthetic appearance (abutment, girder)
	Ride comfort
Restorability	Damage (abutment, girder, joint, geotextile)

4. Conclusions

This report introduced the proposed joint structure between a PCT girder and an abutment, and verification method for GRS integral bridge that should be noted especially when a PCT girder is used.

The design and construction guidelines for GRS integral bridge have been published [12]. The details of a design method can be used as a reference. On the basis of this guideline, GRS integrated bridge using PCT girders has already been constructed [13].

References

[1] T.Yonezawa, T.Yamazaki, M.Tateyama, and F.Tatsuoka, "Design and construction of geosynthetic-reinforced soil structures for Hokkaido high-speed train line," *Transportation Geotechnics*, pp. 3-20, 2014.

[2] Y.Shindo and F.Tatsuoka, "Restoration of Sanriku Railway by Utilizing Reinforced Soil Structures to Enhance Earthquake and Tsunami Resistance," *Journal of JSCE*, Vol. 5, pp. 10-26, 2017.

[3] S. Tamai, "Design Method of Serviceability Limit State to realize Long Span of Geosynthetic-Reinforced Soil Integral Bridge," University of Tokyo, doctoral thesis, 2018 (in Japanese).

[4] H. Kato, T. Morino, Y. Suyama, H. Aoki, and H. Nishioka, K. Kojima, "Repeated loading test of reinforced embankment wall assuming longer span of GRS integrated bridge," Proceedings of the *48th Japan National Conference on Geotechnical Engineering*, pp. 1543-1544, 2013 (in Japanese).

[5] T. Sasaki, H. Nishioka, S. Todoroki, S. Tamami, and T. Yamazaki, Y. Shindo, "Analytical Study of the Effect of Differences in Bridge Length on the Seismic Response of GRS Integrated Bridges," Proceedings of the *Annual Conference of the Japan Society of Civil Engineers*, Vol. 70, I-117, 2015 (in Japanese).

[6] T. Furuya, T. Shimotsu, S. Todoroki, S. Tamami, and M. Okamoto, "Examination of Constant and Seismic Response of Geosynthetic-Reinforced Soil Integrated Bridge using PRC girder," Proceedings of the *Annual Conference of the Japan Society of Civil Engineers*, Vol. 70, V-021, 2015 (in Japanese).

[7] T. Sasaki, H. Kato, H. Nishioka, T. Santo, T. Nishi, Y. Takano, Y. Suyama, and H. Aoki, "Analytical Study of the Effect of Temperature Expansion and Contraction of Long-Span GRS Integrated Bridges on Seismic Response," Proceedings of the *Annual Conference of the Japan Society of Civil Engineers*, Vol. 69, I-402, 2014 (in Japanese).

[8] Architectural Institute of Japan, *AIJ Standard for Structural Calculation of Reinforced Concrete Structures revised 2010*, Architectural Institute of Japan, 2019.

[9] H. Shibui, M. Kaji, K. Kusunoki, and A. Tasai, "An experimental study on the stress transfer mechanism in the soft-landing base-isolation system," *Proceedings of the Japan Concrete Institute*, Vol. 30, No. 3, pp. 1237-1242, 2008 (in Japanese).

[10] Railway Technical Research Institute, *Design Standards for Railway Structures and Commentary (Concrete Structure)*, Maruzen co., Ltd, Tokyo, 2004 (in Japanese).

[11] Railway Technical Research Institute, *Design Standards for Railway Structures and Commentary (Seismic Design)*, Maruzen co., Ltd, Tokyo, 2012 (in Japanese).

[12] Railway Technical Research Institute, *Design and Construction Guidelines for Geosynthetic-Reinforced Soil Integral Bridge (GRS Integrated Bridge)*, Railway Research-Culture Promotion Foundation, 2017 (in Japanese).

[13] D.Soga, Y.Takano, T.Yonezawa, M.Koda, M.Tateyama, and F.Tatsuoka, "Design and construction of various type GRS structures for a new high-speed railway," *Proceedings of the 11th International Conference on Geosynthetics*, 2018.

Authors

Shuntaro TODOROKI, Dr. Eng.
Senior Researcher, Concrete Structures Laboratory, Structures Technology Division
Research Areas: Concrete Structural Engineering

Masaru OKAMOTO, Dr. Eng.
Senior Chief Researcher, Concrete Structures Laboratory, Structures Technology Division (Former)
Research Areas: Concrete Structural Engineering

Hidetoshi NISHIOKA, Dr. Eng.
Senior Chief Researcher, Foundation & Geotechnical Engineering Laboratory, Structures Technology Division (Former)
Research Areas: Foundation & Geotechnical Engineering

Shinichi TAMAI, Dr. Eng.
Senior Director, Japan Railway Construction, Transport and Technology Agency, Design Department
Research Areas: Concrete Structural Engineering

Toyoji YONEZAWA
Senior Director, Japan Railway Construction, Transport and Technology Agency, Technological Management Department, Tokyo Regional Bureau
Research Areas: Foundation & Geotechnical Engineering

Hidekazu ISHII
Manager, Japan Railway Construction, Transport and Technology Agency, Yakumo Construction Site Office, Hokkaido Shinkansen
Research Areas: Concrete Structural Engineering

Floor Heave Mechanism and Effect of Countermeasures for Mountain Tunnels

Keisuke SHIMAMOTO   Kazuhide YASHIRO
Tunnel Laboratory, Structures Technology Division

Takeshi KAWAGOE
Geology Laboratory, Disaster Prevention Technology Division

In mountain tunnels, floor heave may gradually progress. However, the mechanisms underlying this phenomenon are not yet fully understood. Therefore, no countermeasure design method has to date been established. In this study, we first conducted a literature review of floor heave cases to study the underlying mechanisms. Then, drawing on the insights gained through the literature review, we reproduced the estimated mechanisms in a model experiment. Based on the results of these experiments, this paper proposes an explanation of the floor heave mechanism and a suitable countermeasure against this phenomenon. The effect of the countermeasure was evaluated by numerical analysis.

Key words: *mountain tunnel, floor heave mechanism, rock moisture content*

1. Introduction

Floor heave is a phenomenon which occurs progressively after tunnel construction is completed, and may appear as track displacement. Floor heave often progresses relatively slowly and does not immediately threaten safety, but the phenomenon rarely settles naturally, and some reinforcement is required.

Although the floor heave mechanism is generally explained as a squeezing (extrusion due to plasticization) and swelling (water absorption expansion) action [1], to date it has not been fully elucidated. Consequently, no design method for countermeasures in the event of floor heave has yet been established. Therefore, in this study, we investigate the mechanism of floor heave by conducting a literature review of floor heave cases and reproduce the mechanisms estimated from these cases through model experiments. Furthermore, by numerical analysis, we evaluate the effect of countermeasures which could be implemented in places where floor heave is confirmed [2].

2. Estimated mechanism of floor heave

Figure 1 shows a schematic diagram of floor heave due to squeezing and swelling. Floor heave due to squeezing occurs when the ground strength ratio (ratio of uniaxial compressive strength of the ground to overburden pressure) is small. This is a phenomenon in which a roadbed rises due to plasticization because the vertical stress becomes smaller than the horizontal stress in the roadbed where restraining pressure is small. On the other hand, floor heave due to swelling is a phenomenon in which water collects in the roadbed, and the swelling clay minerals in the roadbed absorb and expand, resulting in uplift of the roadbed.

Figure 2 shows a simplified mechanism of floor heave due to squeezing and swelling. As the main factor behind squeezing is weak ground strength, it is considered that the decrease in strength due to water content has a large effect on squeezing. Therefore, if the dilation angle is large, floor heave is exacerbated. The main cause of swelling is the expansion of the bottom spacing (distance between the bottom surface of crystals) due to the absorption of water by the swelling of clay mineral. This results in an overall volume expansion that causes floor heave.

In both cases, changes in the water content of the ground below the invert are a major factor. It is considered that floor heave progresses over a long period of time as water content gradually increases or decreases from the time of excavation over a long period of a year.

In this paper, the floor heave mechanism is described in Section 3; Section 4 reviews the literature and describes the model experiments; Section 5 explains the inference of the mechanism based on these results; and Section 6 evaluates the effect of countermeasures through numerical analysis.
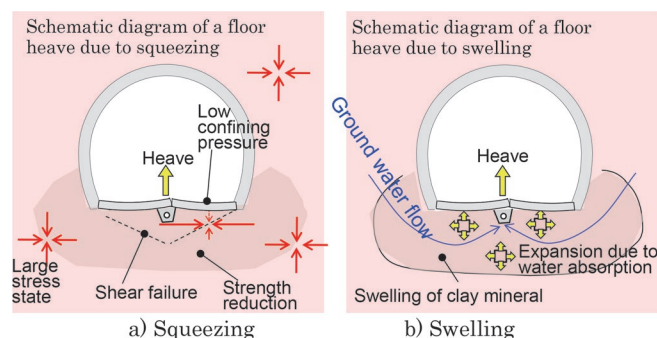

a) Squeezing   b) Swelling

Fig. 1   Schematic diagram of floor heave
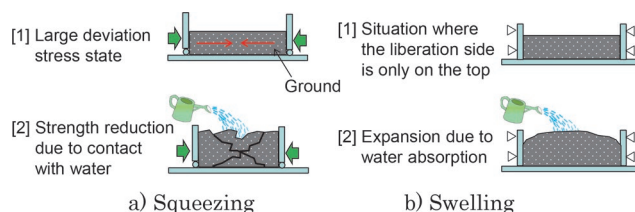

a) Squeezing   b) Swelling

Fig. 2   Simplified floor heave mechanism

3. Case analysis through literature review

3.1 Case analysis target

For the purpose of understanding the mechanism of floor heave in mountain tunnels, we conducted a literature survey of floor heave cases. The analysis concentrated on 26 tunnels featured in published literature in Japan.

3.2 Regional characteristics of tunnels with floor heave

Figure 3 shows the locations of the 26 tunnels with floor heave (tunnels A to Z), identified in the literature survey, on a map of Japan.

The map also shows the so-called "green tuff area," where sediments associated with Neogene Miocene volcanic activity are thickly distributed. Tuff and mudstone containing smectite are thickly deposited in green tuff areas, and it can be seen that tunnels suffering floor heave are concentrated in these areas.

Floor heave occurs in similar places, and it can be said that they are deformations that are very strongly related to geological factors. If there is a tunnel with floor heave in the vicinity, it can be said that sufficient care must be taken during construction to avoid similar damage in other areas with a similar geology.

3.3 Information obtained from literature

Among the cases analyzed through the literature survey, the case of J tunnel [3] is particularly informative. On August 13, 2008, 17 years after the J tunnel was put into service, a 250 mm floor heave suddenly occurred, forcing a complete closure for 3 months, for investigations and countermeasures.

As a mechanism, it has been pointed out that the water in the central drainage pipe may have permeated the roadbed for a long time during operation [3]. Since the invert uplift is progressing rapidly, it is considered that the earth pressure acting on the tunnel increased sharply.

In this case, water was not supplied to the roadbed so much until August 13, but on August 13, there was a sudden surge in the water supply due to damage to the invert, and the ground pressure

action increased sharply. It is speculated that this may have led to the sudden heaving.

3.4 Heave mechanism inferred from case analyses

Reference [4], the amount of spring water in the tunnel face observation records was analyzed for the 626 faces (17 sections of 11 tunnels) of the Shinkansen tunnels where floor heave occurred.

The results of this analysis revealed that 94% of the faces where floor heave occurred after completion had little or no spring water at the time of excavation. 94% of the faces with floor heave is much higher than 75%, that of without floor heave.

In addition, there are relatively many cases (75%) where there is no spring water in the face without floor heave. The reason for this is thought that the analysis target is tunnels with floor heave. Floor heave are more likely to occur in muddy soft rock grounds, where the amount of spring water from the face is relatively small.

On the Basis of this and the results of this literature survey, the following mechanism of floor heave can be considered as a hypothesis.

"After a tunnel is completed, water is supplied to ground with low water content via drainage pipes, etc. The ground absorbs water weakening it, leading to floor heave. In mountains with low permeability, the weakening process is slow due to water absorption, and deterioration may progress over a long period of time."

In other words, before tunnel excavation, the ground is restrained by the overburden pressure and is in a triaxial compression state, so deterioration does not progress even if it is saturated below the groundwater level. However, after excavation, the tangential stress of the ground around the tunnel increases, so that cracks open and loosening occurs.

If there is spring water during excavation, water permeation into the cracks causes weakening at the time of excavation and an increase in displacement during excavation, so that structural measures need to be taken. On the other hand, if the amount of spring water at the time of excavation is small, the displacement will not become apparent immediately after excavation, and the ground will deteriorate due to the water supply after completion without any structural measures, leading to floor heave.
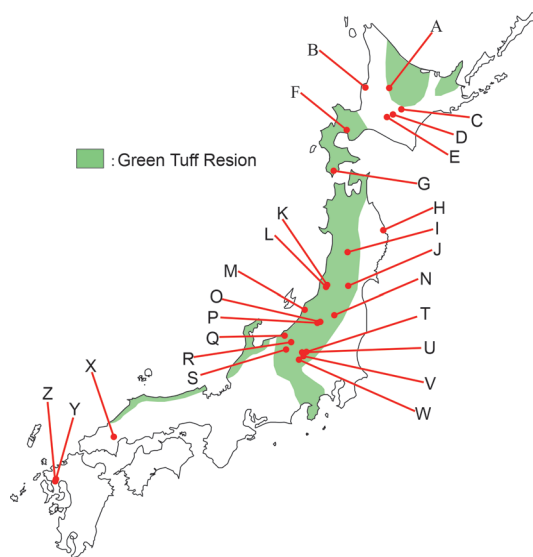
4. Experiment to reproduce floor heave due to contact with water

In the previous chapter, from the results of the literature survey, it was considered that one of the causes of floor heave following tunnel completion was that the ground under the invert came into contact with water, weakening the ground. Therefore, in this chapter, we conducted a model experiment to confirm whether the dry ground under the invert comes into contact with water and the strength decreases, causing floor heave.

4.1 Experimental procedure

The outline of the experiment is shown in Fig. 4. In this experiment, mudstone collected from the tunnel face was placed under the invert of the tunnel model, and water was supplied from outside the model for it to absorb water while lateral pressure was applied, and the resulting behavior was confirmed.

The tunnel model was made of a 1/50 scale mortar model of a Shinkansen tunnel. Since horizontal stress is predominant in the stress state of an invert ground ridge after actual tunnel excavation,

Fig. 3   Regional characteristics of the floor heave tunnel

a load was applied in the horizontal direction to simulate it. A 10 mm thick piece of EPS (Styrofoam) is is attached to the back side of the side wall of the lining. The presence of EPS with relatively low rigidity, meant that the invert ground ridge became dominant in the horizontal stress, and the stress state under the invert when excavating a tunnel (Fig. 1a) was simulated. A low-strength mortar (uniaxial compressive strength qu = 0.5 MPa) was used as the simulated ground.

The procedure of the experiment was as follows:

[1] The tunnel model was installed in the center of a soil tank with the tunnel longitudinal direction facing vertically, and low-strength mortar was placed around the tunnel model as the simulated ground.

[2] After the low-strength mortar was hardened, mudstone that had been dried in a drying oven was laid under the invert. The mudstone used was crushed to a particle size of less than 26 mm. The mudstone was sifted so that it had a predetermined particle size distribution, and the gaps were filled with No. 6 silica sand.

[3] A plane strain state was realized by fixing the upper surface of the soil tank with a lid during loading. For loading, the displacement of the loading plate was controlled to 0.2 mm / min on the left side of the soil tank until the specified loading stress of 600 kPa was reached.

[4] After holding the load for 24 hours, the hose shown in Fig. 4 was used to allow the mudstone under the invert to absorb sufficient water.

Since the length of the tunnel was 300 mm and the water pressure for a vertical height of 300 mm was 3 kPa, the influence of the water pressure on the invert deformation was sufficiently small.

When the same rock pieces used in the experiment were immersed in water after drying, rock pieces that became completely muddy and rock pieces that did not generate cracks were mixed as shown in Fig. 5.
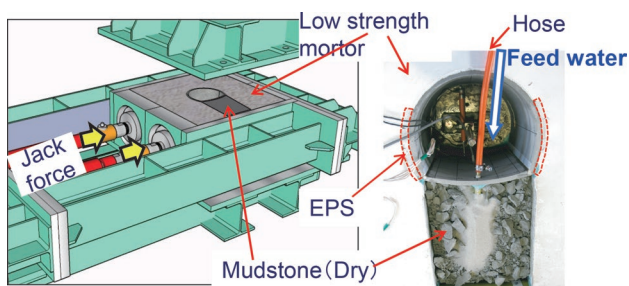

Fig. 4   Outline of the experiment

a) Before immersion   b) 5 minutes later   c) 4 hours later

Fig. 5   Inundation of the same rocks used in the model experiment

4.2 Experiment results

Figure 6 shows the changes over time course of the pressure acting on invert and invert displacement. At first, after the initial loading assuming excavation, creep-like heave occurs while the load was kept constant. When the heave had almost settled, water was supplied to the dry mudstone under the invert. Finally, the pressure acting on the invert and the heave of the invert suddenly increased.

Figure 7 shows the changes in particle size before and after the experiment.

As shown in Fig. 5, there were many rock fragments that became muddy due to immersion in the absence of confining pressure.

On the other hand, in the triaxial stress state as in this experiment, although the heave progressed, the rock fragments did not become muddy but became slightly smaller.

In actual tunnel floor heaving, when the ground under the invert is checked, it is often found that there is no significant deterioration. Even if there is no significant deterioration in the ground under the invert, it is considered that the deterioration of the ground is progressing and may lead to heaving.
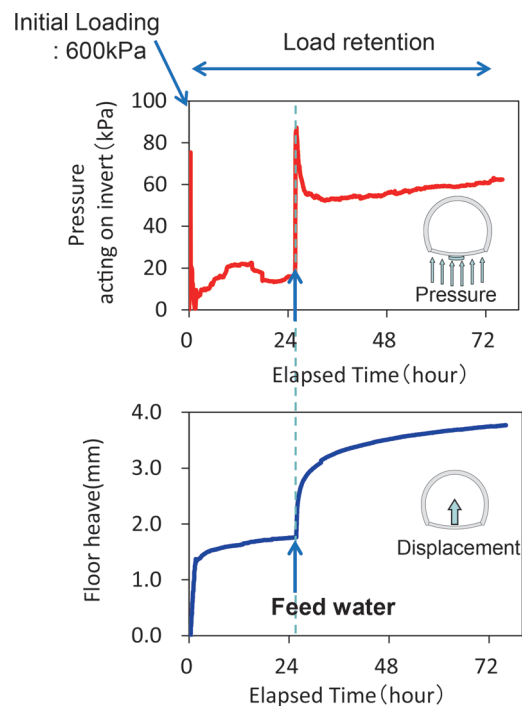

Fig. 6   Changes over time of the pressure acting on invert and invert displacement
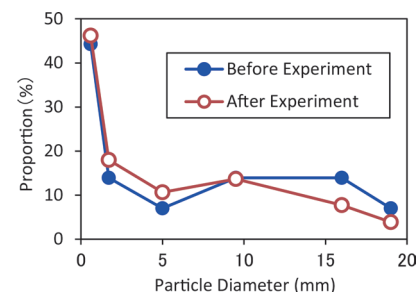

Fig. 7   Changes in particle size before and after the experiment

4.3 Mechanism inferred from model experiment results

The results obtained in this experiment are as follows:

-In ground that is easily deteriorated by water content, the ground pressure acting on the invert increases due to contact with water. At that time, converged displacement that is once converged increases.

-If the water flowing through the drainage pipe leaks to the ground below the invert because of damage to the concrete invert, there is a possibility that floor heave may progress rapidly.

-From the experiment results, the following can be considered as being among the mechanisms underlying floor heave, which occurs after the tunnel is completed.

[1] Due to excavation, the vertical stress in the ground of the roadbed lessens, horizontal stress increases, as does the deviatoric stress, resulting in instability. Along with this, cracks open and loosening occurs. This loosening leaves room for water absorption and deterioration. If the amount of spring water during excavation is small, the roadbed dries during excavation, leaving room for water absorption and deterioration in the future.

[2] If water is supplied to the ground under the invert because of damage to the drainage pipe after the invert is introduced, the ground will absorb water and weaken.

[3] Weakening causes stress that cannot be retained to be released and redistributed, and the ground pressure acting on the invert increases, causing floor heave.

5. Floor heave mechanism hypothesis

On the basis of the results of the above literature survey and model experiment, the scenario shown in Fig. 8 illustrates the assumed mechanism causing floor heave after tunnel completion. It is noted that the figure shows the flow of the scenario when the floor heave occurs, and it is assumed that the ground strength ratio is small to some extent and that the ground is a soft rock ground that is slaking.

Considering reference (5) which showed that in 94% of cases, where floor heave occurred after tunnel completion, there was either just bleeding or no spring water flow, it is considered that there are only few cases corresponding to scenario [3] and the most common
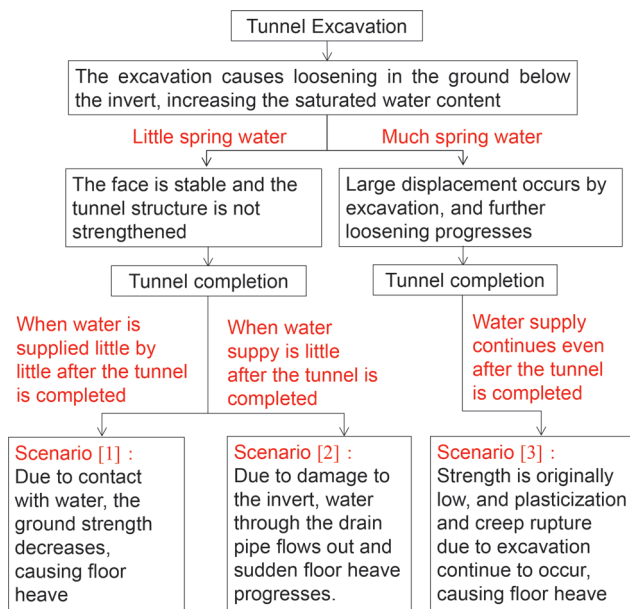

Fig. 8   Floor heave mechanism after the tunnel was completed

scenario is [1]. Considering floor heave mechanisms such as the ones described in scenario [1] and scenario [2], if there is less water during excavation and more water flows through the drainage pipe after the tunnel is completed, the floor heave risk will be greater than otherwise.

The following can be considered as the water supply source of the scenario [1]: "there is no spring water at the time of invert excavation and water is supplied little by little after the tunnel is completed." That is, we can imagine the formation of water that reaches from the upstream side via the drain pipe, or the formation of a new water path by loosening due to excavation.

6. Evaluation of countermeasure effect through numerical analysis

In this chapter, the effect of the mitigation work, such as downward rock bolts, is evaluated by numerical analysis.

Floor heave by numerical analysis has been expressed as a decrease in the strength of the ground (3). This is consistent with the results of the model experiment in Section 4.

6.1 Analysis conditions

The analysis model diagram is shown in Fig. 9. The overburden was set to 200 m, and the overburden load was applied to the ground as the initial stress, and then the vertical displacement of the upper boundary was fixed. The lateral pressure coefficient was 1. The cross-sectional shape of the tunnel is the Shinkansen standard. The excavation by NATM was modeled by three-dimensional sequential excavation analysis, and then the analysis to express the floor heave after completion was carried out. Floor heave after completion was expressed by the decrease in the strength of the ground considering the influence of loosening of the ground during excavation. In order to cover a period of up to 10 years after completion, the strength decrease and the elapsed years are associated in advance based on the deformation reproduction analysis result [3] of an actual tunnel.

The physical characteristics of the ground are as shown in Table 1, while the ground and concrete were modeled as Mohr–Coulomb failure criterion, and concrete was also expressed for softening due to tensile fracture.

Figure 10 shows the analysis case. We implemented four cases: no countermeasures, downward RB (rock bolt), combination of three reinforcement methods; (downward RB, filling the central passage, and reinforcing the corners), and recasting a thick invert with a small curvature.
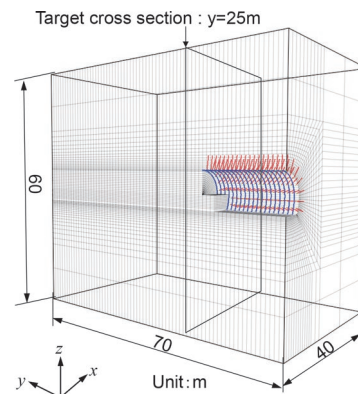

Fig. 9   Analysis model

The central passage filling and corner reinforcement are structural reinforcements proposed as measures that can be constructed rapidly, even in the short intervals during railway operation. Figure 11 illustrates the method in a schematic diagram.

The anchors buried in the central passage and reinforced at the corners are represented by cable elements. The cable element is a structural element that connects mass points with a shaft spring and expresses slippage and separation from peripheral elements by a shear spring and a slider. The model is modeled with an anchor hole diameter of 22 mm, a reinforcing bar diameter of 19 mm, an embedding length of 285 mm, and a yield load of 164 kN. The pitch in the longitudinal direction is 250 mm. Axial reinforcing bars are not modeled assuming a two-dimensional situation in a state of plane strain. The downward RB has a hole diameter of 65 mm, a reinforcing bar diameter of 25 mm and length of 6 m, and is represented by a Cable element. RB expresses the washer by preventing relative displacement from occurring between the head of the RB and the upper surface of the invert.

Table 1　Physical characteristics of the ground

Physical property		unit	value
Overburden	h	m	200
Uniaxial compressive strength	q_u	MPa	2.0
Ground strength ratio	C_f	-	0.5
Specific weight	γ	kN/m³	20
Elastic modulus	E	MPa	206
Poisson's ratio	ν	-	0.36
Cohesion	c	kPa	580
Internal friction angle	φ	°	31
Dilation angle	λ	°	10
Lateral pressure coefficient	K_0	-	1.0
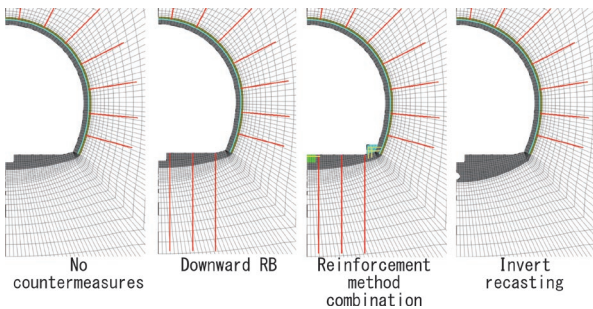
Fig. 10　Predictive evaluation cases of the effect of suppressing floor heave of reinforcement workers
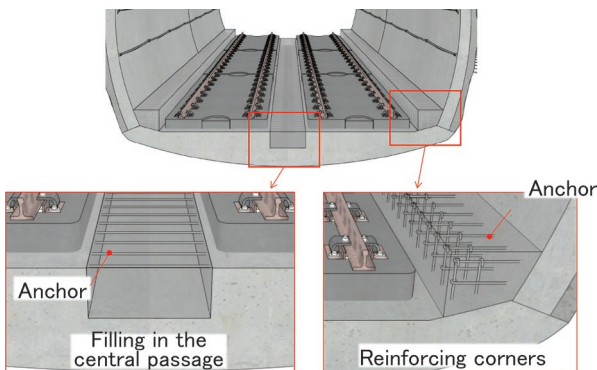
**Fig. 11　Filling in the central passage and reinforcing corners**

6.2　Analysis result

Figure 12 shows the time course of floor heave at the central passage position along with the time course of ground cohesion. Since cohesion c of the ground decreases with looseness of the ground, c differs from location to location. It is noted that this figure shows c of the element with the largest decrease in strength. From this, it can be seen that the effect of suppressing floor heave can be seen in all the countermeasures, but it can be seen that the floor heave can be further reduced by combining various measures.

Although it is difficult to construct measures to increase the curvature of the invert in a short period of time while trains are operating, the result is drastic and most effective.

Figure 13 shows the contour diagram of the maximum principal strain (tensile strain) after 10 years. Fig. 13 indicates that the embedding length is important because cracks occur at the embedding end of the anchor, although cracks in the central passage are prevented.
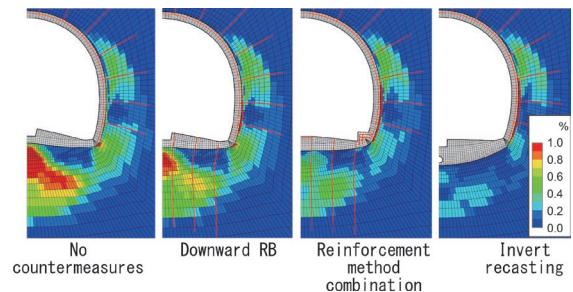
Figure 14 shows the shear strain contour diagram of the ground after 10 years. It can be seen that the structural reinforcement improves the rigidity of the tunnel, reduces floor heave, and suppresses shear strain of the ground.
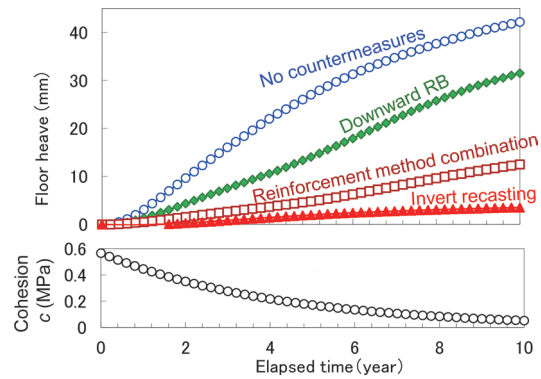
Fig. 12　Time course of floor heave
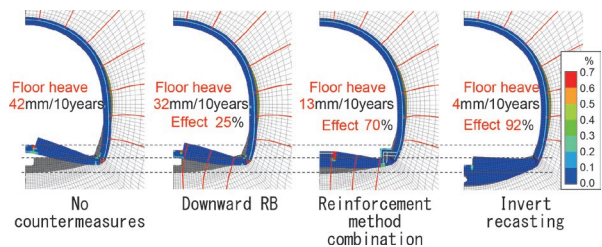
Fig. 13　Tensile strain contour diagrams (displaying deformation magnified 30 times)

Fig. 14　Shear strain contour diagrams (displaying deformation magnified 20 times)

7. Conclusion

In this study, we conducted a case analysis and model experiments, and on the basis of the obtained results, we explored the floor heave mechanism as a result of change in the water content ratio of the ground. Furthermore, the effect of the floor heave countermeasure work was evaluated by numerical analysis.

The main findings are summarized below.

1) From a literature survey, it was found that there are many cases of floor heave in situations where contact between the ground and water is suspected.

2) Model experiments confirmed that when dry rocks that are easy to slake are placed under the invert and water is supplied after reproducing a stressed state, sudden floor heave occurs.

3) The floor heave mechanisms were organized into a flow chart, by focusing on the presence of spring water during excavation and water supply after completion. In particular, we showed a scenario in which floor heave occurs after tunnel completion in ground where there is little spring water during excavation.

4) We demonstrated methods for evaluating the effect of countermeasures through numerical analysis. In addition, we showed that floor heave suppression may be improved by combining various measures.

In the future, by coupling the proposed analysis method with seepage flow analysis, we will express analytically the mechanisms underlying floor heave with changes in the water content ratio, and also work on the evaluation of countermeasures such as groundwater level lowering methods.

In European countries such as Germany and Switzerland, floor heave due to swelling of anhydrite has been a problem [5]. Since this phenomenon is also greatly affected by water, some of the findings obtained in this paper may be useful.

References

[1] Shimamoto, K., Yashiro, K., Kojima Y., Nakanishi, Y., Tsukada, K. and Asakura, T., "Study on the Mechanism of Heaving and its Countermeasures in Mountain Tunnels," *ITA-AITES World Tunnel Congress 2012*, Bangkok, 2012.

[2] Shimamoto, K., Yashiro, K., Kawagoe, T., "Floor Heave Mechanism and the Effect of Countermeasures for Mountain Tunnels," *RTRI REPORT*, Vol. 35, No. 7, 2021 (in Japanese).

[3] Sakuma, S., Sugawara, N., Tada M. and Endo, Y., 2009, Tunnel Invert Restoration of Sudden Heaving Deformation in Service –Yamagata Expressway Sakazukiyama Tunnel (In-bound Line), *Tunnels and Underground*, Vol. 40, No. 12, pp. 27-37, 2009 (in Japanese).

[4] Kobayashi, H., Shimotsu, T., Ueno, H., Watanabe, K., Shimamoto, K. and Asakura, T., "Basic Study on the Inhibitory Effect of Invert Arch Structure against the Long Term Heaving," *Journal of Construction Management and Engineering VI*, Vol. 72, No. 3, pp. I_96-I_107, 2016 (in Japanese).

[5] Schweizer, D., Prommer, H., Blum, P., Siade, A.J. and Butscher, C., "Reactive transport modeling of swelling processes in clay-sulfate rocks," *Water Resour Res*, 54 (9), pp. 6543-6565, 2018.

Authors

Keisuke SHIMAMOTO, Dr. Eng.
Senior Researcher, Tunnel Laboratory,
Structure Technology Division
Research Areas: Tunnel, Mountain Tunnel,
Tunnel Maintenance

Takeshi KAWAGOE, Dr. Eng.
Senior Chief Researcher, Head of Geology
Laboratory, Disaster Prevention Technology
Division
Research Areas: Engineering Geology,
Mountain Tunnel

Kazuhide YASHIRO, Dr. Eng.
Senior Chief Researcher, Head of Tunnel
Laboratory, Structure Technology Division
Research Areas: Tunnel, Mountain Tunnel,
Tunnel Maintenance

Restoration Technology of Embankment Reusing Collapsed Soil

Kohei KASAHARA   Susumu NAKAJIMA
Foundation & Geotechnical Engineering Laboratory, Structure Technology Division

Tatsuki FUJIMOTO
Foundation & Geotechnical Engineering Laboratory, Structure Technology Division (Former)

Yoshitaka TOMIDA
Foundation & Geotechnical Engineering Laboratory, Structure Technology Division

Recent years have seen the collapse of embankments due in many cases to heavy rain in Japan. It is difficult to re-compact embankments which have suffered this type of collapse, because the collapsed soil contains a large amount of water. Another problem is that existing embankments in Japan are often constructed of materials which do not comply with current regulations of Japanese railway. For these reasons, conventionally, since the collapsed soil can't be reused, purchased soil is used for restoration in Japan. However, this approach is both time consuming and costly. This paper proposes a new restoration method which reuses the soil from the collapsed embankment by utilizing the dehydrating effect of lime and by increasing soil strength by compaction.

***Key words**: embankment, collapsed soil, compaction, degree of saturation, Lime improvement, restoration method*

1. Introduction

Recent years have seen the collapse of embankments due in many cases to heavy rain in Japan. It is difficult to re-compact embankments which have collapsed in this way, because the collapsed soil contains a large amount of water. In addition, most of the existing embankments in Japan have often been constructed with materials which do not comply with current Earth structure standards of Japanese railway [1] (hereinafter referred to as non-compliant materials), because most of the existing embankments in Japan were constructed before material regulations and construction management regulations of Japanese railway were established. For these reasons, since the collapsed soil can't be reused, purchased soil is often used for restoration in Japan. However, this method presents problems in terms of time needed for construction, cost, and environmental load because it is necessary to dispose of collapsed soil and transport purchased soil.

On the other hand, Lime improvement is a known soil stabilization method. This method not only increases the stability and strength of the soil but also improves its workability during compaction due to the dehydration effect [2]. Therefore, even if the collapsed soil contains a large amount of water, the embankment can be re-compacted by dehydrating it with lime. However, an indoor mixing strength test is necessary to determine how much lime needs to be added because conventional Lime improvements utilized in railway embankment construction are mainly expected to increase the strength of soil. Therefore, this method is often not adopted for disaster recovery, which requires quick restoration. However, since the dehydration effect of lime is highly immediate, by constructing a new restoration method focusing on the dehydration effect rather than increasing strength, it is considered that Lime improvement can also be used when quick restoration is required such as disaster recovery.

Regarding the material regulations for embankments, the current Earth structure standards stipulate materials applicable for embankments and the degree of compaction according to required

performance level determined by the importance of the earth structure (Table 1). Although such material regulations and construction management standards are determined on the basis of experience and verification test results, the current Earth structure standards are not taken into account the effect of degree of saturation because the relationship degree of saturation and embankment strength had been unclear. However, recent studies have confirmed that not only the degree of compaction but also the degree of saturation are highly correlated with embankment strength [3]. Therefore, by utilizing this knowledge, if the relationship between the degree of compaction, the degree of saturation, and the strength can be evaluated quantitatively in order to consider both the degree of compaction and the degree of saturation, it may be possible to propose a new restoration method for embankments reusing collapsed soil of non-compliant material.

On the basis of the above background, in this paper, we propose a new restoration method for embankments which reuses the soil from the collapsed embankment by utilizing the dehydrating effect of Lime improvement and increase in soil strength by compaction. As for the Lime improvement proposed in this paper, an indoor mixing strength test which is conventionally required can be omitted because the lime addition rate is determined from the viewpoint of the dehydration effect. In terms of construction management of compaction after the Lime improvement, the proposed method focuses on the relationship between the degree of compaction, the degree of saturation, and the strength. This proposed method has a feature that the collapsed soil can be reused by improving the degree of compaction even if the collapsed soil is non-compliant material.

In this paper, in proposing this new restoration method, we first investigate the actual condition of existing embankments in chapter 2. Chapter 3 describes the triaxial compression tests and construction tests which were conducted to examine the effects of the degree of compaction and the degree of saturation on the strength and rigidity of the embankment. Chapter 3 also quantifies the compaction effect on the basis of these test results. Then, chapter 4 proposes the new restoration method which reuses soil from collapsed embank-

Table1 Material regulations and construction management regulations for embankments

Performance rank	Upper part of embankment			Lower part of embankment	
	Material	Degree of compaction	K_{30}-value	Material	Degree of compaction
I	・〔Group A〕 ・〔Group B〕 after soil stabilization 　(Only materials with less fine fraction) ・Such as Recycled resources 　which are industrial by-products	Average value: 95% or more (Lower limit 92%)	Average value: 110 MN/m³ or more (Lower limit 70 MN/m³)	・〔Group A〕 ・〔Group B〕 after soil stabilization 　(Only materials with less fine fraction) ・Such as Recycled resources 　which are industrial by-products	・Gravel Average value: 90% or more Lower limit: 87% ・Sand Average value: 95% or more Lower limit: 92%
II	・〔Group A〕，〔Group B〕 ・〔Group C〕，〔Group D1〕，and 　〔Group V〕，after soil stabilization ・Such as Recycled resources 　which are industrial by-products	Average value: 90% or more (Lower limit 87%)	・Average value: 70 (Lower limit 50) MN/m³ ≦ K_{30}-value < 110 (Lower limit 70) MN/m³ ・Average value: 110 MN/m³ or more (Lower limit 70 MN/m³)	・〔Group A〕，〔Group B〕 ・〔Group C〕，〔Group D1〕，〔Group D2〕， 　and 〔Group V〕，after soil stabilization ・Such as Recycled resources 　which are industrial by-products	Average value: 90% or more Lower limit: 87%
III	・〔Group A〕，〔Group B〕 ・〔Group C〕，〔Group D1〕，and 　〔Group V〕，after soil stabilization ・Such as Recycled resources 　which are industrial by-products	Average value: 90% or more	Average value: 70 MN/m³ or more	・〔Group A〕，〔Group B〕，〔Group C〕 ・〔Group D1〕，〔Group D2〕and 〔Group V〕， 　after soil stabilization ・Such as Recycled resources 　which are industrial by-products	・Average value: 90% or more ・Air-dry v_a: (a) when F_c is 50% or more 　$v_a ≦ 10\%$ (b) when F_c is 20～50% 　$v_a ≦ 15\%$ F_c: fine fraction content
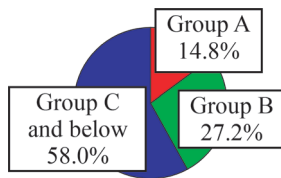
Fig. 1 Group classification of existing embankments (917 samples)

ments, and this proposed method is verified in chapter 5.

2. Investigation of actual condition of existing embankments

Prior to proposing a restoration method for embankments reusing collapsed soil, the actual condition of existing embankments was investigated to understand their current state. Figure 1 shows the analysis results of group classification of 917 existing sample embankments [4]. As a result of the analysis, the materials of group C and below accounted for 58% of the total. As shown in Table 1, under the current regulations, the materials of group C and below cannot be applied to the upper embankment without soil stabilization. Therefore, this investigation revealed that most existing embankments are made of non-compliant materials which do not meet current regulations.

Regarding the materials in group C and below, soil materials where the liquid limit w_L exceeds 50% were classified in group D and below. It has been pointed out in past standards that the materials in group D and below present a risk of mud pumping. In addition, even if w_L is less than 50%, materials which contain organic matter or volcanic ash may become significantly destabilized during rainfall. Therefore, it is considered that the materials in group D and below, and the materials containing organic matter or volcanic ash should not be reused as embankment materials.

On the basis of the above investigation of the actual condition and changes in past standards, it can be said that the non-compliant material which can be applied to this proposed method is group C material.

3. Experimental study for strength and rigidity of collapsed soil

In order to propose a restoration method for embankments reusing collapsed soil of non-compliant material, the relationship between the degree of compaction, the degree of saturation, and the strength were evaluated quantitatively in this chapter. Specifically, the triaxial compression tests and construction tests were conducted in various compaction and saturation conditions.

3.1 Triaxial compression test

(1) Materials and methods for tests

Table 2 shows the materials used in the test and the test conditions. The materials used in the test are classified into group B and group C in the Earth structure standard. Specimens with a diameter of 70 mm and a height of 150 mm were manufactured for the tests. The specimens were isotropically consolidated to the specified confining pressure (50 kPa, 100 kPa, 150 kPa). After that, the specimens were monotonically loaded under the exhaust and drainage conditions in partial saturation conditions.

The specimens were prepared under the conditions of optimum degree of saturation S_{ropt} [3], which gives the maximum dry density ρ_{dmax}, the S_{rL} on the dry side, the S_{rU} on the wet side, and the optimum water content w_{opt}. Furthermore, some materials were tested in saturated conditions, assuming a saturated situation due to rainfall. The setting conditions for ρ_{dmax} in each test case are shown in Table 2.
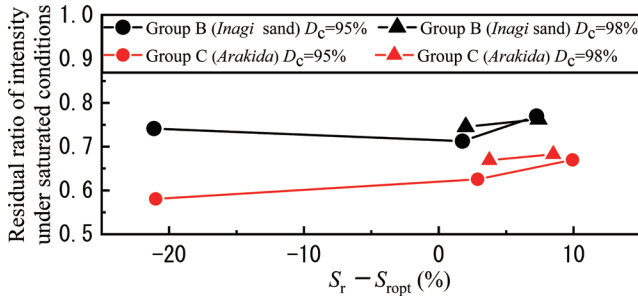
(2) Test results

Figure 2 shows the relationship between the strength and the degree of compaction obtained in the test. Where, the maximum internal friction angle φ_{peak} is used to evaluate the strength. As shown in Fig. 2, it was confirmed that even the group C material of non-compliant material can exhibit about the same strength as the

Table 2 Materials and cases for tests

Group classification	Materials			Degree of compaction D_c	Condition of water content or degree of saturation
Group B	Sample 1	Gravel	GF-S	90%, 95%, 98% (ρ_{dmax} is based on E-method)	S_{rL}, S_{ropt}, S_{rU}
	Sample 2	Sand	SFG	90%, 95%, 98% (ρ_{dmax} is based on E-method)	S_{rL}, S_{ropt}, S_{rU}
	Sample 3	Gravel	GFS	90%, 95%, 98%, 100% (ρ_{dmax} is based on E-method)	S_{rL}, S_{ropt}, S_{rU}
	Sample 4	Sand	SFG	90%, 95%, 98%, 100% (ρ_{dmax} is based on E-method)	S_{rL}, S_{ropt}, S_{rU}
	Sample 5	Sand	SF	90%, 95%, 98%, 100% (ρ_{dmax} is based on E-method)	S_{rL}, w_{opt}, S_{ropt}, S_{rU}
	Sample 6	Sand	SF	90%, 95%, 98% (ρ_{dmax} is based on B-method)	S_{rL}, w_{opt}, S_{ropt}, S_{rU}
	Sample 7	Sand	SF	90%, 95%, 98% (ρ_{dmax} is based on B-method)	S_{rL}, w_{opt}, S_{ropt}, S_{rU}
Group C	Sample 8	CL		90%, 95%, 98% (ρ_{dmax} is based on E-method)	S_{rL}, S_{ropt}, S_{rU}
	Sample 9	CL		90%, 95%, 98% (ρ_{dmax} is based on E-method)	S_{rL}, w_{opt}, S_{ropt}, S_{rU}
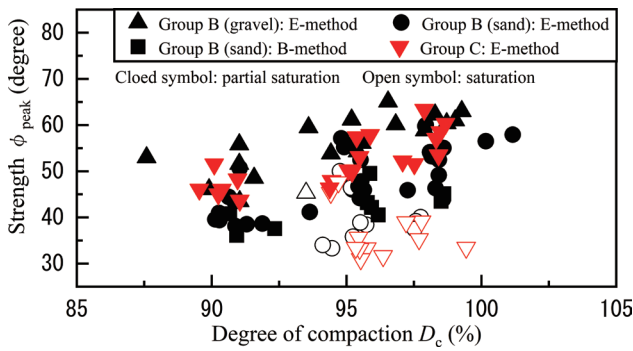
Fig. 2 Relationship between strength and degree of compaction

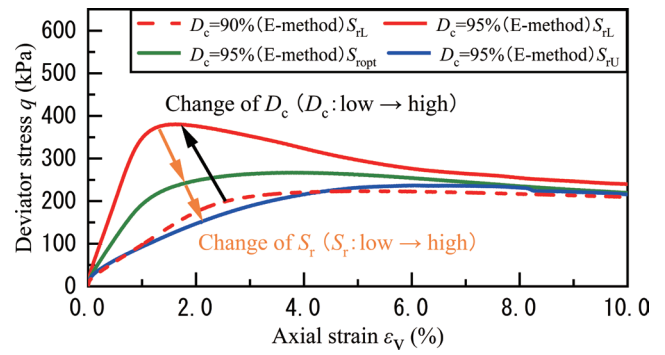Fig. 3 Residual ratio of intensity under saturated conditions

Fig. 4 Example of relationship between deviator stress and axial strain (*Inagi* sand: group B material)

Fig. 5 Example of relationship between φ_{peak} and D_c (*Inagi* sand: group B material)

Table 3 Strength evaluation formula

Group classification	Strength evaluation formula
Group B (sand)	$\phi_{peak} = (\sigma_3/50)^{-0.1833} \times 0.0093(239.3 - S_r) \times (D_c - 63.0)$
Group B (gravel)	$\phi_{peak} = (\sigma_3/50)^{-0.1658} \times 0.0107(212.9 - S_r) \times (D_c - 55.9)$
Group C	$\phi_{peak} = (\sigma_3/50)^{-0.1880} \times 0.0091(248.0 - S_r) \times (D_c - 60.8)$

※ σ_3 : Confining pressure (kPa)

Fig. 6 Comparison of calculated value and experimental value of φ_{peak}

group B material of compliant material by increasing the degree of compaction.

On the other hand, Fig. 3 shows the relationship between the residual ratio of intensity under saturated conditions (the ratio of φ_{peak} in partial saturation conditions to φ_{peak} in saturation conditions) and S_r-S_{ropt} (the difference between the degree of saturation S_r and the optimum degree of saturation S_{ropt}). This figure shows that the rate of decrease in strength from partially saturated condition to saturated condition was larger with group C materials than group B materials. Therefore, when using group C materials, we consider that it is necessary to take measures such as increasing the degree of compaction during construction and taking appropriate drainage measures to prepare for the decrease in strength in saturated conditions.
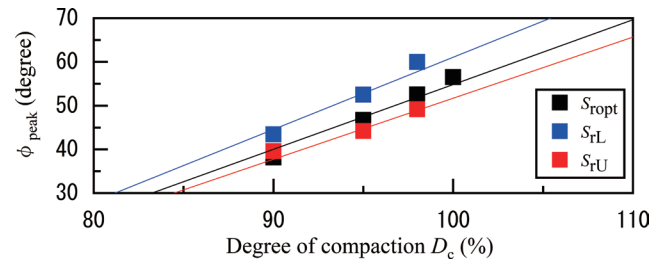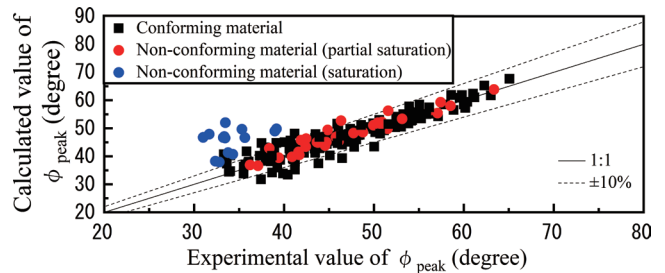
(3) Quantification of compaction effect

In this section, we propose a strength evaluation formula that can quantitatively evaluate the compaction effect based on the results of the triaxial compression test. Regarding the rigidity, we decided not to formulate it because the coefficient of subgrade reaction K_{30}-value which is related to rigidity can be confirmed relatively easily by small FWD testing (impact loading test by dropping a small weight) at the time of construction. Figure 4 shows an example of the relationship between deviator stress and axial strain of group B material (*Inagi* sand). This Figure shows that the strength increased by raising the degree of compaction D_c, while the strength decreased by increasing the degree of saturation during compaction. On the basis of this result, it is considered that both the degree of compaction D_c and the degree of saturation S_r should be considered to quantify the compaction effect of embankments.

Regarding the relationship between the degree of compaction, the degree of saturation, and strength, Fig. 5 shows the relationship

between the strength φ_{peak} and the degree of compaction D_c for each degree of saturation S_r for *Inagi* sand in group B material. From this figure, it can be seen that φ_{peak} increases almost linearly with the increase in the degree of compaction D_c when the degree of saturation S_r is constant. Table 3 shows the strength evaluation formula constructed by organizing the data in the same way as Fig. 5 for the materials in group B (sand and gravel) and group C. By arranging the relationship between the degree of compaction, the degree of saturation, and strength in this way, we constructed a strength evaluation formula obtained from the degree of compaction and the degree of saturation. In this proposed formula, the formula is corrected on the basis of the confining pressure of 50 kPa considering the influence of the confining pressure σ_3.

Figure 6 shows the relationship between the calculated value of φ_{peak} obtained from the strength evaluation formula and the experimental value of φ_{peak} obtained from the triaxial test. From this result, it can be confirmed that the difference between the calculated value and the experimental value is about 10%. Therefore, the strength can be evaluated appropriately by the proposed formula. However, regarding the blue dots in Fig. 6, when the non-compliant material was under saturated conditions, the difference between the calculated value and the experimental value was large. From this, when using this formula for highly saturated soil, we have to consider the additional degree of the compaction. The specific restoration method using this formula is described in chapter 4.

3.2 Construction test

(1) Overview of construction test

In this section, a construction tests using a small soil tank were conducted to confirm the strength and rigidity exhibited when an embankment is compacted with a compaction machine such as a vibrating roller as in an implementation work. In the construction test, we focused on two effects: the effect of the difference in the degree of compaction on the strength and rigidity (Tabele 4), and the effect of the dehydration of lime on the strength and rigidity as a response to the collapsed soil with high water content (Tabele 5).

The construction test was carried out by constructing an embankment in the small soil tank (4.5 m × 4.0 m) shown in Fig. 7. The finished thickness of each layer of the embankment was 30 cm, and 4 layers were constructed in total so that the height of the embankment was 1.2 m. In the construction test, two types of soil materials were used: *Inagi* sand (a group B material) and *Arakida* (a group C material). Regarding a water content at the time of embankment construction, the construction was started after adjusting a water content with the goal of the optimum water content obtained from a soil compaction test by the B-method ($1.0E_c$) or E-method ($4.5E_c$).

In addition, for the construction management of the embankment, three items (degree of compaction D_c, K_{30}-value, and settlement at the time of roller compaction) were measured with an RI instrument (a device for measuring the degree of compaction by radio isotope method), small FWD, and leveling. The embankment was compacted with compaction machines such as a vibrating roller or a plate compactor until the construction management conditions of each study case were met. The measurements with RI instrument and small FWD were conducted at 4 points per layer, and the measurements for settlement at the time of roller compaction were con-
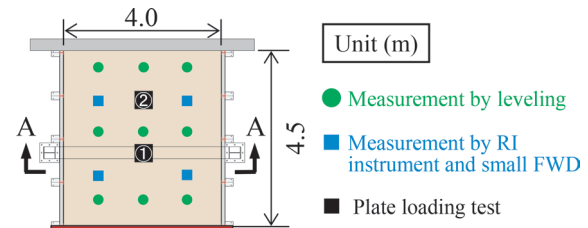

Fig. 7 Plan view of construction test (Height = 1.2 m)

ducted at 9 points per layer. Furthermore, after constructing four layers of the embankment, plate loading tests using a plate with a diameter of 30 cm were conducted at two points.

(2) Examination of differences in degree of compaction (Examination A)

In order to examine the effect of the difference in the degree of compaction on the strength and rigidity of the embankment, construction tests were conducted in two cases where the soil material and construction management conditions were changed, as shown in Table 4. The strength and rigidity of the embankment were confirmed by the K_{30}-value obtained from small FWD tests and the ultimate bearing capacity obtained from Plate loading tests. Here, the K_{30}-value is the coefficient of subgrade reaction when the strain level is around 0.1% of the loading plate diameter (the loading plate diameter is 30 cm), and the K_{30}-value is a value related to the rigidity of the ground. Regarding the ultimate bearing capacity, if there is a point on a load-settlement curve where settlement increases linearly or settlement increases sharply, the load at that point is taken as the ultimate bearing capacity. If there is no such point, the load at 10% of the loading plate diameter is taken as the ultimate bearing capacity. The ultimate bearing capacity is a value obtained by the above method and is a value related to the strength of the ground.

In the triaxial compression tests in the previous section, *Arakida* (group C material) compacted with D_c = 95% (E-method) exhibited about the same or higher strength as *Inagi* sand (group B material) compacted according to the regulations of performance rank II. Based on the result, the compaction condition of *Arakida* set to D_c = 95% (E-method) in this construction test. Figure 8 shows the relationship between the K_{30}-value by small FWD tests and the degree of compaction D_c with an RI instrument, and Fig. 9 shows the load-settlement curve in the plate loading tests. Here, the coefficient of subgrade reaction K_{30}-value uses the average value of four points

Table 4 Construction management conditions (Examination A)

Case	Materials	Construction management conditions	Optimum water content
CaseA1[*Inagi*_D_{cB}90]	Group B (*Inagi* sand)	$D_c \geq 90\%$ (B-method) and $K_{30} \geq 70$ MN/m³	16.8%
CaseA2[*Arakida*_D_{cE}95]	Group C (*Arakida*)	$D_c \geq 95\%$ (E-method)	15.5%

※ In addition to the conditions of the above table, it was confirmed that the settlement at the time of roller compaction had converged.

Table 5 Construction management conditions (Examination B)

Case	Materials	Construction management conditions
CaseB1[*Inagi*_D_{cB}90]	Group B (*Inagi* sand)	$D_c \geq 90\%$ (B-method) and $K_{30} \geq 70$ MN/m³
CaseB2[*Inagi*_improved_D_{cB}95]	Group B (*Inagi* sand)	$D_c \geq 95\%$ (B-method) (※1)
CaseB3[*Arakida*_improved_D_{cE}95]	Group C (*Arakida*)	$D_c \geq 95\%$ (E-method) (※1)

※1 They were constructed after dehydration with lime.
※2 In addition to the conditions of the above table, it was confirmed that the settlement at the time of roller compaction had converged.
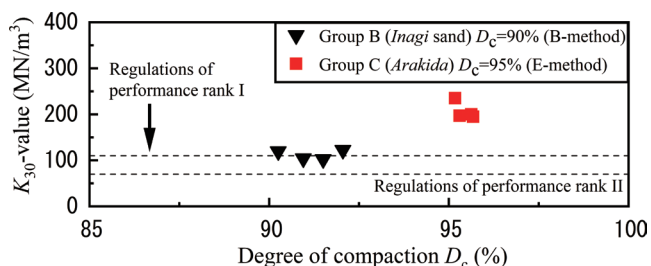
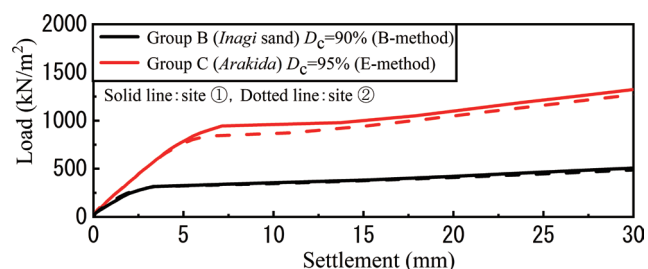Fig. 8 Relationship between K_{30}-value and D_c (Examination A)

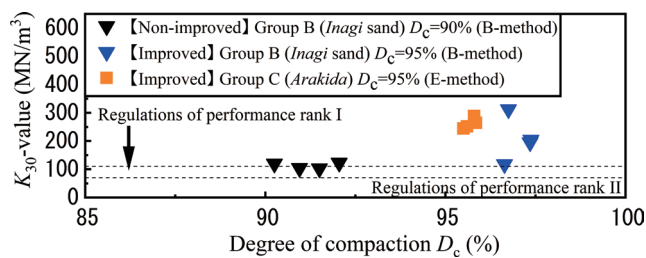Fig. 9 Load-settlement curve in plate loading tests (Examination A)

Fig. 10 Relationship between K_{30}-value and D_c (Examination B)

Fig. 11 Load-settlement curve in Plate loading tests (Examination B)

Fig. 12 Proposed restoration flow

and represents the average K_{30}-value of each layer.

Figure 8 shows that even group C materials meet the K_{30}-value regulatory requirement for level I performance (upper embankment) when sufficiently compacted, as in Case A2 [*Arakida_D_{cE95}*]. Furthermore, Fig. 9 shows that the bearing capacity of Case A2 [*Arakida_D_{cE95}*] exceeded the bearing capacity of Case A1 [*Inagi_D_{cB90}*] compacted according to the regulations of performance rank II (upper embankment).

(3) Examination of dehydrating effect of lime (Examination B)

In order to examine the dehydrating effect of lime, as shown in Table 5, the strength and rigidity were compared between the *Inagi* sand (Group B material) compacted according to level II performance requirements and the soil material after dehydration of soil with high water content (*Inagi* formation and *Arakida*) by lime. In the construction test, in order to simulate the high water content, water is first added and then lime is added. As for *Inagi* sand which is sandy soil and has a relatively low liquid limit, the target water content at water addition is $w = 35\%$. On the other hand, as for *Arakida* which is cohesive soil and has a relatively high liquid limit, the target water content at water addition is $w = 40\%$. The lime addition rate (ratio of lime mass to dry mass of soil) is based on the theoretical formula [2] obtained from the reaction formula of lime and water, where the target water content for dehydrating is the optimum water content of soil before lime addition. Specifically, in this construction test, the lime addition rate was 15% for *Inagi* sand and 20% for *Arakida*.

Figure 10 shows the relationship between the K_{30}-value by small FWD tests and the degree of compaction D_c with a RI instrument, and Fig. 11 shows the load-settlement curve by Plate loading tests. Fig. 10 and Fig. 11 show that the K_{30}-values and the ultimate bearing capacity of both Case B2 [*Inagi*-improved_D_{cB95}] and Case B3 [*Arakida*-improved_D_{cE95}] exceeded Case B1 [*Inagi_D_{cB90}*] which satisfies the regulatory requirements for Level II performance (upper embankment). For Case B2 [*Inagi*-improved_D_{cB95}] in Fig. 10, the K_{30}-value for only one layer shows a very large value
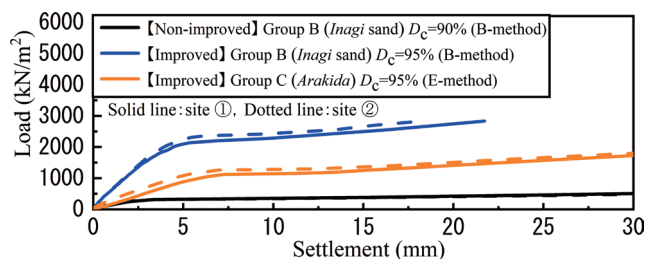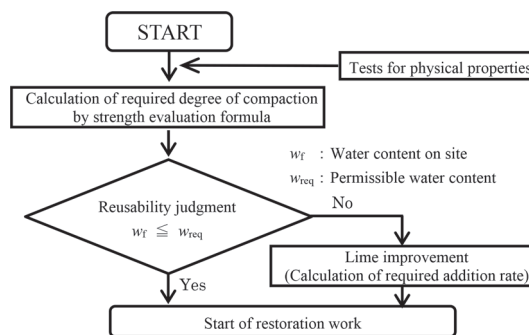
(312 MN/m³). This is because while the other layers took an average of 2 days from sprinkling to the completion of compaction, this layer required 8 days due to the construction schedule. In other words, it is considered that the chemical reaction between lime and soil is enhanced as time goes by, and strength and rigidity increase.

From the construction test results, it is considered that even soil from group B and C with a high water content may be able to exhibit strength and rigidity that satisfy level II performance, if sufficiently compacted after dehydration with lime.

4. Proposal of restoration method reusing soil from collapsed embankments

In this chapter, on the basis of the triaxial compression tests and construction tests, we propose a restoration method which reuses soil from collapsed embankments. Figure 12 shows the proposed restoration flow when an embankment collapses. At first, a physical test of the collapsed soil is carried out to confirm the soil particle density, grain size distribution, water content, compaction characteristics, and so on.

Secondly, according to the group classification determined from the grain size distribution, the required degree of compaction for the necessary strength is calculated using the strength evaluation

formula shown in Section 3.1. If the collapsed soil is a compliant material, the required degree of compaction can be determined according to Earth structure standard.

Thirdly, the judgement of whether it can be reused is conducted according to the water content of the collapsed soil. Specifically, we confirm the magnitude relationship between w_f (the water content of the collapsed soil measured on site) and w_{req} (the permissible water content) (Fig. 13), and Lime improvement is conducted if w_f is larger than w_{req}. Here, the guideline for w_{req} is the water content which indicates the intersection of the compaction curve and the required degree of compaction. As the result of the judgment of whether it can be reused, if Lime improvement is necessary, a lime addition rate is calculated using the theoretical formula obtained from the chemical reaction formula of lime and water shown in Fig. 14, and the improvement is implemented. After the Lime improvement, a compaction test is conducted again, and an embankment is constructed with a degree of compaction $D_c = 95\%$ with respect to the maximum dry density after improvement. On the other hand, as the result of the judgment of whether it can be reused, if Lime improvement isn't necessary, an embankment is compacted to reach the required degree of compaction described above. As a result, it is possible to restore an embankment reusing soil after it has collapsed.

5. Verification of proposed method

5.1 Overview of verification test

In order to verify the proposed restoration method, repeated load tests simulating a train load were conducted. The loading tests were carried out by constructing an upper embankment and a track section in a non-drained shear pit (width 2 m × depth 2 m × depth 3 m) (Fig. 15). In the load tests, after constructing a track with a roadbed, the PC sleeper model (1900 mm × 220 mm × 149.5 mm) was repeatedly loaded in the vertical direction. The number of loadings was 2 million times in all cases, and the number of loadings per day was 200,000 times (250,000 times only on the first day). The loads were equivalent to EA-17, and the load sharing ratio of one sleeper was determined as about 40% of the axle load with reference to previous research.
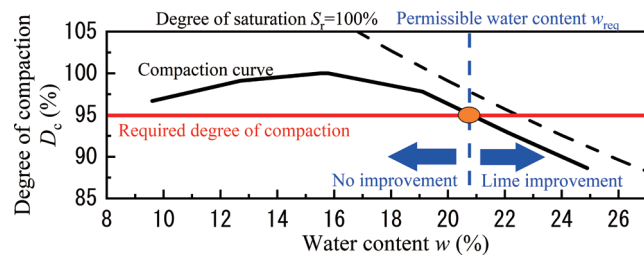
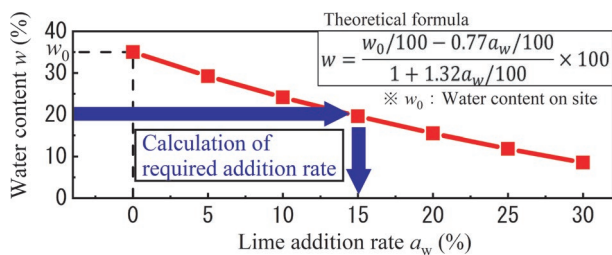**Fig. 13 Concept of permissible water content**

Fig. 14 Calculation of required addition rate

After 1 million loadings, water was added from the surface of the roadbed every 200,000 loadings to confirm the decrease in rigidity when the degree of saturation increased. For the amount of added water, the standard rainfall was determined as 120 L with reference to the concept of rainfall action specified in Earth structure standard in the design of drainage works. Then, while observing the saturation situation, 120 L was added on the first day of watering, 240 L was added on the second and third day, and 360 L was added on the 4th and 5th day.

5.2 Model specifications

The test conditions are shown in Table 6. As for case C1, *Inagi* sand (group B material) was constructed with a degree of compaction $D_c = 90\%$ (B-method) according to the regulations of level II performance stipulated in the current Earth structure standard. As for case C2, *Arakida* (group C material) which is a non-compliant material, was constructed with the degree of compaction $D_c = 90\%$ (E-method). In case C2, M-40 with a thickness of 60 cm was installed as a roadbed protection layer in order to reduce or prevent the decrease in roadbed rigidity and mud formation caused by heavy rain. In addition, case C3 was the case where the roadbed protection layer was not installed in Case C2.

The construction of the embankment was controlled by the degree of compaction with a RI instrument and the K_{30}-value by small FWD tests at every 30 cm layer thickness. For the measurement during loading, displacement gauges were installed at both ends of the sleepers to measure the amount of settlement, and the amount of
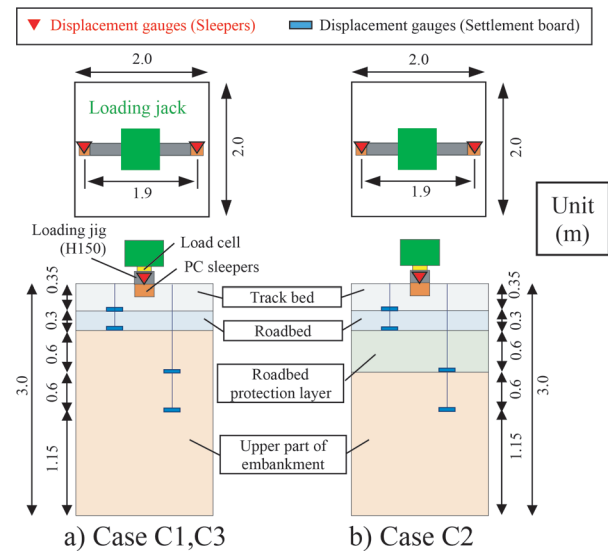
Fig. 15 Model specifications (Top: plan view, bottom: cross section)

Table 6 Test conditions for repeated load test

Case	Upper part of embankment	Roadbed protection layer	Roadbed※	Track bed
Case C1	*Inagi* sand (Group B) $D_c=90\%$ (B-method) $K_{30}\geqq 70$ MN/m³	—	C40 $D_c=95\%$ (E-method) $K_{30}\geqq 110$ MN/m³	Ballast $D_c=98\%$ (E-method) $K_{30}\geqq 110$ MN/m³
Case C2	*Arakida* (Group C) $D_c=90\%$ (E-method) $K_{30}\geqq 110$ MN/m³	M40 $D_c=95\%$ (E-method) $K_{30}\geqq 110$ MN/m³		
Case C3	*Arakida* (Group C) $D_c=90\%$ (E-method) $K_{30}\geqq 110$ MN/m³	—		

※ Water content was set to optimum water content

settlement in the underground was measured using a settlement plate.

5.3 Results of experiment

Figure 16 shows the amount of sleeper settlement due to loading and the settlement rate of the roadbed. The amount of sleeper settlement is calculated by averaging the measured values of the displacement meters on both sides of the sleepers for the displacement increment during dynamic loading. The settlement rate of the roadbed is calculated by normalizing the amount of settlement of the settlement plate installed at the top of the roadbed by the thickness of the roadbed (excluding the roadbed protection layer). Figure 16 shows that the sleeper settlement of Cases C1 and C2 presents almost the same cumulative deformation even after rainfall and watering. On the other hand, in Case C3, the amount of settlement is small up 1 million load cycles, but the amount of settlement increased significantly due to added water, and the amount of settlement at 2 million times of loading is larger than the other two cases.

The results of this experiment confirm that even non-compliant materials can exhibit almost the same load-bearing performance as compliant materials by using the proposed restoration method. However, if there is no roadbed protection layer, the amount of settlement during rainfall tends to be large. Therefore, it is considered necessary to install an appropriate roadbed protection layer when using non-compliant materials.

6. Conclusion

We conducted triaxial compression tests and construction tests using various materials, and proposed a new restoration method re-using soil from collapsed embankments. Furthermore, repeated loading tests simulating a train load were conducted, and we confirmed that even non-compliant materials can exhibit almost the same load-bearing performance as compliant materials by using the proposed restoration method.

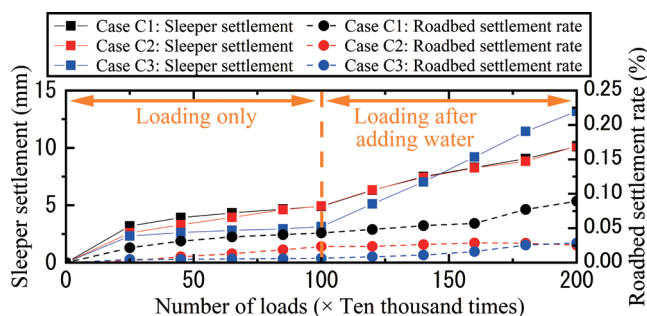Although this proposed method has never been used in actual

Fig. 16 Cumulative trend of sleeper settlement and roadbed settlement rate

restoration yet, by using this method, it is not necessary to dispose of soil from a collapsed embankment and purchase / transport new soil. This method should therefore make it possible to reduce the costs of restoration, and shorten the time required for reconstruction. This research was funded by railway technology development subsidy of Ministry of Land, Infrastructure, Transport and Tourism.

References

[1] Supervised by Ministry of Land, Infrastructure, Transport and Tourism, Edited by Railway Technical Research Institute, *Design Standards for Railway Structures and Commentary (Earth structure)*, Maruzen Publishing Co. Ltd 2007 (in Japanese).

[2] Japan Lime Association, *Ground Improvement Manual with Lime*, 7th Edition, Hokkosha, February, p. 17, 2016 (in Japanese).

[3] Fumio Tatsuoka et al., *Geotechnical Engineering / Technical Note*, Embankment Compaction 1 to 20 times, Foundation Works, July 2013-February 2015, 2013-2015 (in Japanese).

[4] Goro Kubota, "Soil test result collection, railway business research material," Vol. 5, No. 6, railway business research material, 1948 (in Japanese).
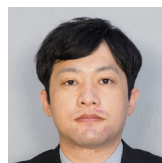
Authors

Kohei KASAHARA
Assistant Senior Researcher, Foundation & Geotechnical Engineering Laboratory, Structures Technology Division
Research Areas: Geotechnical Engineering

Tatsuki FUJIMOTO
Assistant Senior Researcher, Foundation & Geotechnical Engineering Laboratory, Structures Technology Division (Former)
Research Areas: Geotechnical Engineering

Susumu NAKAJIMA, Ph.D.
Senior Chief Researcher, Foundation & Geotechnical Engineering Laboratory, Structures Technology Division
Research Areas: Geotechnical Engineering

Yoshitaka TOMIDA
Researcher, Foundation & Geotechnical Engineering Laboratory, Structures Technology Division
Research Areas: Geotechnical Engineering

Development of High-speed Test Facility for Pantograph/OCL Systems

Tatsuya KOYAMA

Current Collection Laboratory, Railway Dynamics Division

The Railway Technical Research Institute (RTRI) has developed a new pantograph test facility, the "High-Speed Test Facility for Pantograph/OCL Systems," to develop pantographs for high-speed trains, wear resistant contact strips, and so on. This test facility mainly consists of four parts: a rotational disk with attached contact wire which can rotate at high speed up to 500 km/h, exciters which reproduce lateral arrangement and vertical movement of overhead contact lines (OCL), an energizing device which applies large current to a pantograph up to 1000 A, and environmental control devices which can control temperature from -20 to +40°C and humidity from 10% to 90% in test chamber. This paper shows the function, performance, and usage example of this test facility.

1. Introduction

Electric power to railway vehicles is generally supplied from overhead contact lines (OCL) via pantographs installed on the vehicle in electric railways. In order to supply stable power to vehicles, pantographs must meet the following performance requirements:

i)   Ability to maintain adherence with the OCL despite height fluctuations and vibrations;
ii) Sufficient energizing capacity;
iii) Wear resistance of sliding parts such as contact strips;
iv) Stable aerodynamic characteristics and low noise when running at high-speed.

There are several ways to evaluate this performances: (a) theoretical analysis, (b) computer simulation, (c) testing on a test bench, and (d) testing on commercial lines. Although (c) has limited testable conditions, (c) has the advantages such as

· evaluating current collection performance quantitatively compared with (a),
· evaluating complex phenomenon such as wear of contact strips, which is difficult to reproduce with (a) or (b),
· carrying out testing under conditions that cannot be achieved in (d), e.g., extremely high uplift force of the pantograph.

Therefore, RTRI has test facilities for evaluating the performance of pantographs. Among its conventional facilities was the "pantograph test equipment" (hereinafter, PTE) which could evaluate i) - iii). However, it could not be used to develop pantographs for higher speeds, e.g. the maximum peripheral speed which could be achieved with the PTE was 300 km/h which was lower than the maximum operating speed in Japan (320 km/h). Thus, RTRI developed a new test facility "High-speed Test Facility for Pantograph/OCL Systems (HiPaC)," which can evaluate the current collection performance of a pantograph for high-speed trains.

2. Functions and Performances of HiPaC

2.1 Configuration

Figure 1 shows the configuration of the HiPaC. HiPaC is installed on a ground floor and basement floor. The test chamber where various tests are carried out is on the basement floor and is covered with heat insulating material for maintain a constant temperature.
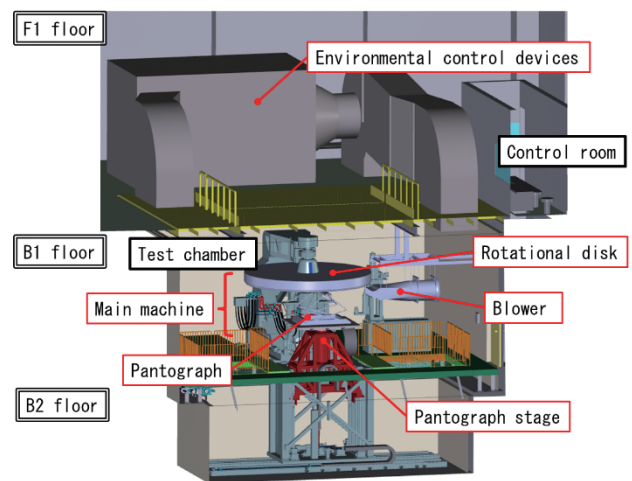

Fig. 1   Configuration of HiPaC

HiPaC consists of

· main machine simulating OCL,
· pantograph stage on which a pantograph is installed,
· an energizing device which supplies electricity to the pantograph,
· environmental control devices which control the temperature and humidity in the test chamber,
· a blower which simulates cooling effect to pantograph head by airflow while train running.

The main machine, the pantograph stage, and the blower are installed in the test chamber, and the environmental control devices and the energizing device are installed on the ground floor. In addition, the hydraulic system, which is the power source for the main machine and pantograph stage, is installed in the hydraulic room on the basement floor to suppress noise during the test.

2.2 Main function

Figure 2 shows the test chamber and function of main machine and pantograph stage such as the vibration direction. Table 1 shows the main specifications of HiPaC. For comparison with the PTE, the specifications of PTE are also shown in { } in table 1.

Compared with PTE, HiPaC has improved peripheral speed, vibration performance, and energization performance. Furthermore,
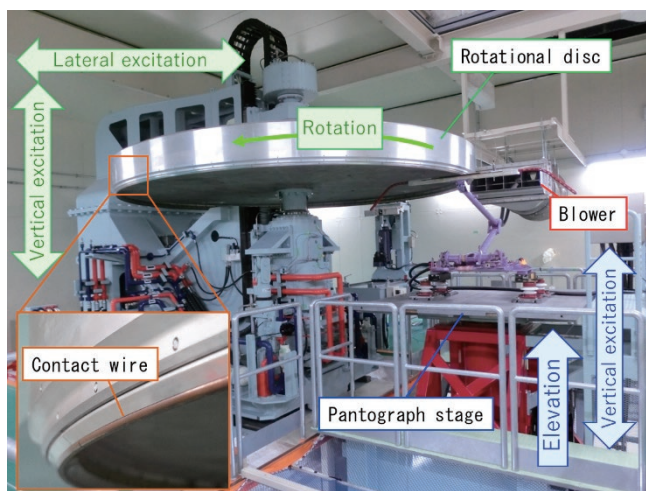
Fig. 2 Function of HiPaC

HiPaC has been equipped with environmental control devices and a blower as new functions.

2.2.1 Main machine

The main machine consists of a rotational disk, vertical direction exciter and lateral direction (direction perpendicular to the train running direction and the vertical direction) exciter. The rotational disk, the vertical direction exciter, and the lateral direction exciter are used to reproduce sliding between a pantograph and contact wire, vibration in vertical direction, and the stagger (arrangement in lateral direction) of the contact wire, respectively. An actual contact

Table 1 Main specification of HiPaC

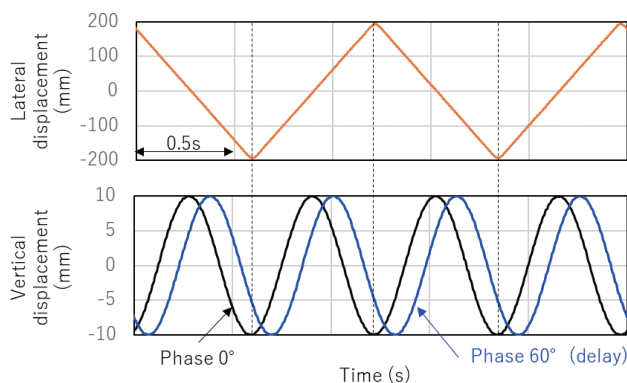| Device	Specification		
Main Machine	Peripheral speed	Max. 500 km/h {300 km/h}	
	Vertical vibration	Frequency	≤ 27.8 Hz {17 Hz}
		Amplitude	Max. 100 mm*1 {35 mm}
		Waveform	Sine wave or other*2 {Sine wave}
	Lateral vibration	Frequency	≤ 5 Hz {0.03 Hz}
		Amplitude	Max. 300 mm*1
		Waveform	Triangular wave, sine wave, or other*2 {Triangular wave}
Pantograph stage	Elevating amount	1600 mm	
	Vertical vibration	Frequency	≤ 10 Hz {Same}
		Amplitude	35 mm*1 {Same}
		Waveform	Sine wave or other*2 {Sine wave}
Environmental control device	Temperature	-20 to +40 degree (Celsius)*3 {None}	
	Humidity	10% to 90% {None}	
Blower	Wind speed	60 to 100 km/h {None}	
Energizing device	Type	AC or DC {Same}	
	Voltage	100 to 600 V {100 V}	
	Current	≤ 1000 A (10-step control) {≤ 400 A (4-step control)}	

* { } means specification of PTE
*1 Depends on the frequency.
*2 Can be vibrated with any waveform by inputting an external signal.
*3 When the main machine is active (controllable at -25 to +40 degree (Celsius) at a standstill)

wire can be installed on the rotational disk (Fig. 2).

The maximum speed of the disk is about 700 rpm (equivalent to train running speed of 500 km/h). Regarding the vibration performance in the vertical direction, the maximum frequency is 27.8 Hz, which corresponds to the arrival frequency of the dropper installed at intervals of 5 m when train running speed is 500 km/h, and the maximum amplitude is 100 mm (depending on the frequency). Regarding the vibration performance in the lateral direction, the maximum frequency is 5 Hz, which is larger than the arrival frequency of the supporting point of OCL of which span length is 50 m and cycle of stagger is a half cycle in a span when train running speed is 500 km/h. The maximum amplitude is 300 mm (depending on the frequency) which equals to stagger of OCL of Shinkansen (cf. stagger of OCL of conventional train is 250 mm in Japan).

The disk rotation and vertical/lateral vibration of the main machine can be controlled independently or integrally with each other. For example, to understand the pantograph compliance characteristics in the vertical direction, which is one of the indicators to evaluate the performance of pantograph, only vertical vibration is performed. On the other hand, when evaluating contact loss, disk rotation, vertical vibration, and lateral vibration are performed integrally. However, when vertical and lateral vibration are performed at same time, if each phase of vibration is different, it is impossible to perform reproducible tests. Therefore, HiPaC has a phase adjustment function. To match the actual behavior between the pantograph and the OCL when the train is running, the main machine makes the vertical position of the disk lowermost when the disk turns back laterally. On the other hand, it makes the vertical position of the disk uppermost when the disk exists at the midpoint in the lateral direction (black line in Fig. 3). The adjustment function can also delay or advance phase intentionally (blue line in Fig. 3).

Furthermore, in addition to the function described above, HiPaC has other two advanced features to control the rotational disk. One is a function to reproduce the behavior corresponding to the time-history waveforms created through simulation or acquired in a field test. The other is a function to excite the disk by a signal generated by an external device such as function generator and real-time simulator which is used in the hybrid simulation described later.

2.2.2 Pantograph stage

The pantograph stage is a device to set a pantograph, and consists of a vibration table, vertical vibration device, an elevating de-

Fig. 3 Vertical/horizontal vibration waveform of the disc (above: Lateral displacement waveform, below: Vertical displacement waveform)

vice, and a front-back moving device.

The size of the vibration table is 2 m in the longitudinal direction (train running direction) and 1.9 m in the lateral direction. Since many kinds of pantograph are used in Japan, bolt holes with a 150 mm pitch are provided on the upper surface of the table to install various pantographs. The vertical vibration device is used to reproduce the vertical vibration of train and its maximum frequency and amplitude is 10 Hz and 35mm, respectively. The elevating device is to adjust posture of pantograph and its elevating height is 1600 mm. The front-back moving device is used to adjust the longitudinal position of the pantograph head.

2.2.3 Energizing device

Energizing device supplies electricity to the pantograph and consists of a pulse width modulation (PWM) converter, an H-bridge chopper, and resistance units. This device can supply AC or DC electricity. Maximum voltage and current are 600 V and 1000 A, respectively. Figure 4 shows a photo of the energization test with disk rotation, vertical and lateral vibration. The light in Fig. 4 is an arc generated by contact loss.

When DC loading tests were carried out with the PTE, the PTE energizing device made DC current from single-phase AC and a full-wave rectifier circuit. Therefore, since the voltage became 0 V momentarily, the arc, which occurred when a pantograph lost contact with contact wire, disappeared immediately. On the other hand,

Fig. 4 Photo of energization test (light between disk and pantograph is an arc generated by contact loss)

○ Contact loss with arcing
   (so-called NQ or AQ in [1])
● Contact loss without arcing
   (so-called CQ in [1])
○ Sum of contact loss with and
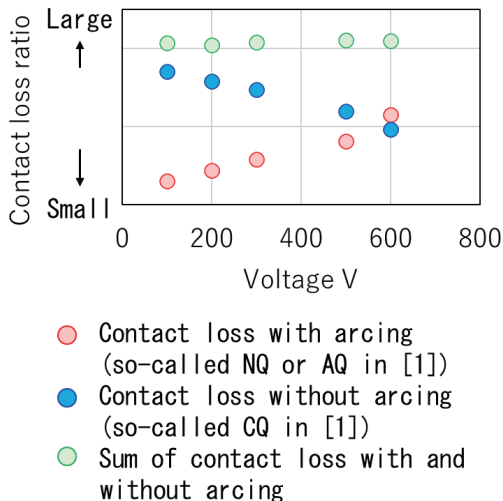   without arcing

Fig. 5 Contact loss ratio for each voltage

since HiPaC can supply accurate DC electricity with low ripple rate, which is less than 1%, it is possible to generate a longer lasting arc. In addition, the voltage, which was 100 V for PTE, has been improved to 600 V for HiPaC. Figure 5 shows the contact loss ratio when tests were carried out with different voltages with HiPaC. The testing conditions were as follows;

- Peripheral speed: 300 km/h
- Vertical vibration of the rotational disk:
    Frequency: 10 Hz, Amplitude: 10 mm
- Lateral vibration of the rotational disk:
    Frequency: 0.1 Hz, Amplitude: 200 mm
- Temperature and humidity in the test chamber: 15°C, 20%
- Energization: DC100 V-600 V, 100 A
- Wind velocity from the blower: 0 km/h

Green plots indicate the contact loss ratio calculated from contact loss time when the pantograph loses mechanical contact with contact wire. Red plots indicate the contact loss ratio calculated from the time when the arc was generated within the time when pantograph loses mechanical contact with the contact wire, which corresponds to NQ or AQ defined in [1]. Blue plots indicate the contact loss ratio calculated from the time when the arc disappears within the time when pantograph loses mechanical contact with the contact wire, which corresponds to CQ defined in [1]. Since the test conditions are the same except for the voltage in each test, green plots in Fig. 5 are constant regardless of the voltage. On the other hand, red plots increase as the voltage increases. This indicates that the arc was difficult to extinguish under high voltage conditions.

The resistance units (single unit 2 Ω or 6 Ω, 10 units in total) were used as the electrical load when energized test was performed. The energizing current could be adjusted in 10 steps by increasing or decreasing the number of resistance units connected in parallel. In addition, the maximum current was 1000 A, which was more than the current collected by a Shinkansen pantograph.

As described above, by increasing the voltage and current of the energizing device, it is possible to conduct tests under energization conditions that are closer to those of commercial lines, than with the PTE.

2.2.4 Environmental control devices

The environmental control devices consist of a heater, a refrigerator, a humidifier, and a dehumidifier.

The temperature can be controlled in the range of -20°C to + 40°C, when the main machine is operated. On the other hand, the temperature can be controlled in the range of -25°C to + 40°C, when the main machine is not operated. The latter range satisfies the temperature conditions specified in operating climatic tests (type test) in IEC 60494:2013 [2].

The humidity can be controlled in the range of 10% to 90%, when the temperature in the test chamber is higher than 10°C.

2.2.5 Blower

A blower simulates the cooling effect of the airflow on pantograph head while a train is running. The maximum wind speed is 100 km/h.

3. Usage example of HiPaC

It is possible to evaluate the performance of current collection of a pantograph, such as compliance characteristics in the vertical

direction, and contact loss ratio by using HiPaC. In addition, it is now also possible to carry out the following tests as the functions have been improved and expanded, compared with the PTE.

3.1 Evaluation test of wear resistance of contact strips

It has been reported that the amount of wear of the contact strips changes depending on the running speed and lateral movement speed of the contact wire [3, 4]. In addition, temperature is also important to evaluate wear resistance of contact strips [5]. As mentioned above, HiPaC has many functions to perform tests similar to various condition on commercial line, e.g. high voltage, large current, airflow around pantograph, and lateral movement of the contact wire. Table 2 shows the mean temperature of the lower surface of the contact strips at the center of the pantograph head and a point 200 mm away from the center of the pantograph head, when the frequency of the lateral vibration with constant amplitude, and velocity of airflow from the blower were changed. The test conditions were as follows:

- Peripheral speed: 300 km/h
- Vertical vibration of the rotational disk: disuse
- Lateral vibration of the rotational disk:
    Frequency: 0.1 Hz or 1.0 Hz
    Amplitude: 200 mm
- Temperature and humidity in the test chamber: 15°C, 20%
- Energization: AC100 V, 400 A
- Wind velocity from the blower: 0 km/h or 100 km/h

Table 2   Mean temperature on lower surface of contact strips

Test case	Frequency of lateral vibration Hz	Velocity of airflow km/h	Mean temperature °C	
			center	200 mm
Case 1	0.1	0	113	75
Case 2		100	72	45
Case 3	1.0	0	114	96
Case 4		100	80	64

Case 1 is similar test condition on PTE, and Case 4 is similar test condition to commercial train. It is confirmed that the speed of lateral movement and the airflow affect temperature of contact strips, in other words wear of contact strips. Therefore, it is considered that the wear of the contact strips on the commercial line can be reproduced more accurately than with the PTE.
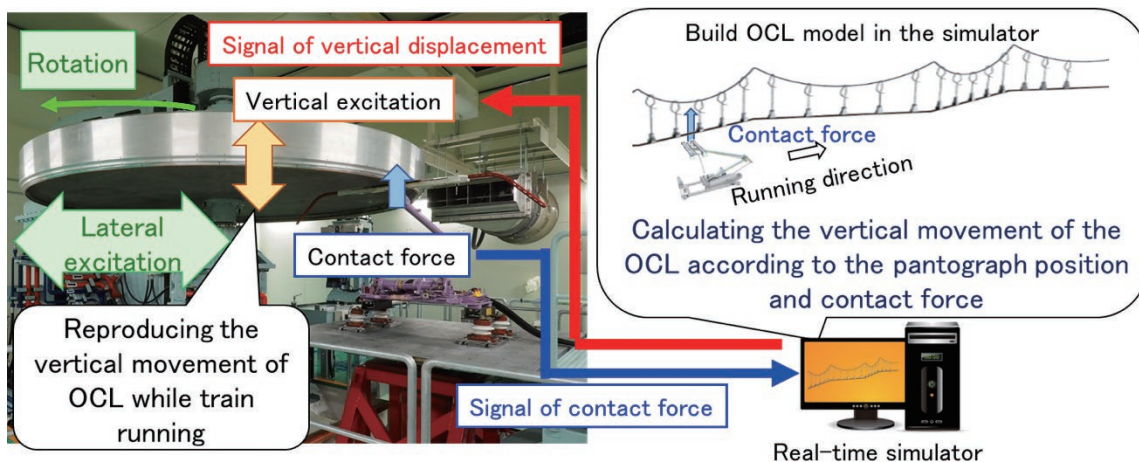
3.2 Hybrid simulation

In order to reproduce dynamic interaction between pantograph and OCL, a hybrid simulation (HS) with an exciter has been developed [6, 7]. If HS can be applied to HiPaC, we can carry out HS test considering not only vertical and lateral vibration but also sliding. Figure 6 shows schematic drawing of hybrid simulation of pantograph and OCL systems on HiPaC. A pantograph with sensors to measure contact force between the pantograph and the rotational disk, and the real-time simulator which calculates the behavior of the OCL were used to carry out HS on HiPaC. An example of the procedure for carrying out HS is as follows:
(1) Signals required for estimation of contact force are sent to the real-time simulator.
(2) The real-time simulator calculates the contact force and the behavior of the OCL according to the contact force and pantograph location.
(3) The real-time simulator sends signals of the vertical displacement of the contact wire at the contact point between pantograph and contact wire as the vertical displacement of rotational disk to the HiPaC controller.
(4) The controller moves the rotational disk to the calculated position.
To realize HS, not only is a high-speed real-time simulator required, the vertical exciters must also be highly responsive. We consider that HiPaC has sufficient responsiveness to perform HS. Currently, we are developing HS system on HiPaC [8]. In future, it will be possible to evaluate the current collection performance of a pantograph and the wear of the contact strips considering OCL response.

4. Conclusion

RTRI has developed a new pantograph test facility, the "High-Speed Test Facility for Pantograph/OCL Systems," which has the

Fig. 6   Schematic drawing of hybrid simulation of pantograph and OCL systems

functions to reproduce:

- sliding between contact wire and contact strips at high speed, up to 500 km/h,
- vertical vibration of contact lines,
- the stagger of the contact wire,
- the vertical vibration of train,
- energization during train running,
- environment condition (temperature and humidity) on commercial line,
- and the cooling effect of the airflow on pantograph head.

We will use this facility to develop pantographs for highspeed lines and contact strips with improved wear resistance.

References

[1] The International Electrotechnical Commission, "*Railway applications - Current collection systems - Technical criteria for the interaction between pantograph and overhead contact line (to achieve free access) IEC 62486: 2017*," 2017.

[2] The International Electrotechnical Commission, "*Railway applications - Rolling stock – Pantographs - Characteristics and tests - Part 1: Pantographs for main line vehicles IEC 60494-1: 2013*," 2013.

[3] Nemoto, K., Kubota, Y., "Effect of sliding speed on friction and wear between copper alloy contact wire and iron-based sintered alloy contact strip," presented at *the 26th Jointed Railway Technology Symposium (J-RAIL 2019)*, Tokyo, Japan, December 4-6, 2019, Paper S7-4-2 (in Japanese).

[4] Morimoto, F., Kubota, Y., "Influence of the lateral movement speed of the contact wire on the wear of the pantograph contact strip," presented at *the 25th Jointed Railway Technology Symposium (J-RAIL 2018)*, Tokyo, Japan, December 5-7, 2018, Paper 1312 (in Japanese).

[5] Yamashita, C., "Wear mechanism of Current Collection Materials under the Effect of Flowing Electric Current," *Quarterly Report of RTRI*, Vol. 58, No. 4, pp. 264-269, 2017.

[6] Pombo, J., Antunes, P., Rebelo, J., Santos, J., Magalhaes, H., Ambrosio, J., "Recent Developments in Pantograph-Catenary Interaction Technology Development and De-Risk Electrification Projects," Presented at *the 9th International Symposium on Speed-up and sustainable Technology for Railway and Maglev Systems (STECH 2021)*, Chiba, Japan, November 23-25, 2021, Paper IL-3.

[7] Kobayashi, S., Yamashita, Y., Usuda, T., Stoten, D. P., "Hybrid Simulation Testing of a Pantograph-Catenary System Using a Dynamically Substructured System Framework and a MDOF Catenary Model," *Quarterly Report of RTRI*, Vol. 61, No. 2, pp. 127-132, 2020.

[8] Kobayashi, S., Koyama, T., Harada, S., "Hybrid Simulation Based on High-Speed Test Facility for Pantograph/OCL Systems," *RTRI Report*, Vol. 35, No. 12, pp. 47-52, 2021 (in Japanese).

Author

Tatsuya KOYAMA
Senior Researcher, Current Collection
Laboratory, Railway Dynamics Division
Research Areas: Dynamic Interaction
between Pantograph and Catenary

Development and Validation of Drive-by Detection Method for Resonant Bridges

Kodai MATSUOKA
Structural Mechanics Laboratory, Railway Dynamics Division

Kyohei KAWASAKI
Kyushu Railway Company

Hirofumi TANAKA
Track Geometry and Maintenance Laboratory, Track Technology Division

Mizuki TSUNEMOTO
Contact Line Structures Laboratory, Power Supply Technology Division

Resonance in high-speed railway bridges is one of the sources of concern for ride comfort and catenary damage. In severe cases, countermeasures are required. However, detecting resonance requires a vast number of on-site measurements. This study develops a drive-by method for detecting resonant bridges as a train is running. The proposed method consists of signal processing for extracting vibration components specific to resonant bridges and a process of identifying differences between the lead and last vehicles. Results from a practical application of this method confirmed that it was possible to extract resonant bridges and the resonant states of the extracted bridges were confirmed by on-site measurement.

Key words: *drive-by inspection, high-speed railway, resonance, bridge*

1. Introduction

In order to efficiently manage a vast number of railway structures with minimum necessary maintenance, structural health monitoring that understands the state of the structures with sensors has been proposed and introduced, and relating methods, equipment, and practical applications have been widely studied [1]. In recent years, a method for indirectly evaluating the structural performance of bridges using sensors installed on traveling vehicles has been studied, as a more economical and efficient monitoring method, especially for bridges [2]. The authors of this paper have also (developed) studied a method for detecting the resonance of bridges from data measured on traveling vehicles, which is important in the maintenance of high-speed railway bridges themselves and equipment installed on them [3]. In the existing method, the amplitude ratio of vertical car body accelerations measured in the first and last vehicles was used, however there was a problem that the accuracy decreased when the amplitude of the first vehicle was small. In this study, the authors improved the method to allow more accurate detection using the theoretical features of the resonant bridge and verified it on an actual railway.

Before introducing the proposed drive-by detection method, the resonance phenomenon in high-speed railway bridges is explained briefly. Resonance of a bridge occurs when the excitation frequency due to the regular wheelset arrangement of a train traveling on the bridge is close to the natural frequency of the bridge [4]. Figure 1 shows an example of the calculation of the vertical displacement at the center of the bridge supports when a 12-car train passes through a bridge with a 50 m span length and a frequency of 2.8 Hz at various speeds. In this example, at a train speed of 250 km/h, resonance occurs where the displacement of the bridge increases as the vehicle passes. In recent years, the excitation frequency of trains and the natural frequency of bridges tend to be close to each other due to the rapid increase in train speed, existence of long spans and low-stiffness bridges. Based on this, a design system that can consider the bridge resonance has already been established, so the resonance phenomenon itself is rarely a problem for bridges. However, in some high-speed railways, the vibrations caused by
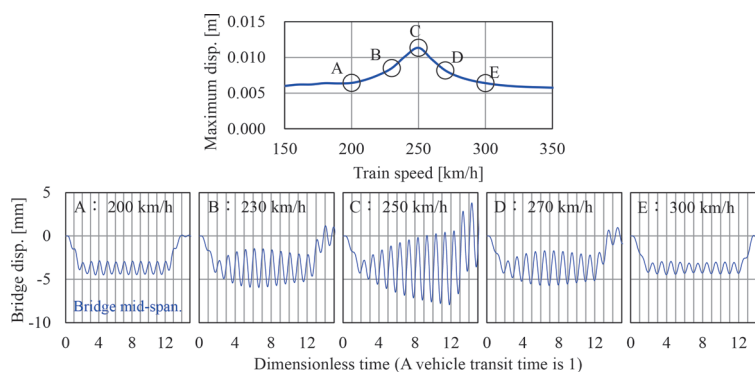
Fig. 1 Calculation examples of high-speed railway bridge resonance (span length 50 m, bridge frequency 2.8 Hz, 12-car train)

resonance affects ride quality, and in serious cases, countermeasures may be required [5]. In addition, there may be concerns about the impact on overhead catenary equipment such as poles and overhead lines on resonant bridges. Therefore, it is desirable to detect these appropriately [6]. However, extracting resonant bridges is extremely labor intensive, because bridge deflection measurements on the ground are necessary under train passages. To save the labor of in-situ measurements and manage resonant bridges more efficiently, this research developed a resonant bridge detection method using data measured on traveling vehicles.

2. Resonant bridge detection method

2.1 Waveform peculiar to resonant bridge

To clarify the vibration components peculiar to a resonant bridge among displacements and vibrations input to vehicles, consider the theoretical model shown in Fig. 2. Here, for simplicity, four adjacent axles near the coupler between vehicles are modeled as one concentrated load. The bridge is a simple supported beam with natural frequency n (Hz) and span length L_b (m), and the vertical displacement at horizontal position x (m) and time t (s) is expressed as $z_b(x, t)$. Assuming that a train speed is v (m/s) and a vehicle length per car is L_c (m), the main excitation frequency is v/L_c (Hz). Considering that resonance occurs when v/L_c matches the bridge natural frequency n, resonance train speed v_{res} is expressed by the following (1).

$$v_{res} = n \cdot L_c \qquad (1)$$

Here, assuming that the traveling speed is the resonance speed, and the bridge is in a steady state. The displacement of the bridge at the position of the load P newly passing through the bridge in this state are focused. Let t_p be the elapsed time since this concentrated load entered the beam and let x_p be the concentrated load acting position at that time. The following (2) can be obtained from (1).

$$n = \frac{v_{res}}{L_c} = \frac{x_p}{L_c \cdot t_p} \qquad (2)$$

$(0 < x_p \leq L_b)$

On the other hand, the displacement $z_b(x, t)$ is composed of the quasi-static response component $z_{b,s}$ generated corresponding to the moving load position and the dynamic response component $z_{b,d}$ caused by the Eigen vibration of the beam as shown in (3).

$$z_b(x, t) = z_{b,s}(x, t) + z_{b,d}(x, t) \qquad (3)$$

Of these, the quasi-static response components $z_{b,s}$ are removed by difference processing as described later. Therefore, the dynamic response components $z_{b,d}$ are focused here. Equation (4) is obtained by decomposing the dynamic response components $z_{b,d}$ into functions of position and time by modal decomposition, and then considering only the primary deflection mode, which is the main component of the resonant bridge.

$$z_{b,d}(x, t) \approx \xi_{1,d}(t) \sin\left(\frac{\pi x}{L_b}\right) \qquad (4)$$

Also, from the assumption of steady state, the modal displacements $\xi_{1,d}$ can be expressed by (5).

$$\xi_{1,d}(t) = A_{res} \sin(2\pi n t + \theta_{res}) \qquad (5)$$

A_{res} is the dynamic response amplitude of the beam at resonance. In addition, $\theta_{res} = \pi(1 - L_b/L_c)$ because the phases of the displacement response and the exciting force shift by $\pi/2$ in the resonance state.

Here, if (5) is substituted into (4) and converted to time $t = t_0 = x_p/(L_c n)$ by (2) in the domain $0 < x_p < L_b$, the dynamic response components $z_{b,d}(x_p)$ of the beam at the load position x_p traveling through the resonant beam are given by (6) in the domain $0 < x_p < L_b$.

$$z_{b,d}(x_p)$$
$$\approx A_{res} \sin\left(2\pi \frac{x_p}{L_c} + \theta_{res}\right) \sin\left(2\pi \frac{x_p}{2L_b}\right) \qquad (6)$$

$(0 < x_p \leq L_b)$

From (6), the displacement of the bridge measured at the load position of the vehicle passing through the resonant bridge is the multiplication of a wave with a wavelength equal to the vehicle length L_c and a wave with a wavelength equal to twice the bridge span length ($2L_b$). Figure 3 and Fig. 4 show the waveform and spectrum of the dynamic response component of the resonant bridge at the load position calculated by (6) when the span length is 50 m and the vehicle length is 25 m. The theoretical waveform (solid line) shows the characteristic that the maximum amplitude of the wave corresponding to the vehicle length (black dotted line) increases or decreases according to the semi-sine wave (blue dashed line: span length component) corresponding to the span length. In addition, it can be seen from Fig. 4 that the dynamic bridge response component of the load position is mainly composed of the vehicle length component corresponding to the Eigen vibration of the bridge.

Resonant bridges can be detected by extracting the waveform
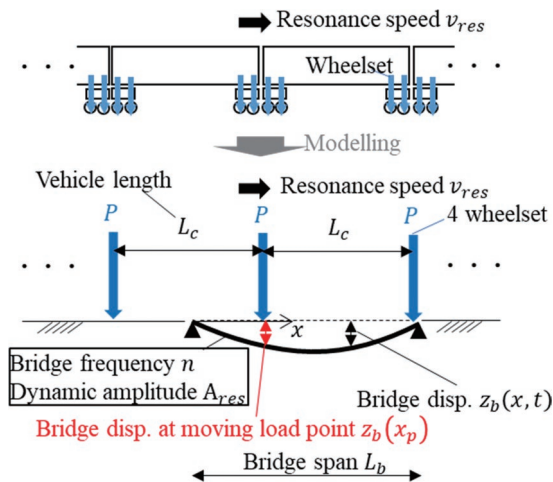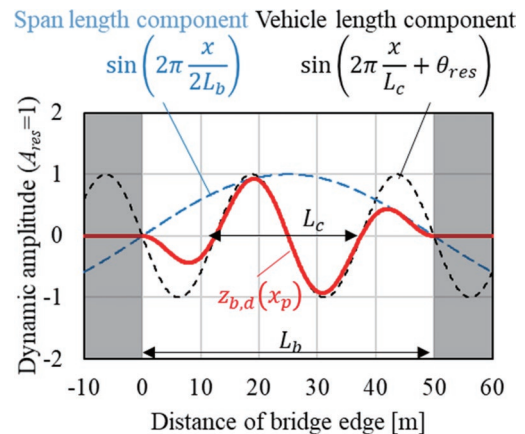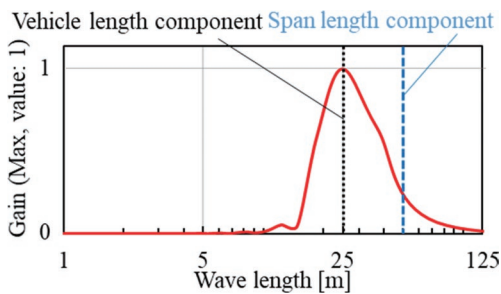

Fig. 2 Resonant bridge model for theoretical analysis

Fig. 3 Theoretical calculated resonant bridge dynamic response at moving load point (span length 50 m)

Fig. 4 Spectrum of resonant bridge dynamic response at moving load point (span length 50 m)

peculiar to the resonant bridge shown above from the track vertical displacement (hereinafter, track displacement) and the car body vertical acceleration (hereinafter, vehicle body acceleration) measured by sensors on the vehicles. When measuring track displacement, the components peculiar to the above resonance bridge are directly observed. In the case of vehicle body acceleration, it is affected by the springs and dampers of vehicles. However, the frequency of the waveform peculiar to the resonance bridge is more than approximately 2 Hz. This is a higher frequency than about 1 Hz, where the vehicle body vertical vibration mode exists in many high-speed railway vehicles. Therefore, the component in Fig. 3 introduced as track displacement is also observed as car body acceleration [7].

However, the drive-by measurement data contains various components such as rail irregularity and quasi-static response components of bridges, in addition to the components peculiar to the resonant bridge. The method of offsetting these effects and extracting the resonant bridge with higher accuracy is shown in the next section.

2.2 Extraction method from drive-by measurement data

This method consists of two processes: signal processing using filters and envelopes for track displacements or car body accelerations measured in the first and last vehicles, and subtraction processing of the measured waveforms of the first and last vehicles.

To emphasize the components peculiar to the resonant bridge in Fig. 3 from various components of the drive-by measured data, the signal processing consists of (1) bandpass filter processing with the wavelength near 25 m as a passing band, and (2) envelope processing to connect the peaks of the waveform. By (1), the components peculiar to the resonant bridge shown by the solid line in Fig. 3 are extracted from the drive-by measurement data containing various components. Next, from (2), the component corresponding to the bridge span length shown by the dashed line is estimated from the solid line in Fig. 3. The envelope processing (2) lengthens the wavelength of the extracted waveform and converts the evaluation index from wave domain to the amplitude domain. The longer wavelength can reduce the influence of the position synchronization error during the difference processing shown below.

Even if signal processing is performed, the 25 m wavelength component of the track displacement and the quasi-static deformation of the bridge may not be removed. Therefore, it cannot be determined whether the obtained peak is caused by resonance or not. Therefore, after performing the above processing on the two drive-by measurement data of the first and last vehicles, (3) the difference processing that subtracts the measured waveform of the first vehicle from the measured waveform of the last vehicle cancels out the
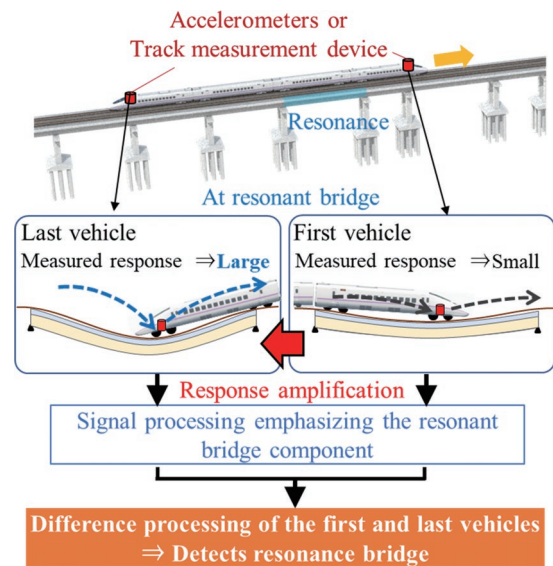
Fig. 5 Resonant bridge extraction flow

components other than the bridge resonance. This difference-processed waveform is called an envelope difference. Figure 5 shows the concept of resonant bridge component extraction by difference processing of the measured waveforms of the first and last vehicles. The dynamic response of the bridge grows as a train passes; however, the dynamic response is hardly excited when the first car passes. On the other hand, the quasi-static bridge deformation and the static track displacement do not change when the first and last vehicles pass. Therefore, by subtracting the measured waveform of the first vehicle from the measured waveform of the last vehicle, it is possible to cancel out the vibration components other than those caused by the bridge resonance, so that only the resonant bridge can be extracted with high accuracy.

More specifically, the resonant bridge is extracted from the drive-by measurement data assuming the following two conditions.
・There is a predominant component (peak) in the envelope difference
・Peak span roughly matches the length of the bridge span

The above-mentioned detection method for the resonant bridge has been implemented on the track maintenance management database system "LABOCS" [8]. LABOCS is a system that is widely used in track maintenance departments of railway operators in Japan. For example, this system can read track geometry data obtained from track geometry cars, perform the necessary signal processing with measured waveform, and display the processing waveform on a chart with ledger data of railway infrastructure. As a result, if there is a peak with the same span as the bridge span length in the envelope difference calculated by the proposed method by comparing with the bridge data prepared on LABOCS, the bridge can be extracted as a resonant bridge. In addition, since equipment data such as bridge spans already exists in LABOCS of each railway company in many cases, it is not necessary to build a new database when introducing this method.

3. Verification by numerical simulation

Here, the effectiveness of the proposed method was verified using a two-dimensional dynamic interaction simulation in which the vehicle was modeled as multi-body dynamics with 6 degrees of

freedom per car and the bridge was modeled as a simple support girder with 3 degrees of freedom up to the third-order bending mode. The simulation method can be found in references [9] and [10].

Figures 6 and 7 show the results of applying the method to track displacement and car body acceleration calculated by simulation for a bridge with a span length of 30 m and a natural frequency of 2.3 Hz. The train was an 8-car train, and the train speeds were 100, 180, 210, 240, and 300 km/h (A, B, C, D, and E, respectively). According to the sensor position in a commercial train, the acceleration on the floor just above the first bogie of the first car and the second bogie of the last car are used for the car body acceleration, and the displacement of the bridge directly below the center of the second bogie of the first car and the first bogie of the last car are used for the track displacement. The entrance point on the bridge for the drive-by sensor is set to 0 on the horizontal axis.

Figure 6 shows that only the track displacement corresponding to the last car increases at the time of resonance in Fig. C, and that the vibration component peculiar to resonance is extracted by the bandpass filter processing and the envelope processing. In addition, the difference processing between the first and the last cars forms a dominant component whose span is the span length. Therefore, it is considered that the resonant bridge can be detected on the condition of the presence or absence of the predominant component, the pre-

dominant span, and the bridge span length.

When the car body acceleration shown in Fig. 7 is used, almost the same tendency can be seen. However, it should be noted that a phase delay occurs due to the influence of the vehicle spring-damper system, and the position of the peak formed at the tail end at resonance shifts toward the end point of the bridge. From the above, the resonance bridge can be detected from the drive-by measurement data by the proposed method. In the numerical simulation, in addition to the above basic examples, the effects of bridge span length, bridge damping ratio, static track displacement, measurement noise, and the first and the last cars position synchronization error have been studied for Japanese high-speed railways. It has been confirmed that the proposed method can be applied with a span length of 20 m to 70 m in the track management state [4], [7].

4. Validation on the actual railway

4.1 Tested drive-by measurement data

To validate the effectiveness and practicality of the proposed method on an (actual) commercial railway, the proposed method was applied to car body accelerations and track displacement measured on vehicles of an actual high-speed railway, and resonant
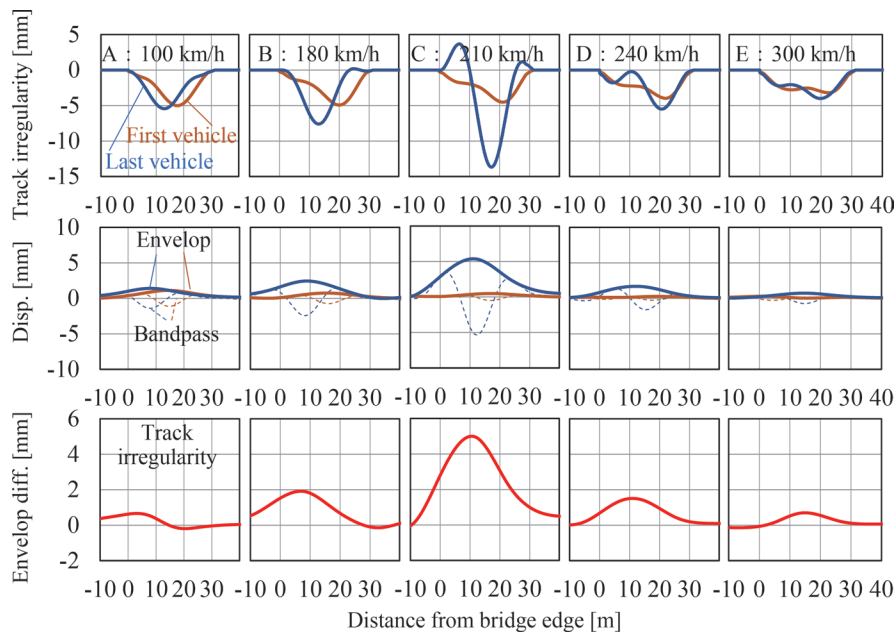
Fig. 6 Application results of the proposed method to track irregularity (span length 30 m, natural frequency 2.3 Hz, 8-car train)
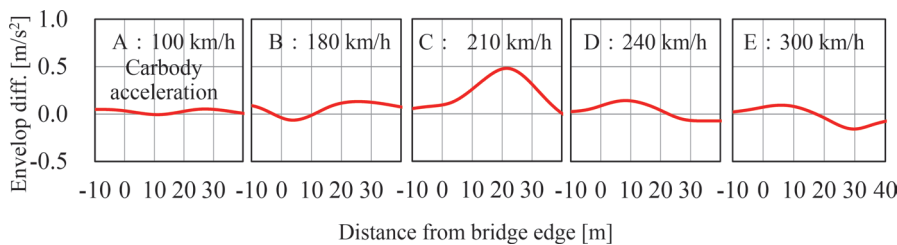
Fig. 7 Application results of the proposed method to carbody acceleration (span length 30 m, natural frequency 2.3 Hz, 8-car train)

bridges were extracted. Here, for validation, it was applied to both types of data, however in reality, this method can be applied if there is drive-by measurement data of either car body acceleration or track displacement.

Car body acceleration was measured on the car body floor just above the front bogie of both leading vehicles, and track displacement was measured at the center position of the rear bogies of both leading vehicles by a bogie-mounted inertial versine track inspection device [4]. All of these have already been installed in commercial vehicles for the purpose of managing ride comfort, car body vibration, or track condition, and no new capital investment was made when applying the proposed method. In addition, since the proposed method was implemented on LABOCS, the agreement between the peak span of the envelope difference and the bridge span length can be confirmed together with the equipment data already constructed on LABOCS.

The number of trains was 6 and the maximum speed was 260 km/h. The proposed method was applied to the bridge section of about 20 km, excluding the tunnel and the low-speed section near the stop station where the traveling speed is less than 200 km/h.

4.2 Resonance bridge detection results

Figure 8 shows a result of applying the proposed method to the car body accelerations and track displacement measured at the first and last vehicles. In the figure, for each of the car body acceleration and track displacement measured at the first and last vehicles, the waveforms were subjected to a bandpass filter and envelope processing, and the first and last difference processing were performed for these waveforms. The difference waveform is shown. There are five bridges from A to E in the section in the figure, however in the envelope processing waveforms of both car body acceleration and track displacement, the waveform of the last vehicle tends to be predominant at the position of Bridge E (shown in red enclosed in the figure). Therefore, it is inferred that dynamic response amplification occurs due to the resonance of Bridge E. On the basis of this tendency, in the envelope difference, a peak with a span almost the same as the bridge span length is formed at the position of Bridge E. The train speed at the section was about 230 km/h. Therefore, it can be determined that Bridge E is in a resonance state at a train speed of about 230 km/h. As a result of applying the proposed method,
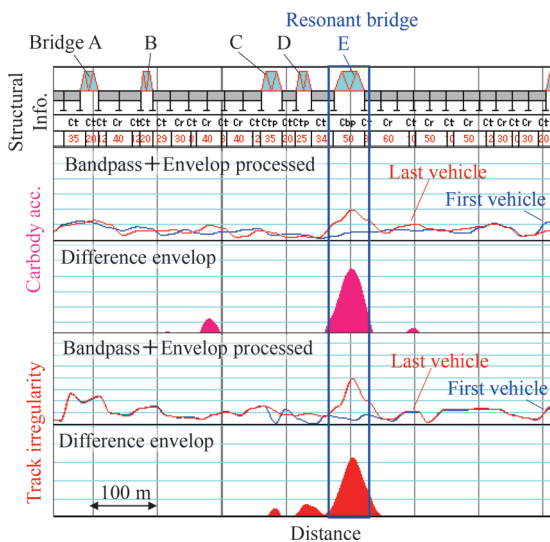
more than 30 bridges were extracted as resonant bridges as in bridge E. Although small dominant components can be confirmed in the difference waveform at locations other than the bridge E, these are judged to be effects other than the resonance of the bridge because the dominant amplitude is small and the bridge span length and the dominant span do not match.

4.3 Verification by in-situ bridge measurement

To verify the resonance state of the extracted bridges, the bridge displacement under train passages from the ground was measured.

Figure 9 shows a measurement scene on the ground. In Bridge E, the U Doppler II [11]: a laser Doppler speedometer with a self-vibration correction function, was used to measure remotely the vertical displacement of the bridge when a train passed; a reflective maker was installed on the lower surface of the bridge mid-span.

Figure 10 shows the displacement measurement results when a train passed. It is possible to confirm the waveform peculiar to resonance bridges in which the displacement amplitude increases as a train passes. In addition, since the train speed is close to 230 km/h when it is determined to be a resonant bridge by the drive-by measurement, it can be confirmed that the bridge extracted from the drive-by measurement data is actually in a resonant state. Of the bridges extracted by the proposed method, the measurements from the ground were carried out on 7 bridges including Bridge E, and it was confirmed that all of them actually resonated.

5. Conclusions

This study describes the development of an efficient method using data (track displacement or car body acceleration) measured on a train running at a high speed to detect resonant bridges, which is one of the focus points in the maintenance of high-speed railway bridges and equipment installed on them. More than 30 resonant
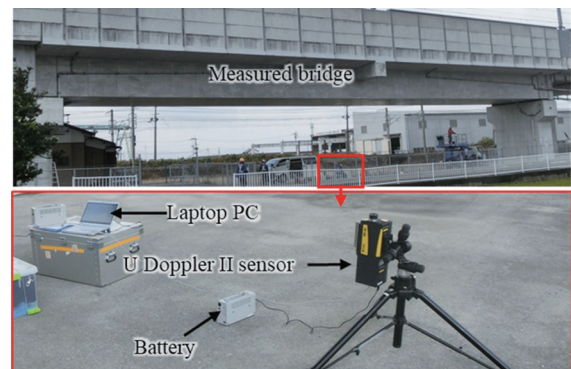

Fig. 9   In situ measurement of bridge E

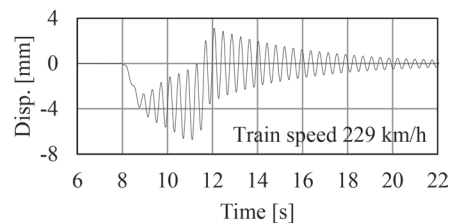**Fig. 8   Application result (train speed 230 km/h)**

Fig. 10   In situ measurement result of Bridge E

bridges were then extracted by applying this method to real drive-by measurement data, and confirmation was obtained that this resonance was consistent with the on-site measurement results.

The proposed method has already been used on several Japanese high-speed lines and has contributed to the management of resonant bridges and the efficiency of inspection of overhead catenary equipment. However, there were some cases where it was difficult to apply the method to actual data, because of factors such as position synchronization errors or passing cross trains. Currently, the authors are improving the system to solve these problems and to make it more accurate and automatically extractable. There is also a pressing need for the detection of resonance in short span lengths of about 10 m, which is outside the scope of the proposed method. Thus, expansion of the application range of the method by changing the filter passage band of the proposed method according to the resonance of short span bridges is an important challenge.

References

[1] Fujino, Y., Siringoringo, D. M., Ikeda, Y., Nagayama, T. and Mizutani, T., "Research and implementations of structural monitoring for bridges and buildings in Japan," *Engineering*, Vol. 5, No. 6, pp. 1093-1119., 2019.

[2] Yang, Y. B., Yang, J. P., Zhang, B. and Wu, Y., *Vehicle Scanning Method for Bridges*, John Wiley & Sons Ltd., Hoboken, NJ, U.S.A., 2019.

[3] Matsuoka, K., Tanaka, H., Kawasaki, K., Somaschini, C., and Collina, A., "Drive-by methodology to identify resonant bridges using track irregularity measured by high-speed trains," *Mechanical Systems and Signal Processing*, Vol. 158, No. 107667, 2021.

[4] Matsuoka, K., Collina, A., Somaschini, C. and Sogabe, M., "Influence of local deck vibrations on the evaluation of the maximum acceleration of a steel-concrete composite bridge for a high-speed railway," *Engineering Structures*, Vol. 200, No. 109736, 2019.

[5] Matsuoka, K., Tokunaga, M., Ogihara, Y., Tsukishima, D. and Goto, K., "Response Reduction Effect and Application Scope of Additional Supports Reinforcement for a High-Speed Railway PRC Bridge," *Journal of Japan Society of Civil Engineers, Ser. A1*, Vol. 76, No. 3, pp. 523-541, 2020 (in Japanese).

[6] Tsunemoto, M., Matsuoka, K., Goto, K. and Ikura K., "Measures for Reducing Damage to Overhead Contact Line System due to Bridge Oscillations Caused by Passing Trains," *RTRI Report*, Vol. 34, No. 9, pp. 35-40, 2020 (in Japanese).

[7] Matsuoka, K., Watanabe, T. and Uehan, F., "Resonant Bridge Detection Method by On-board Measurement," *Quarterly Report of RTRI*, Vol. 61, No. 2, pp. 133-138, 2020.

[8] Tanaka, H., Yamamoto, S., Oshima, T. and Miwa, M., "Methods for Detecting and Predicting Localized Rapid Deterioration of Track Irregularity Based on Data Measured with High Frequency," *Quarterly Report of RTRI*, Vol. 59, No. 3, pp. 169-175, 2018.

[9] Matsuoka, K., Kaito, K. and Sogabe, M., "Bayesian time–frequency analysis of the vehicle–bridge dynamic interaction effect on simple-supported resonant railway bridges," *Mechanical Systems and Signal Processing*, Vol. 135, No. 106373, 2020.

[10] Matsuoka, K., Tokunaga, M. and Kaito, K., "Bayesian estimation of instantaneous frequency reduction on cracked concrete railway bridges under high-speed train passage," Mechanical Systems and Signal Processing, Vol. 161, No. 107944, 2021.

[11] Matsuoka, K., Uehan, F., Kusaka, H. and Tomonaga, H., "Experimental Validation of Non-Marker Simple Image Displacement Measurements for Railway Bridges," *Applied Sciences*, Vol. 11, No. 15, 7032, 2021.

Authors

Kodai MATSUOKA, Dr. Eng.
Senior Researcher, Structural Mechanics, Railway Dynamics Division
Research Areas: Bridge Dynamics, Vehicle and Bridge Interaction, Damage Detection

Kyohei KAWASAKI
Senior Engineer, Kyushu Railway Company
Research Areas: Track Maintenance, Image Processing and Signal Processing

Hirofumi TANAKA, Dr. Eng.
Senior Researcher, Track Geometry and Maintenance, Track Technology Division
Research Areas: Track Geometry Management, On-board Monitoring and Signal Processing

Mizuki TSUNEMOTO
Senior Researcher, Contact Line Structures, Power Supply Technology Division
Research Areas: Dynamic Interaction between Pantograph and Catenary, Catenary Maintenance

Method for Measuring Lateral Force Utilizing Shear Strains inside Wheel Load Measuring Holes of Instrumented Wheelset

Takatoshi HONDO   Shoya KUNIYUKI   Takayuki TANAKA   Mitsugi SUZUKI

Vehicle Mechanics Laboratory, Railway Dynamics Division

This paper proposes a new configuration for an instrumented wheelset, which is used to measure wheel/ rail contact forces to assess running safety and evaluate curving performance of railway vehicles. Lateral force, which is a component of the wheel/rail contact forces, is measured as strains which are caused by the bending deformation of the wheel web in a conventional instrumented wheelset. According to this measurement principle, the measured lateral force is affected if a wheel load is applied, which reduces the accuracy of lateral force measurement. This paper describes in detail a novel instrumentation method for measuring the lateral force which can reduce the influence of the wheel load by using the shear strains inside the holes of the wheel web.

Key words: *running safety, measurement of wheel-rail interaction force, derailment quotient, 3-axis strain gauge, bending moment*

1. Introduction

Measurement of wheel load and lateral force between wheels and rails is important for assessing running safety and evaluating the curve passing performance of railway vehicles. Wheel load (P) is the vertical force that acts between a wheel and a rail, and lateral force (Q) is the force in the lateral direction. The value Q/P obtained by dividing the lateral force by the wheel load is known as the derailment quotient and is used as an indicator for evaluating running safety. One method for measuring wheel load and lateral force continuously when vehicles travel on an actual track, is to use an "instrumented wheelset" (Fig. 1), which has multiple strain gauges on the wheel's surface [1]. Although there are several ways to construct an instrumented wheelset, the common measurement principles in instrumented wheelsets used in Japan are as follows: the wheel load is measured using the vertical strain generated on the side surface of holes, and the lateral force is measured using the bending strain on the side surface of wheels [2, 3].

In the lateral force measurement method using bending strains (hereinafter referred to as the 'conventional method'), when a contact position between a wheel and a rail shifts in the lateral direction, measurement accuracy may decrease due to the influence of the bending moment induced by the wheel load (Fig. 2). Specifically, the measured lateral force of wheels on the outer track side of a curve, which come into contact near the flange while passing through a curve, may exceed the real force due to the influence of the wheel load. This sometimes results in an evaluation of certain situations which is stricter than the reality. This paper proposes a method for measuring lateral force that utilizes shear strains inside the wheel load measurement holes as a measure of the lateral force (hereinafter referred to as the 'proposed method'). It is shown that the proposed method is less affected by wheel load than the conventional method through an FEM analysis and a static load test.

2. Overview of the proposed method

2.1 Concept and merit of the proposed method

As shown in Fig. 3, the proposed method utilizes shear strains generated in the wheel as lateral force is exerted. In this method,
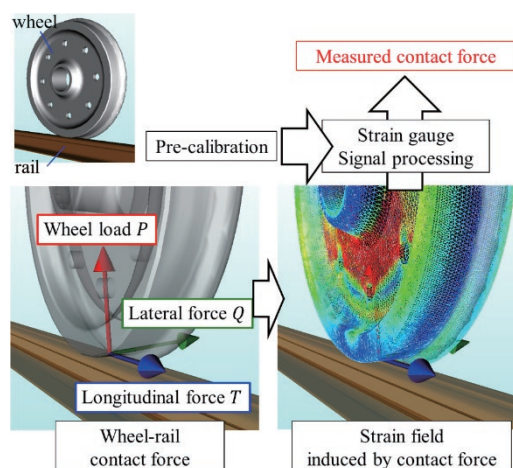
Fig. 1 Principle of measuring wheel-rail contact forces using instrumented wheelset

3-axis strain gauges, which are generally used for rosette analyses, are attached where strain gauges for measuring the wheel load are attached, and shear strains are simultaneously measured with normal strains. Specifically, normal strains are measured with a central strain gauge and used as a measure of the wheel load. On the other hand, the concept of the proposed method is to measure the shear strains with remaining two orthogonal strain gauges and use them as a measure of the lateral force.

Even if the proposed method is adopted as a measurement method for the lateral force, the influence of the wheel load cannot be completely eliminated. However, as shown in the verification in this paper, the influence of the wheel load is reduced compared to the conventional method. Simultaneously measuring the lateral distance from the tread center to the contact position is another possible method capable of eliminating wheel-load influence completely [4-8]. However, this method requires additional (6 channels in total) measuring equipment [4, 5], or more bridge circuits [6-8] than usual to determine the lateral contact position. In particular, signal transmission devices which have additional channels are required at the same time when adding bridge circuits to the instrumented wheelset. Although the measurement method proposed in this paper cannot
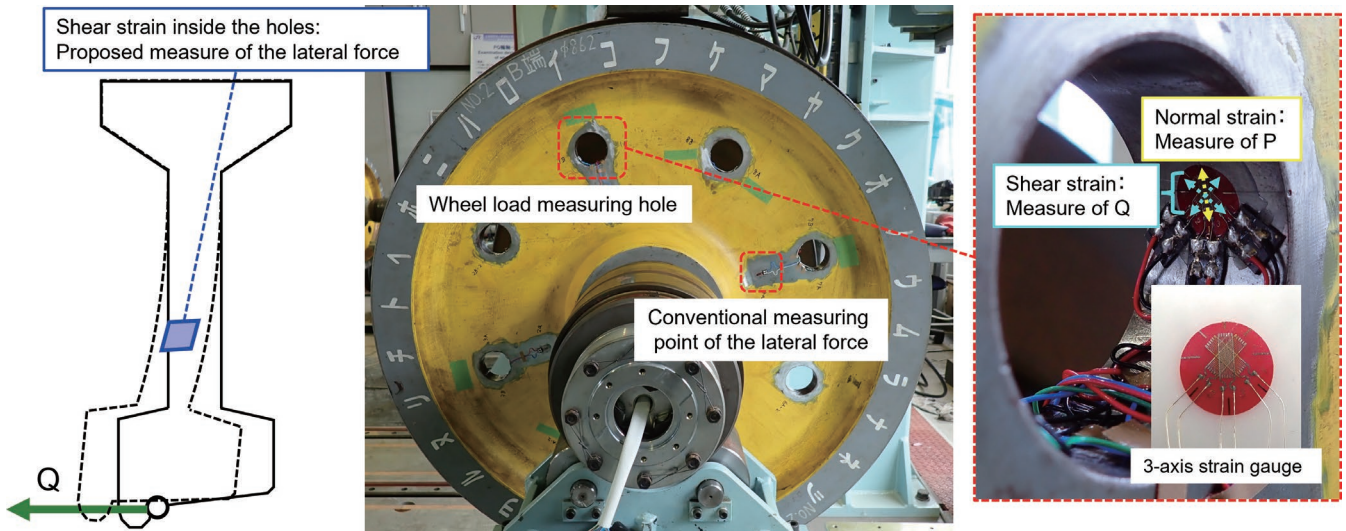
Fig. 3　Concept of measurement method for lateral force utilizing shear strain inside wheel load measuring holes
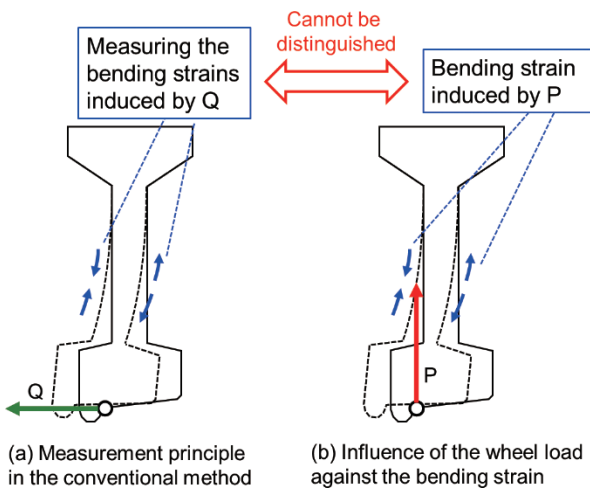

(a) Measurement principle
in the conventional method

(b) Influence of the wheel load
against the bending strain

Fig. 2　Mechanism of reducing measurement accuracy of lateral force due to wheel load

Fig. 4　Bridge configuration of proposed method

completely eliminate the influence of the wheel load, it has the advantage of being compatible (4 channels in total) with the conventional method in terms of the number of channels and positions where strain gauges are attached.

2.2　Configuration of the bridge circuit

　　Figure 4 shows an example of the bridge circuit configuration of the proposed method for a wheel set used for the "new continuous method" [2] in which eight holes for measuring wheel load are provided for each wheel. For convenience, as shown in the figure, wheel load measuring holes are numbered from 1 to 8. 3-axis strain gauges are attached to the opposite positions of holes 1, 3, 5, and 7 (4 locations), two at each hole on its inner opposite positions. A single-axis strain gauges are attached to remaining four holes same as the conventional method to form a bridge circuit. As shown in the lower part of Fig. 4, the channels of the 3-axis strain gauges, tilted at 45 degrees, are grouped into two bridge circuits qs1 and qs2.

　　It is also conceivable to attach 3-axis strain gauges to all eight holes, but as described later, sufficient sensitivity against the lateral

force is ensured over the entire circumference of the wheel even if the 3-axis strain gauges are attached in only four locations. Therefore, from the viewpoint of sensitivity, both the new continuous method and the intermittent method can be supported by the configuration shown in Fig. 4.

3.　Methods for evaluating characteristics of the proposed method

3.1　Numerical investigations using FEM

　　Prior to tests using an actual instrumented wheelset, an FEM analysis was performed using a single-wheel finite element model in which a geometric constraint was set on the inner surface of the hole

(a) FEM model

Circumferential direction: 32 points

Lateral direction: 3 points

(b) Setting of the loading points
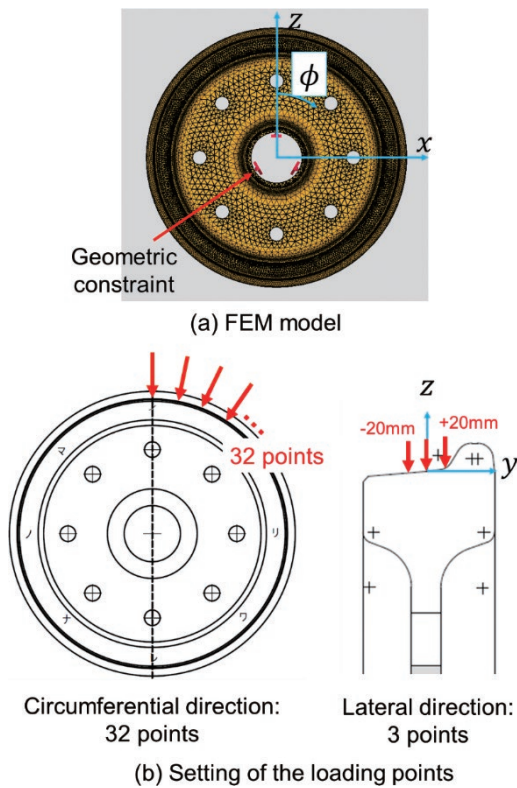
Fig. 5　Overview of FEM model

into which the axle was press-fitted. Figure 5 shows an overview of the FEM model. The 3D geometric model of the wheel was built with a 3D CAD software "FreeCAD", divided into quadratic tetrahedral elements with an auto-mesher "NETGEN", and then an FEM solver "CalculiX" was used to build and solve simultaneous equations. We analyzed a strain field under various loading conditions. As shown in Fig. 5, loading points were set at 32 points in the circumferential direction and three points in the lateral direction ($y = 0$ mm, $y = \pm 20$ mm), for a total of 96 points.
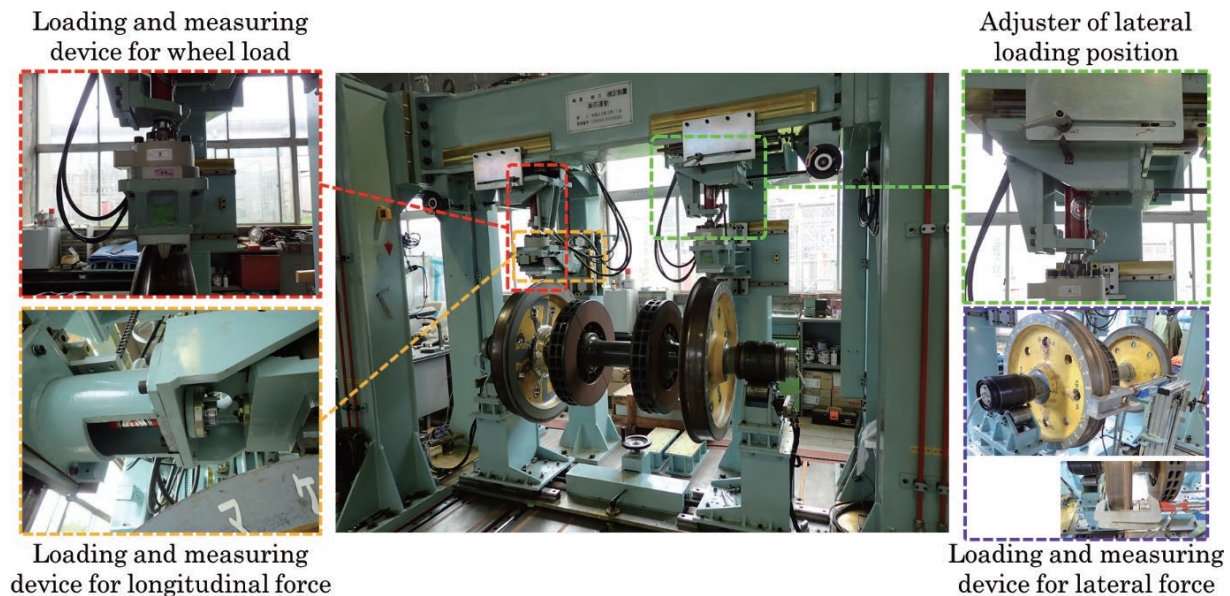
The results of analysis with CalculiX were obtained as a Lagrange strain tensor at a node position. In order to obtain measurement results per strain gauge, strain tensors were first interpolated by quadratic function, and strain tensors were calculated at the positions where the strain gauges were attached. Furthermore, strain tensors described in a global coordinate were transformed in the strain gauge direction. For example, for a strain gauge tilted 45 degrees in a 3-axis strain gauge, the calculated strain tensor is rotationally converted by 45 degrees to obtain a strain component along the direction in which the strain gauge is attached. The output of the bridge circuit was obtained by calculating the electric resistance of the strain gauges using the converted strain component and applying the formula of the Wheatstone bridge circuit.

3.2 Experimental investigations by static load test

In order to confirm the validity of the FEM analysis, static load tests were conducted using the calibration test device for an instrumented wheelset (Fig. 6) owned by the Railway Technical Research Institute. This device can load a force equivalent to a wheel load and lateral force on the instrumented wheelset and calibrate the wheelset by simultaneously measuring the load with the load cell and the output of the bridge circuits of the instrumented wheelset. The lateral loading position of a wheel load can be changed by the adjustment mechanism shown in Fig. 6. Using this mechanism, the outputs of the bridge circuits can be evaluated when the loading position of a wheel load is shifted in the lateral direction.

4. Results of investigations

4.1 Feasibility as a measure of lateral force

In order to verify whether the shear strains inside wheel load measuring holes can be used as a measure of lateral force, the relationship between a load equivalent to the lateral force and the shear strain was investigated with an FEM. The difference in loading position of the lateral force in the lateral direction does not have a significant effect, therefore the lateral loading position was set to

**Fig. 6　Overview of calibration test device for instrumented wheelset**
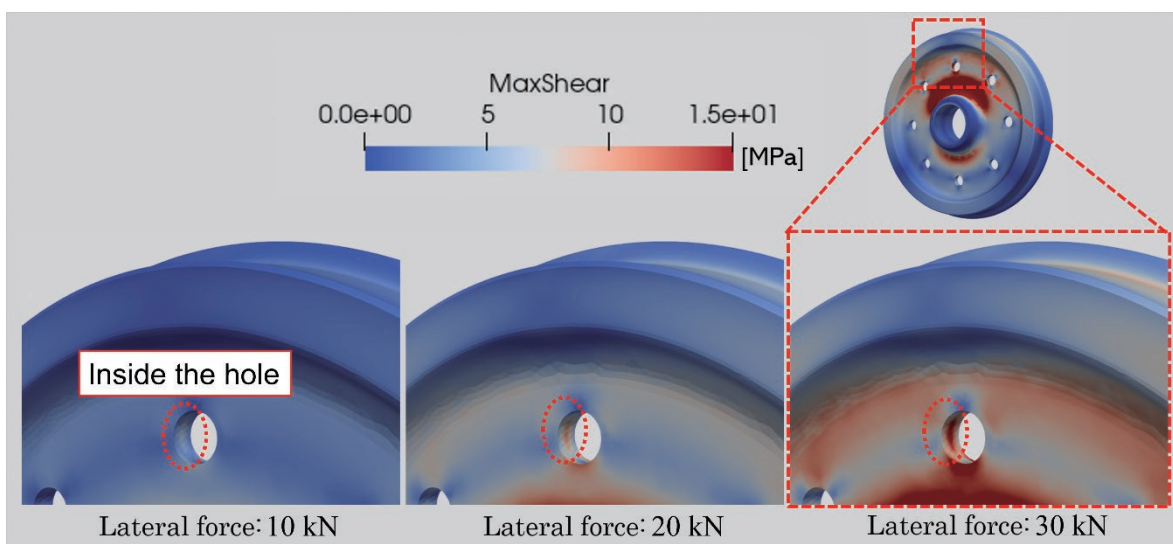
Fig. 7 Relation between lateral force and maximum shear stress distribution: color contour of FEM results

one condition of $y = 0$ mm.

Figure 7 shows an example of the FEM analysis results, and shows the distribution of maximum shear stress near a wheel load measuring hole expressed in color contours. The figure shows the analysis results in which a lateral force is loaded in three stages of 10 kN, 20 kN, and 30 kN above the hole No. 1 shown in Fig. 4. From this figure, it is confirmed that the shear stress inside the wheel load measuring hole tends to increase as the lateral force increases. On the other hand, Fig. 8 shows the relationship between the lateral force and the output of the bridge circuit qs1 when the lateral force was loaded and unloaded in a static load test. The figure shows a proportional relationship between the lateral force and the bridge output. Therefore, it was confirmed that the shear strain can be used as a measure of the lateral force.

Figure 9 shows the results of the investigation into bridge sensitivity (value obtained by dividing bridge output by loading lateral force) with respect to lateral force for all 32 loading points set on the wheel circumference. In the figure, the bridge outputs of a conventional method using wheel bending are also shown as bridge circuits qb1 and qb2. The characteristics of the sensitivity of the proposed method are expressed as a trigonometric function whose phase is approximately 90 degrees different from the loading position on the wheel circumference, as in the conventional method. This confirms the hypothesis that sufficient sensitivity is ensured over the entire circumference of the wheel even if just four holes are used for instrumentation using 3-axis strain gauges. Compared with the conventional method, the peak value of the sensitivity of the proposed method is reduced to about 1/3, however in the case of a general wheelset for meter-gauge lines, the peak sensitivity of the bridge circuit for wheel load measurement was about 2.5 $\mu\varepsilon$/kN [9, 10]. (about 1/4 of the proposed method). Therefore, the sensitivity of the proposed method does not become a bottleneck of sensitivity for the entire instrumented wheelset system.

In the results of the conventional method, there is a discrepancy between the FEM and the experiment, which may be due to the influence of the error of the evaluating position of the bending strain in the FEM. Specifically, since there is no definite standard on the position of strain gauges for measuring lateral force in the radial direction of the wheel, the strain amount was evaluated at a tempo-
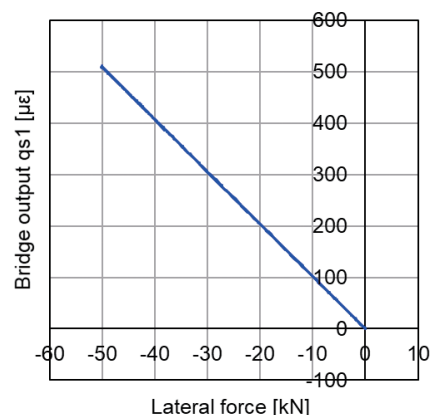
Fig. 8 Relation between lateral force and bridge output in static load test

rally position in the FEM analysis. It is probable that this divergence was caused by this.

4.2 Cross-sensitivity associated with wheel load

In this section, the cross-sensitivity of the bridge circuit for lateral force measurement is investigated when a wheel load is applied. Figure 10 shows the relationship between the circumferential loading position and the cross-sensitivity obtained by the FEM analysis and the static load test for each loading position in the lateral direction. As shown in the figure, when the loading position of the wheel load is changed in the lateral direction (y direction), a relatively large output is also generated in the bridge circuit for lateral force measurement.

When comparing the influence of the wheel load in the conventional method and the proposed method, since basic strain susceptibility at each strain measurement point is different, even if the cross-sensitivity itself is compared between the two, it is not a fair comparison. When the wheel load P and the lateral force Q act at the same time, the output of the bridge circuit ε can be approximately expressed by (1).
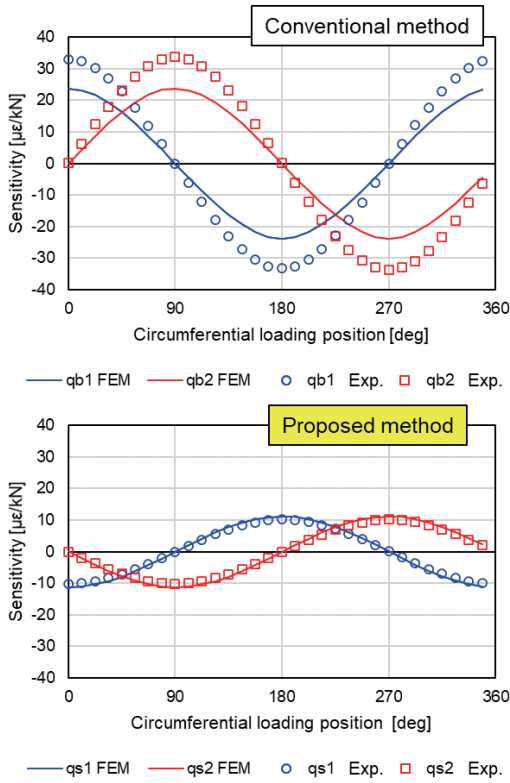
Fig. 9 Relation between the 32 points of loading position on the wheel circumference and the bridge sensitivity with respect to the lateral force

$$\varepsilon = \alpha Q + \beta P, \tag{1}$$

where α is the sensitivity against the lateral force and β is the cross-sensitivity against the wheel load. Assuming that the magnitude of the cross-sensitivity in the second term cannot be obtained, the measurement result of the lateral force $\hat{Q}$ can be expressed as (2).

$$\hat{Q} = \frac{\varepsilon}{\alpha} = Q + \frac{\beta}{\alpha}P \tag{2}$$

That is, the measurement result $\hat{Q}$ is obtained as a result of adding the cross-sensitivity term to true lateral force Q, and the degree of its

influence is determined by β/α if the wheel load P is the same value. Dividing both sides of (2) by P gives (3).

$$\frac{\hat{Q}}{P} = \frac{Q}{P} + \frac{\beta}{\alpha} \tag{3}$$

Assuming that the wheel load P is measured correctly, $\hat{Q}/P$ on the left side of (2) is the derailment quotient calculated from the measurement results, and Q/P on the right side is the true derailment quotient. Therefore, β/α represents the measurement error of the derailment quotient. In this paper, β/α is defined as "cross-sensitivity ratio." As is clear from the verification results so far, α and β are functions of the loading position φ in the wheel circumferential direction and y in the lateral direction, and functions $\alpha_1(\varphi)$, $\beta_1(\varphi, y)$, $\alpha_2(\varphi)$ and $\beta_2(\varphi, y)$ can be defined for each bridge circuits. Considering that each function, for example $\alpha_1(\varphi)$ and $\alpha_2(\varphi)$, can be expressed by a cyclic function whose phase differs by 90 degrees with respect to φ, the cross-sensitivity ratio $r(\varphi, y)$ is defined as in Eq. (4) as a function of φ and y.

$$r(\varphi, y) = \frac{\sqrt{\beta_1(\varphi, y)^2 + \beta_2(\varphi, y)^2}}{\sqrt{\alpha_1(\varphi)^2 + \alpha_2(\varphi)^2}} \tag{4}$$

Figure 11 shows the results of calculating the cross-sensitivity ratio as a function of φ under the condition of $y = \pm20$ mm, where the influence of wheel load is large. It can be seen that the cross-sensitivity ratio of the proposed method is smaller than that of the conventional method regardless of the difference in the contact position. In particular, the measurement accuracy of the forces by the intermittent method is expected to improve since the effect of reducing the cross-sensitivity ratio is particularly large in the vicinity of the hole to which the 3-axis strain gauge is attached (0deg, 90deg, 180deg, 270deg).

Comparing the experimental results of the conventional and the proposed method under a flange side loading condition ($y = 20$ mm), the reduction effect of the cross-sensitivity ratio was 0.015 at the maximum. This is the result of shifting the loading position by 20 mm from the center of the tread to the flange side, therefore it is assumed that the reduction effect of the cross-sensitivity ratio increases since the contact point is moved to the flange side on a sharp curve.
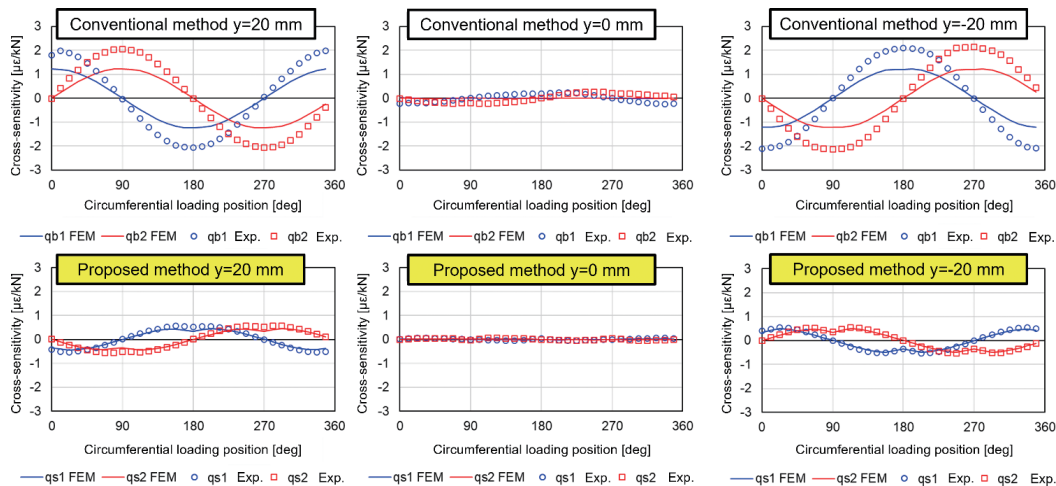
Fig. 10 Cross-sensitivity of the bridge circuits when the wheel load is applied
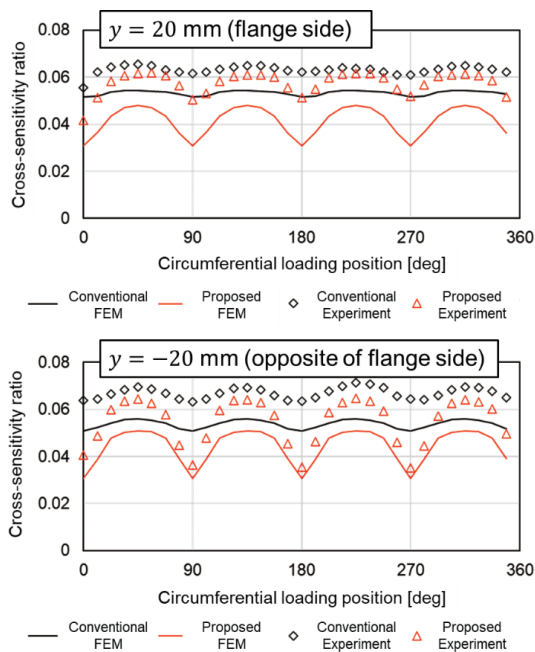
Fig. 11 Evaluation of the cross-sensitivity ratio

5. Conclusions

In this paper, we proposed a method for measuring lateral force that utilizes the shear strains inside the wheel load measuring holes. This method is characterized by wheel load and lateral force being measured at the same time using 3-axis strain gauges measuring the vertical strain and the shear strain simultaneously, and these 3-axis strain gauges are attached to the conventional strain gauge positions for measuring the wheel load of the instrumented wheelset. The analysis using a finite element method and static load tests show that the influence of the bridge output when the wheel load acts is relatively small compared to the conventional method, which is based on the bending strain of a wheel web. In addition, this method has the advantage of being compatible with the conventional method in terms of the number of channels and the position where the strain gauges are attached. In other words, by applying the proposed method, it is expected that running safety assessment can be carried out more accurately than before without causing a significant increase in cost.

References

[1] Bracciali, A., et al., "Review of instrumented wheelset technology and applications," *in Proceedings of the Second International Conference on Railway Technology: Research, Development and Maintenance*, No. 167, 2014.

[2] Ishida, H., et al., "Method of measuring wheel and rail contact forces and derailment quotients continuously (development of measuring device)," *Transactions of the Japan Society of Mechanical Engineers, Series C*, Vol. 63, No. 614, pp. 3417-3423, 1997 (in Japanese).

[3] Sato, K., et al., "Development of wheel load and lateral force measurement processing system combining intermittent and continuous measurement methods," *RTRI Report*, Vol. 22, No. 2, 2005 (in Japanese).

[4] Burstow, M., et al., "Understanding wheel/rail interaction with thermographic imaging," in Proceedings of the *22nd IAVSD International Symposium on Dynamics of Vehicles on Roads and Tracks*, No. 105, 2011.

[5] Yamamoto, D., "Locating of the contact position between the wheel and the rail by means of thermal imaging," *Quarterly Report of RTRI*, Vol. 60, No. 32, pp. 65-71, 2019.

[6] Kanehara, H. and Fujioka, T., "Measuring rail/wheel contact points of running railway vehicles," *Wear*, Vol. 253, pp. 275-283, 2002.

[7] Bižić, M.B., et al., "Development of method for experimental determination of wheel-rail contact forces and contact point position by using instrumented wheelset," *Measurement Science and Technology*, Vol. 28, DOI: 10.1088/1361-6501/aa666f, 2017.

[8] Ozawa, R., et al., "Method of identifying contact point of wheel on the rail by measuring strain generated on wheel web," *in The Proceedings of the Transportation and Logistics Conference*, 2018, Volume 2018.27, 2018.27, Session ID 3211, Pages 3211, 2018 (in Japanese).

[9] Hondo, T., and Noguchi, Y., "Measurement Method for longitudinal displacement of wheel/rail contact point using strain gauges put on wheels," *Mechanical Engineering Journal*, Vol. 7, No. 3, p. 19-00659, 2020.

[10] Hondo, T., "Extraction method for a wheel rotation average of longitudinal creep force from strain data acquired by instrumented wheelset without the use of rotation angle sensor," *Transactions of the JSME (in Japanese)*, Vol. 87, No. 894, 2021 (in Japanese).

Authors

Takatoshi HONDO, Ph.D.
Assistant Senior Researcher, Vehicle Mechanics Laboratory, Railway Dynamics Division
Research Areas: Vehicle Running Safety, Measurement Technology, Signal Processing

Takayuki TANAKA, Ph.D.
Assistant Senior Researcher, Vehicle Mechanics Laboratory, Railway Dynamics Division
Research Areas: Vehicle Dynamics, Vehicle Running Safety

Shoya KUNIYUKI
Researcher, Vehicle Mechanics Laboratory, Railway Dynamics Division
Research Areas: Vehicle Dynamics, Vehicle Running Safety

Mitsugi SUZUKI
Senior Researcher, Vehicle Mechanics Laboratory, Railway Dynamics Division
Research Areas: Vehicle Dynamics, Vehicle Running Safety, Measurement Technology

Summaries of Papers in RTRI REPORT (in Japanese)

Recent Activities for Research and Development of Railway Vehicle Technology
Takamitsu YAMAMOTO
(Vol.36, No.2, 1-4, 2022.2)

As for the recent situation surrounding railways, the efficiency of operations and labor saving are rapidly progressing due to the influence of the decrease in passengers due to the covid-19. Then, the DX (digital transformation) technology which has been applied to an automatic train operation and so on, is attracting attention. Another topic is a turning point toward the realization of global decarbonization, such as the demand for reduction of greenhouse gas emissions by "2050 Carbon Neutral" declared by the Suga Cabinet and "COP26". This paper introduces the outlines of three technologies related to these topics, "Evaluation method for gliding control performance by hybrid simulator", "Abnormal noise detection method during train running using neural network", and "High efficiency of diesel electric railcars".

Analysis of Hunting Stability Using Method for Calculating Periodic Solution
Yusuke YAMANAGA
(Vol.36, No.2, 5-10, 2022.2)

In order to evaluate the vehicle running stability, hunting motion test is commonly conducted using a real bogie on roller rigs. Hunting motion occurs at a certain speed without any disturbance. However, even below the critical hunting speed, hunting motion can occur when disturbance is applied. Our previous studies have shown that there exists a clear point where initial lateral displacement of wheelset causes hunting motion and the point originates from unstable limit cycle. Therefore, we applied a shooting method, which can calculate periodic solution for nonlinear system, to obtain an unstable limit cycle. This paper reports summary of the shooting method and its application for vehicle dynamics model, then examines the validity of the result obtained by the method.

Verification of the Influence of Elastically Supported Mass of Underfloor Equipment on the Reduction of Elastic Vibration of Carbody
Ken-ichiro AIDA, Tadao TAKIGAMI, Yuki AKIYAMA
(Vol.36, No.2, 11-16, 2022.2)

We have developed the high-damping elastic support of underfloor equipment as one method for reducing the elastic vibration of carbody. In this report, first, we conduct a running test on a commercial line to verify the effectiveness of the high-damping elastic support of mass. Secondly, we conduct an excitation test in the rolling stock testing plant to verify the effect of the elastically supported mass on the reduction of the elastic vibration of carbody. As a result of the excitation test, we confirm that the larger the elastically supported mass is, the larger the effect of improving the riding comfort is.

Evaluation of Influence Due to Reflection Point Shift on Axle Surface in Ultrasonic Flaw Detection
Kazunari MAKINO
(Vol.36, No.2, 17-22, 2022.2)

For ultrasonic flaw detection of axles, an inspection technique in which a shear wave is emitted into an axle at certain angles is widely applied. However, when a shear wave is obliquely incident on a boundary surface, sound beam displacement may shift a geometric reflection point parallel to the boundary surface. In this study, two types of boundary surfaces, that is, an axle body and a wheel seat, are targeted. The relationship between a shear wave incident angle and sound beam displacement is derived theoretically and then reproduced using finite element calculations. The propagation behavior of ultrasonic waves while inspecting surface flaws on an axle is discussed from the viewpoint of sound beam displacement.

Anomaly Detection for Equipment on Railway Vehicle Using Condition Monitoring Data
Toshihide YOKOUCHI, Tatsuro TAKASHIGE, Minoru KONDO
(Vol.36, No.2, 23-28, 2022.2)

In recent years, some railway vehicles are equipped with condition monitoring devices, which constantly record the operating condition of railway vehicle equipment. Thus, we improve the reliability of train operation by learning the data and detecting abnormalities using machine learning. Condition monitoring data is recorded in time-series. Therefore, we propose an anomaly detection method for railway vehicle equipment using Long Short Term Memory (LSTM), which is a deep learning method suitable for learning time-series data. In this paper, we apply the proposed method to data recorded at diesel cars in operation. As a result, it is confirmed that the anomaly scores increase in case of abnormal data using the proposed method and that anomalies are detected in railway vehicle equipment.

Degradation Prediction Method for Lithium-Ion Battery for Railway Vehicle Considering Temperature Variation
Yoshiaki TAGUCHI, Satoshi KADOWAKI, Gaku YOSHIKAWA
(Vol.36, No.2, 29-34, 2022.2)

Regarding the capacity degradation of lithium-ion battery, the Weibull-law-based long term prediction method has been studied. However, the use of this method has been limited to the case of a constant temperature. Therefore, we developed a method which allows us to vary temperature conditions, to lead to more practical prediction compared with the conventional method. We executed accelerated aging test with using two types of battery modules: one is used for traction, and another is used for control circuit for railway vehicle. The test results of both types demonstrated that the calculated values and measured values of battery capacity and inner resistance are in good agreement.

A Survey of the Adoption of SiC Semiconductor for Power Devices in Railway Vehicles in Japan and Overseas
Satoru HATSUKADE
(Vol.36, No.2, 35-40, 2022.2)

SiC power semiconductors are increasingly being applied to various power converters because of their performance of high-speed operation under even high temperature. The first adoption of SiC devices for railway vehicles was 2012 in Japan. Until the year of 2021, many railway vehicles in Japan have installed power converters with SiC devices. The adoption of these power converters with SiC devices are not limited to motor drives, but also extends to auxiliary power supplies and PWM rectifiers. However, there are few SiC device usages in overseas railway vehicles. This paper reports a survey result on the application of SiC power semiconductors to railway vehicles in Japan and overseas.

Development Trend of Fuel Cell Trains

Takashi YONEYAMA, Takayuki KASHIWAGI, Takamasa YAMADA

Fuel cell trains are being developed in Japan and abroad. In Japan, Railway Technical Research Institute and East Japan Railway Company have been developing fuel cell trains in each way. Overseas, European railway manufacturer Alstom unveiled a fuel cell train in 2015 and has conducted trial operation since 2018, and Germany's Siemens has also been developing a fuel cell Train. In China, a group company of CRRC, a manufacturer of rolling stock, developed a low-floor fuel cell tramway, which started operation at the end of 2019 in Foshan, China. This paper reports on these development trend of fuel cell trains.

Track Technology for Reducing Maintenance Cost and Labor Work

Masashi MIWA

From the viewpoint of safe train operation, railway track condition must also be kept in a satisfactory level by appropriate track inspection and maintenance activities. On the other hand, from the viewpoint of management soundness, it is highly desired to develop track technologies for cost reduction of both track inspection and maintenance. For developing the technologies, it is important to focus on the research area in terms of automation and labor saving by applying ICT and AI techniques progressing in recent years significantly. This paper describes the recent RTRI's R&D for these track technologies.

Image Analysis Engine for Supporting Onboard Track Patrol

Shuhei KONNO, Kyohei KAWASAKI, Kengo MISHIMA, Masashi MIWA, Atsushi SHIMIZU, Noboru NAKAJIMA

One of the maintenance works of railroad tracks is patrolling by the eyes of workers from a driver's compartment of a train in operation. To support such works, an image analysis engine has been developed. The engine consists of three image analysis techniques: self-localization, 3D measurement by multi-view stereo, differential detection, and can automatically detect the presence of obstacles intruding a structure gauge and environmental changes on a railroad track. In this paper, an overview of the system with the image analysis engine and processes of each image analysis techniques are described.

New Restrictions of Maintenance Works for Continuous Welded Rails at Low Temperatures

Shingo TAMAGAWA, Yuki NISHINOMIYA, Tomoya KOKETSU

This study aims to establish new restrictions of maintenance works for continuous welded rails at low temperatures in winter. The authors measured inward rail displacements and changes in axial rail forces caused by maintenance works and performed FEM analyses which simulate maintenance works under various track conditions. On the basis of the measurements and the FEM results, the authors propose the restriction diagrams of track maintenance works which provide allowable decreases in rail temperature from neutral temperatures. Furthermore, the authors propose an assessment flow for users to judge the propriety of maintenance works at low temperatures by using the diagrams. Consequently, new restrictions allow track maintenance works at low temperature conditions exceeding current restrictions.

Rail Broken Detection System from Vehicle as an Alternative to Track Circuits

Mitsuru HOSODA, Hiroyuki AIZAWA, Ryu-ichi YAMAMOTO

In order to develop a method for detecting rail breakage from vehicle, we focused on non-contact air coupled ultrasonic wave, accelerometer, and sound level meter, to conduct a basic study on their applicability. Furthermore, we optimized the detection conditions such as frequency of ultrasonic sensor and probe size so on to utilize the non-contact air coupled ultrasonic technology to rail broken detection. Also, we analyzed axil box acceleration when vehicle run through rail opening and the noise from the sound level meters installed on both sides of vehicle body. This paper describes the results of these basic studies and rail broken detection method developed based on them.

Design Method for Ballasted Track Applicable to Widening of Sleeper Spacing

Tadashi DESHIMARU, Daiki YAMAOKA, Kazuki ITO, Saki SHIMIZU

A design method for ballasted track, which is applicable to the case of widening sleeper spacing, considering the condition of ballast and track bed and the quality of maintenance, was proposed. The method was considered to be a complement to the conventional design method, defined in the Railway Structure Design Standard – Track Structure. On the basis of the proposed method, we conducted the simulation of train running on the condition of various curve radii, and clarified the limit sleeper spacing which secures running safety. Moreover, we conducted a trial calculation regarding the propriety of widening of sleeper spacing using the method.

Fatigue Life Evaluation of PC Sleepers Based on Wheel Load Measurement Results

Keiichi GOTO, Tsutomu WATANABE, Shintaro MINOURA, Manabu IKEDA

In this study, we evaluate the remaining life of PC sleepers from the viewpoint of the fatigue life of PC-steels of the PC sleepers. Specifically, we develop a method of acquiring the stress waveform of the PC-steels during train running. Furthermore, using this waveform, we calculate the fatigue strength of the PC-steels in consideration of the occurrence probability of wheel load in actual measurement, and quantitatively evaluate the fatigue life of the PC-steels. The result of this study shows that the PC-steels for post-tension type has a longer fatigue life than those for pre-tension type, and the PC-steels for both types have a fatigue life of over 300 years.

Design Method for Roadbed Improvement for Existing Ballastless Track

Kazuki ITO, Yoshitsugu MOMOYA, Takahiro KAGEYAMA

In order to reduce the cost of track maintenance, ballastless track for existing line where ballast voids are filled with cement grout has been developed and put into practical use. However, there is a problem that some constructed ballastless tracks laid on soft roadbed require repair within a few years after operation. Therefore, we developed an improvement method for the ballastless tracks which are laid on soft roadbed and conducted construction to verify the developed method at existing line. In the construction, roadbed improvement thickness was determined according to the proposed design flow. This paper describes the improvement method developed for ballastless tracks for existing line and its results of verification test.

Evaluation of Settlement Characteristics for Grouted Ballasted Track Applied to Ballasted Track with Mud Pumping

Shota FUCHIGAMI, Takahisa NAKAMURA, Takatada TAKAHASHI, Yoshitsugu MOMOYA
(Vol.36, No.3, 41-46, 2022.3)

When mud pumping begins to generate in ballasted track, frequency of repair work increases. Therefore, several types of ballastless tracks have been developed to reduce the repair work of ballasted track. For example, grouted ballasted track which uses super-fine particle cement (SFC) milk as grout material, can be used with existing aged ballast. However, SFC milk could not be applied to ballasted track which produced mud pumping. In this study, we have proposed several construction methods for grouted ballasted track with SFC milk that can be applied to ballasted track which produced mud pumping, and have evaluated the effectiveness of the track in reducing settlement. As a result of the cyclic loading test on full-scale track model and test construction on commercial lines, it was confirmed that grouted ballasted track with SFC milk had a sufficient settlement reduction effect.

Thermal Deformation Analysis of Gas Pressure Welding of Rail

Hajime ITOH, Ryu-ichi YAMAMOTO, Hiroyuki AIZAWA, Hiroki IZUTSU, Mikihiro IWASAKI
(Vol.36, No.3, 47-52, 2022.3)

We developed thermal deformation analysis model by using numerical calculation in order to quantitatively understand deformation behavior of gas pressure welding of rail. We found that the deformation degree at the center of the rail base and the jaw part of the rail head are smaller than that of other parts. Furthermore, we also identified that the hot cracks occur at their parts in the simulative tests of the crack. This paper describes the developed thermal deformation analysis model of gas pressure welding of rail and its validation test results.

Recent Research and Development on Disaster Prevention Technology

Naoyuki OTA
(Vol.36, No.4, 1-4, 2022.4)

This paper provides an overview of the impact of climate change on Japan's weather and introduces some of the research being conducted by R.T.R.I. in this regard. In line with our research plan "RESEARCH2025", we are working on developing following researches : a high precision operation control system applying observation data, and an evaluation method for the stability of slopes after heavy rain. We will develop technologies to improve the resilience of railways against disasters using a variety of digital information.

Development of Estimation Method for Run-off from the Bottom of Snow at Any Point using AMeDAS Data

Shigehiro IIKURA, Ryota SATO, Daisuke TAKAHASHI
(Vol.36, No.4, 5-10, 2022.4)

A method for estimating a run-off from the bottom of snow at any point in the snow melt season is proposed using AMeDAS data. In this method, meteorological elements at any point are estimated using the IDW (Inverse Distance Weighting) method, and the estimated values are input to an estimated model of a run-off from the bottom of snow to estimate the amount of snowmelt. As a result of the analysis, we found that the amount of run-off from the bottom of snow can be roughly estimated at any point near a meteorological station (usually within 20 km).

Proposal of Snowmelt Disaster Warning Criteria Using Effective Rainfall Index that Reflects Snowmelt

Tsuyoshi TAKAYANAGI, Ryota SATO, Osamu NUNOKAWA
(Vol.36, No.4, 11-16, 2022.4)

In snow-covered areas, slope failures induced by snowmelt water may occur. In this study, we attempted to develop warning criteria for snowmelt disasters using the effective rainfall index, which reflects the analyzed snowmelt amount (hereinafter referred to as the effective snowmelt index), as an evaluation index. In this study, we verified the appropriate half-life of the effective snowmelt index by comparing it with the results of groundwater level observation in snow-covered areas. As a result, it was confirmed that a strong correlation between them was confirmed under the conditions that the half-life of the index was set to approximately 24 to 96 hours. In addition, through case studies, we found that the warning criteria using the effective snowmelt index and snow depth as evaluation indexes could effectively warn of snowmelt disasters.

Effect of Change in Water Content of Soft Mudstone on Bond Strength of Rock Bolts

Yuichiro NISHIKANE, Takuya URAKOSHI, Keisuke SHIMAMOTO, Michiaki IMAIZUMI
(Vol.36, No.4, 17-22, 2022.4)

In this study, the authors of this paper devised a testing method for evaluating the bond strength between rock and an anchoring material for holding a rock bolt at a laboratory using boring cores. Furthermore, the authors examined the effect of the change in water content of Neogene mudstone on the bond strength by conducting this test after changing the water content of rock samples. As the results of the examination, we make it clear that the bond strength of the rock sample decreases when the water content of the rock sample is decreased and subsequently increased.

A Method to Extract Streams with Debris Flow Hazard using Sediment Volume

Atsushi HASEGAWA, Yuichiro NISHIKANE
(Vol.36, No.4, 23-29, 2022.4)

Recently, there has been damage often by debris flow that occurs at valleys on railway lines. However, since there are many valleys on railways, it is not easy to investigate the risk of debris flow. Therefore, it is important to develop a method to estimate the risk of debris flow. Hence, we present a method to estimate the risk of debris flow on the basis of the geomorphological and geological features of valleys where debris flow once occurred.

Development of Analysis Method of Tsunami Overflow and Scouring by Soil-water Coupled Analysis Using Mesh Free Method

Keita ABE, Kohei MUROTANI
(Vol.36, No.4, 31-37, 2022.4)

The tsunami induced by 2011 earthquake off the Pacific coast of Tohoku caused a lot of tremendous damage to railway embankments. Furthermore, in recent years, heavy rainfalls near water catching terrain have caused overflow, erosion, and scouring in the embankment, indicating that heavy rainfall disasters have tended to become more serious. In this study, we developed an analysis method of tsunami overflow and scouring by soil-water coupled analysis using mesh free methods. Such a method can be an effective tool to predict the damage due to overflow and scouring in the embankment, evaluate countermeasures against the damage, and further deepen model experimental studies. This paper explains overview of the developed analysis method and then presents the results from reproduction analyses of a series of model experiments.

Improvement in Rapidness of Earthquake Early Warning using Ocean Bottom Seismic Data

Shunta NODA, Naoyasu IWATA

This paper proposes two earthquake early warning (EEW) methods for ocean bottom seismic (OBS) data system of railways. The one is that the P-wave warning method, which has been used in the conventional Shinkansen system, can be applied also to the OBS data. Using multiple-station data, the other method enables us to issue an earthquake alert to areas far from the source region earlier than the conventional technique while an extremely large rupture is in progress. We conclude that the OBS data system can be improved in terms of the rapidness of EEW using the methods proposed in this study.

Method for Resetting Operation Regulation Standards Considering Seismic Risk of Railway Facilities

Kimitoshi SAKAI, Kazunori WADA, Akihiro TOYOOKA

The regulations of seismic intensity to suspend a train operation after earthquakes is determined empirically according to the past disaster. Therefore, it is difficult to reflect the effects of seismic countermeasures, such as seismic reinforcement and additional seismometers, in the regulation standards of train operations. To resume train operations as quickly as possible after an earthquake, this study proposes a method for updating the regulation standards of train operations based on risk analysis. In the proposed method, the seismic risk of each facility is evaluated and used to determine the regulations for suspending a train operation. Using this method, the effect of seismic countermeasures, such as improving the seismic performance of railway facilities and adding seismometers, can be directly reflected to the regulations of train operations.

Study on Method for Setting Seismic Force on Railway Viaduct Considering Influence of Shed

Hiroshi MIKI, Daisuke ISHIKAWA, Katsuyuki SHIMIZU

In elevated stations, it is general that shed and viaduct are integrated structures. However, it is considered that in many cases, the shed and the viaduct are designed separately because of different execution periods of design and construction. Therefore, it is necessary to take into account the influence of the interaction between the shed and the viaduct in the calculation of the seismic forces used in the design of the shed and the viaduct, respectively. Specifically, it is necessary to consider the resonance (response amplification) with the viaduct for the seismic force to the shed. On the other hand, the seismic force on the viaduct is considered to be added by the shed as it interacts with the shed, but the actual situation has not been clarified. Therefore, in this paper, the seismic force on the viaduct integrated with the shed is analyzed and a practical setting method is proposed.

May 2022 Vol. 63 No. 1 - No. 2

Dear QR, Quarterly Report Readers,

RTRI pleased to tell you that the tenth issue of "Ascent," the semiannual magazine of RTRI was released on 15 March 2022, featuring "Simulation Technology".
All the issues of "Ascent" are available on:
https://www.rtri.or.jp/eng/publish/ascent/

Quarterly Report of RTRI

Q
UARTERLY

R
EPORT of

RTRI

RAILWAY TECHNICAL RESEARCH INSTITUTE